Assessing the Effectiveness of Impact-Mitigating Countermeasures at Reducing Fatality Risk in the NYC Subway

---

A

Thesis

Presented to

the faculty of the School of Engineering and Applied Science

University of Virginia

---

in partial fulfillment

of the requirements for the degree

Master of Science

by

Logan Zentz

May 2025

APPROVAL SHEET

This

Thesis

is submitted in partial fulfillment of the requirements
for the degree of

Master of Science

Author: Logan Zentz

This Thesis has been read and approved by the examing committee:

Advisor: Matthew Panzer

Advisor:

Committee Member: Greg Shaw

Committee Member: Jason Forman

Committee Member: Jason Kerrigan

Committee Member: Bronislaw Gepner

Committee Member: Matthew Panzer

Committee Member:

Accepted for the School of Engineering and Applied Science:

Jennifer L. West, School of Engineering and Applied Science

May 2025

Abstract

The New York City subway system is the preferred mode of transportation for millions of commuters daily and is an affordable alternative to other transportation options. Despite this utility, the subway has had a public safety problem going back decades. In NYC alone, over 50 deaths and dozens of debilitating injuries are caused by train-pedestrian collisions on a yearly basis [1]. Many conventional solutions, such as platform doors, are not possible due to the subway's aging infrastructure, excessive installation costs, and accessibility issues [2]. To address the safety concerns within NYC subway, the Federal Transit Administration funded a project specifically aimed at developing and evaluating train-mounted impact-mitigating countermeasures. The goal of this thesis was to evaluate the effectiveness of a potential countermeasure and assess its benefit to public safety. The first step was to understand the distribution of impact conditions seen in the subway by studying incident reports. These statistics helped establish performance targets for the countermeasure and recognize design challenges related to train and station geometry. It was essential for the countermeasure to reduce impact severity and rebound. For this purpose, energy absorbing materials that exhibited the desired physical properties were identified and characterized through compression testing. The effectiveness of these materials was assessed through a combination of finite element simulations and sled tests. It was estimated that a countermeasure attached to the train front could reduce fatalities in the New York City subway by more than 80%, bringing the annual fatality count to under ten per year. A benefit-cost analysis was conducted using the predicted countermeasure effectiveness and rough cost estimates. Given the most conservative estimation for installation and maintenance cost, the net value of the project was evaluated to be one billion US Dollars over a 50-year period. This analysis indicates that a countermeasure could drastically improve public safety in the subway.

Table of Contents

Table of Figures

Table of Tables

Chapter 1. Introduction

1.1. Motivation

The New York City subway system is one of the oldest and largest in the world. It is an indispensable part of the city's transportation infrastructure but has also been the subject of growing public safety concerns. Many other subway systems, such as the London Underground, have implemented platform screen doors (PSD) to minimize the risk of pedestrians being hit by trains. Despite the effectiveness of these systems, implementing PSDs in the NYC subway has proven difficult for a variety of reasons. A 2020 study found that out of 472 stations, only 128 could accommodate platform doors [2]. Due to narrow platforms and obstructions, the installation of PSDs would cause accessibility issues in more than 40% of stations (Figure 1). An estimated 28% of platforms have structural problems that make them unable to bear the weight of platform doors (Figure 2). Both issues would require extensive station renovations to rectify. In addition to the infeasibility of PSD installations in most stations, the cost of installing doors within the 128 feasible stations would be between 6.5 and 7 billion dollars and the anticipated yearly maintenance would exceed 119 million dollars. For these reasons, the study determined that platform doors were not a practical solution to the public safety problem. Other proposed countermeasures, such as laser fencing, would be ineffective due to the high percentage of incidents that are suicides and the long braking distance of the subway trains. In summary, most safety measures intended to prevent pedestrians from falling on the tracks are infeasible, and active systems that alert train operators or deploy an airbag will be ineffective. To address the problem, the United States Federal Transit Administration (FTA) awarded the New York City Transit Authority (NYCT) a grant under its Safety Research and Demonstration Program (FTA-2020-004-TRI-SRD Design for Impact – An Innovative Approach to Train Front-End Safety and Collision Fatality Reduction). The focus of this project was to develop a technically feasible and cost-effective impact-mitigating device to reduce the lethality of train-pedestrian collisions.

Figure 1. Platform screen doors in narrow stations would hinder accessibility [2]

Figure 2. Overhanging platform which is structurally unable to bear the load of PSDs [2] source: wikipedia.org

1.1. Approach

The first step in addressing a public safety problem is to understand its root cause. Previous literature including medical examiner data was analyzed along with NYCT incident reports to determine the characteristics of the train-pedestrian impacts in terms of speed, location, and distribution of injury outcomes. The findings from this study were published in Transportation Research Record: Journal of the Transportation Research Board (summarized in section 1.2 [1]). Prior to testing, it was necessary to establish performance targets and evaluation metrics to assess the effectiveness of potential countermeasures (Chapter 2). These metrics were later used to estimate injury in simulations and sled tests. Based on the findings from the incident reports, the countermeasure concept was developed to address the injury mechanisms that were the most frequent causes of serious injury and death (Chapter 3). Preliminary simulations were conducted to help identify the range of material stiffness that would minimize injury in subway collisions (3.2). Energy attenuating materials that exhibited the desired physical properties were identified (3.3) and characterized through Instron testing (3.5). This data was later used to develop finite element (FE) models of these materials. Existing safety devices were also explored. Stunt airbags are widely used to prevent injury at speeds similar to those in subway collisions. An FE model of this device was developed and validated with test data (Chapter 4). While stunt airbags cannot be mounted on a train front, they serve as a point of comparison for other potential countermeasures. A sled test environment was constructed to replicate train-pedestrian collisions with a countermeasure implementation (Chapter 5). Sled tests were run with a variety of different countermeasure devices, and the injury criteria from these tests were compared with the accepted safety threshold established by NCAP (2.1). An FE model of the sled test environment was created and used to validate the material models of the energy attenuating materials (Chapter 6). This environment was then used to estimate the injury distribution at various impact speeds and pedestrian orientations. Countermeasure effectiveness was determined using these injury distributions (6.2). Based on the countermeasure effectiveness and rough estimates for the installation costs, a benefit-cost analysis was conducted to determine whether such a countermeasure would be economically worthwhile to implement (Chapter 7).

1.2. Incident Statistics and Epidemiology

The first goal of this project was to form a thorough understanding of the types of accidents that were happening in the subway. This included the location and root cause of incidents, impact conditions, injury mechanisms, and pedestrian demographics. These incident statistics were key to establishing performance targets for a potential countermeasure and identifying design challenges related to the station and train geometry. The investigation included a review of the current literature as well as an analysis of PTSB (Public Transportation Safety Board) incident reports. The incident reports provided data previously unavailable in the literature relating to the impact conditions, such as an estimate of the train pedestrian impact velocity, impact location, and relevant pedestrian characteristics. The PTSB reports relied heavily on eyewitness accounts for pre-impact conditions and lacked detailed post impact injury data. These reports were written by MTA employees, not medical professionals. Thus, there was very little detail pertaining to the types of injuries sustained by pedestrians or the root cause of the injury. Fatality statistics were calculated using PTSB reports and existing literature on the NYC subway incidents. Lin et al. [3], studied medical examiner reports between 2003 and 2007. While this paper did not contain any information relating to non-fatal cases or impact conditions, it did provide insight into the injuries sustained from impact and rollover. It also included data that overlapped with information available in the incident reports. The degree to which the incident statistics changed over time was determined by comparing the 2019 incident reports to the 2003-2007 medical examiner data. In 2019 there were over 180 reported collisions between a pedestrian and subway train, 54 of which resulted in fatality. A preliminary analysis of 2019 medical examiner records provided by the New York City Office of Chief Medical Examiners (OCME) suggests this number was closer to 65. Cases where the pedestrian was removed alive from the station and later expired at the hospital were often not marked as a fatality in the incident reports. By comparison, Lin et al. reported 211 fatalities during a 4-year period [3], also averaging more than 50 per year. The distribution of impact speeds from Hall et al. was given by the train event recorder [1]. The exact time of impact was unknown, so the impact speed was recorded as the time at which the train's emergency brake was activated. Consequently, the reported speeds likely overestimate the train speed at collision. Well over 90% of these train-pedestrian impacts happen at or below 35 mph (56 kph). Hall et al. also reported the incident locations, with over 95% of incidents happening within 200 feet of a station, and nearly 84% happening inside the station. According to the 2019 incident reports 83% of incidents involve male pedestrians, with a mean age of 40 years [1]. This figure resembled what was reported in by Lin et al. which reported 83% of subway fatalities were male [3]. Medical examiner data indicated that an overwhelming number of the fatalities in the New York subway are caused by blunt force trauma and many involve amputation, transection, or decapitation from contact with the wheels [3]. Both the incident reports and the medical examiner data agree that only a small fraction of fatalities was caused by electrocution. The baseline injury distribution was obtained from analyzed incident report data presented in Hall et al., 2023 [1]. Injuries from this publication were coded in the KABCO injury scale and had to be converted to AIS according to NHTSA guidance as shown in Table 1 [4]. The baseline injury distribution is shown in Figure 3. For further discussion on AIS see section 2.2 below.

Table 1. KABCO/Unknown – AIS Data Conversion Matrix [4]

AIS	O *No injury*	C *Possible Injury*	B *Non-incapacitating*	A *Incapacitating*	K *Killed*	U *Injured Severity Unknown*	# Non-fatal Accidents *Unknown if Injured*
0	**0.92534**	**0.23437**	**0.08347**	**0.03437**	**0.00000**	**0.21538**	**0.43676**
1	**0.07257**	**0.68946**	**0.76843**	**0.55449**	**0.00000**	**0.62728**	**0.41739**
2	**0.00198**	**0.06391**	**0.10898**	**0.20908**	**0.00000**	**0.10400**	**0.08872**
3	**0.00008**	**0.01071**	**0.03191**	**0.14437**	**0.00000**	**0.03858**	**0.04817**
4	**0.00000**	**0.00142**	**0.00620**	**0.03986**	**0.00000**	**0.00442**	**0.00617**
5	**0.00003**	**0.00013**	**0.00101**	**0.01783**	**0.00000**	**0.01034**	**0.00279**
6	**0.00000**	**0.00000**	**0.00000**	**0.00000**	**1.00000**	**0.00000**	**0.00000**

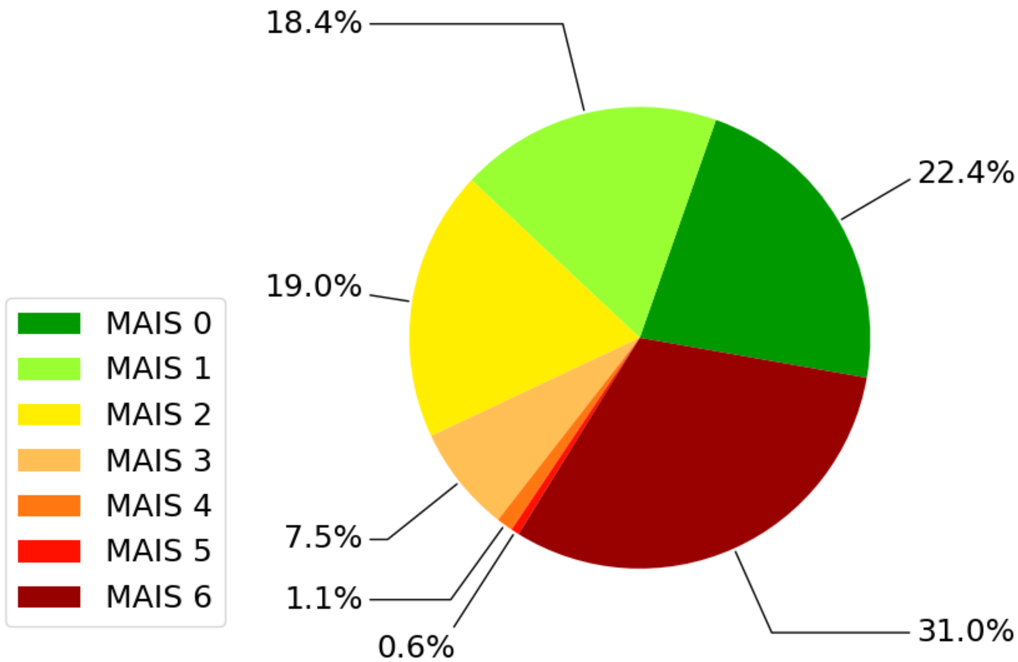

Figure 3. MAIS baseline injury distribution translated from incident reports.

Chapter 2. Countermeasure Evaluation Metrics

To evaluate the effectiveness of impact-mitigation countermeasures, it was essential to define objective and widely accepted safety metrics. In the absence of transit-specific injury thresholds, this study draws on established benchmarks from the automotive industry. The New Car Assessment Program (NCAP) assesses the crashworthiness of cars in rollover, frontal, and side impacts [5]. To evaluate car safety, NCAP provides injury criteria thresholds which constitute an acceptable level of injury risk to occupants. The fixed barrier frontal impact tests provided a good standard in which to compare the sled tests as they match in impact speed and surrogate. While these safety guidelines are authoritative, they can only be used to assess frontal impact tests with a Hybrid III dummy and cannot predict risk of injury or death. The injury risk from physical tests and simulations was calculated using Injury Risk Functions (IRFs) available in the literature. This approach allowed for a simulation or test to be mapped to an injury distribution for each body region, which was used to estimate the overall risk of death. Many of the IRFs used for this assessment were developed from a small number of tests and the confidence in the absolute injury risk predicted by these IRFs was limited. However, there was considerably higher certainty in relative injury risk predicted by this method than absolute risk. Thus, the injury risk from the countermeasure was compared to other effective safety measures under the same loading conditions. Airbags are widely used by professional stunt performers to break falls at speeds comparable to NYC subway collisions, and their ability to prevent injuries under such conditions is well documented. While it may be infeasible to mount low pressure airbags on a train front, peak loads and kinematics can be compared between airbag and countermeasure impacts to gauge whether the countermeasure produces a similar response.

2.1. NCAP

To understand the relative effectiveness of the countermeasures used in the sled tests, it was useful to compare these tests with an industry accepted safety standard. NCAP frontal impact tests provided a good benchmark for comparison as they match the sled tests in both impact speed (35 mph) and surrogate (Hybrid III) [5]. NCAP has a 5-star safety rating which evaluates vehicles based on occupant injury risk for head, chest, neck, and lower extremity. The US NCAP injury criteria for these body regions and their respective thresholds are shown in Table 2 [6]. The injury criteria from the sled tests was compared with the thresholds and 5-star NCAP tests. The Hybrid III was originally developed for occupant testing, and there were reasons to doubt the biofidelity of post impact kinematics of the dummy in pedestrian tests. For this reason, the focus of the injury analysis in the sled tests was on the primary impact.

Table 2. Injury criteria thresholds for US NCAP [6].

Injury Criteria	Units	Threshold
Head Injury Criteria (HIC_{15})	N/A	700
Maximum Chest Compression	mm	63
Nij	N/A	1
Neck Tension	N	4170
Neck Compression	N	4000
Femur Force	N	10008
Lower Tibia Axial Force	N	5200
Tibia Index	N/A	0.91

2.2. Abbreviated Injury Scale (AIS)

Injury outcomes from both simulation and physical testing were classified with AIS. AIS is widely used in automotive safety research to classify injuries by their risk of causing a fatality. All injuries are categorized according to a 6-point scale with AIS 6 describing the injuries that pose the greatest threat to life, and AIS 1 corresponding to injuries with little to no risk. A patient can sustain injuries to multiple body regions in a single incident. MAIS describes the maximum injury level sustained by an individual in all body regions [7]. For the injury analysis, the risk of fatality was based on MAIS. A 2013 study of automotive crash injuries quantified the average risk of mortality caused by an injury from a given MAIS category (Table 3). It is important to note that there is considerable variation in the risk to life posed by different injuries within the same AIS severity level. Some AIS 6 injuries, such as brainstem transection, result in a fatality nearly 100% of the time, while others such as major thoracic aorta laceration cause death less than 85% of the time [8]. Despite this limitation, it is reasonable to assume that the types of injuries from the data set used to develop this method are similar enough to those seen in train-pedestrian collisions.

Table 3. Risk of death by MAIS severity level [8].

MAIS Injury Severity Level	Risk of Death
0 No injury	0%
1 Minor	0%
2 Moderate	1%
3 Serious	3%
4 Severe	12%
5 Critical	43%
6 Fatal	85%

This was used to calculate countermeasure effectiveness based on an MAIS distribution (π_i) predicted by simulation or physical testing. Countermeasure effectiveness describes the relative proportion of fatal cases before and after the implementation of a countermeasure; a countermeasure that was 50% effective would prevent half of all fatalities. The effectiveness was computed according to Eq. 1 where F^B is the baseline proportion of fatalities and F^P is the projected proportion of fatalities. Eq. 2 shows the calculation for fatality risk given an injury distribution and risk of death R_i as shown in Table 3.

$$E = \frac{F^B - F^P}{F^B} \quad \text{Eq. 1}$$

$$F = \sum_i \pi_i * R_i \quad \text{Eq. 2}$$

2.3. Injury Criteria and Injury Risk Curves

AIS injury risk from simulation and physical testing was calculated using the appropriate IRFs from the literature. The selection of injury criteria and IRFs will depend on the surrogate and will be limited by its biofidelity and instrumentation. NCAP defined a particular set of IRFs and injury criteria that should be used for the injury assessment of the Hybrid III dummy. Injury criteria and IRFs used with THUMS and the MADYMO pedestrian model came from other publications. Table 4 summarizes the injury criteria used by surrogate and body region.

Table 4. Injury criteria by body region and surrogate.

Body Region	Hybrid III	Madymo Ped.	THUMS
Skull	HIC_{15}	HIC_{15}	HIC_{15}
Brain	DAMAGE/ BrIC	UBrIC	DAMAGE
Neck	Nij	Nij	Nij
Thorax	Chest Deflection	Chest Deflection	Rib Strain
Femur	Axial Force	Force and Moment	Axial Force
Tibia	RTI	Force and Moment	RTI
Ankle	Axial Force	Axial Force	Axial Force
Face			Nasal Force
Pelvis			Pubic Force
Wrist			Elbow Force

2.3.1. Head Injury Criterion

The Head Injury Criterion (HIC) is a metric for evaluating head injury risk that is formulated using linear head acceleration. Acceleration does not correlate well with brain injury; however, it has been shown to be predictive in determining the risk of skull fracture [9]. The HIC_{15} score is computed as shown in Eq. 3, where t2 - t1 $\leq$ 15 ms. The maximum value for this quantity over an acceleration pulse is used to calculate the risk of AIS 3+ skull injury (Eq. 4).

$$HIC_{15} = \left| (t_2 - t_1) \left[\frac{1}{t_2 - t_1} \int_{t_1}^{t_2} a(t)\, dt \right]^{2.5} \right|_{max} \qquad \text{Eq. 3}$$

$$P(AIS3+) = \Phi \left[\frac{\ln\,(HIC_{15} - 7.45231)}{0.73998} \right] \qquad \text{Eq. 4}$$

2.3.2. *Brain Injury Criterion*

The Brain Injury Criterion (BrIC) was developed as a rotational motion based metric for evaluating brain injury risk. The BrIC score is calculated using peak angular velocity and critical values (Table 5) for each of the principal axes (Eq. 5). Brain strain injury risk curves have been developed to map the BrIC score to AIS injury risk. The AIS 3+ IRF is shown in Eq. 6. According to the study that developed this criterion, angular acceleration did not correlate well with brain injury, and was excluded from the formulation [10]. Later studies contradicted this claim however, pointing out that high angular rates are observed in certain sports without any substantial brain injury risk. Ice skaters regularly exceed an angular velocity of 25 rads/s without sustaining brain injury, however BrIC predicts the AIS 3+ brain injury risk for these conditions to be over 20% [11]. BrIC is particularly prone to overpredicting injury in longer duration events with low angular acceleration.

$$BrIC = \sqrt{\left(\frac{\omega_x}{\omega_{xC}}\right)^2 + \left(\frac{\omega_y}{\omega_{yC}}\right)^2 + \left(\frac{\omega_z}{\omega_{zC}}\right)^2} \qquad \text{Eq. 5}$$

$$P(AIS3\,+) = 1 - e^{-\left(\frac{BrIC}{0.987}\right)^{2.84}} \qquad \text{Eq. 6}$$

Table 5. BrIC critical intercepts [10].

Axis	Critical Intercept (rads/s)
x	66.25
y	56.45
z	42.87

2.3.3. DAMAGE

DAMAGE or Diffuse Axonal Multi-Axis General Evaluation, was developed to replace brain injury criteria based solely on peak kinematics which tend to only be predictive for specific impact conditions. The DAMAGE injury criterion estimates brain strain using a three DoF spring damper system (Figure 4) driven by the angular acceleration time history [12]. This is calculated using an ODE solver, and the code for this computation can be provided upon request. Brain strain can then be used to estimate AIS 1+, 2+, and 4+ injury risk as shown in Eq. 7, Eq. 8, and Eq. 9 [13].

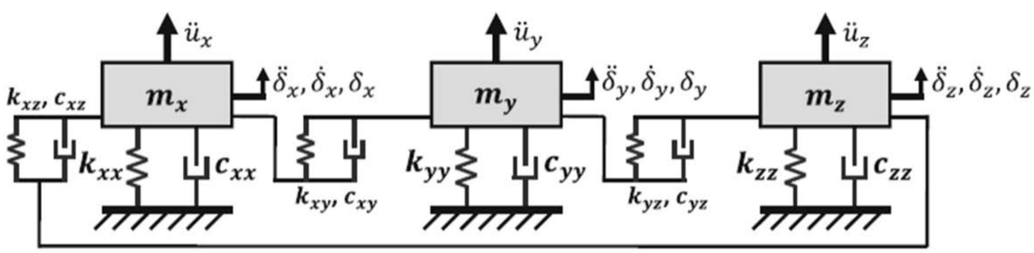

Figure 4. Three degree of freedom spring damper system used to evaluate brain strain [12].

$$P(AIS1+) = 1 - e^{-e^{4.078*\ln(0.957*DAMAGE+0.017)+3.798}} \quad \text{Eq. 7}$$

$$P(AIS2+) = 1 - e^{-e^{3.875*\ln(0.957*DAMAGE+0.017)+3.017}} \quad \text{Eq. 8}$$

$$P(AIS4+) = 1 - e^{-e^{6.051*\ln(0.957*DAMAGE+0.017)+2.644}} \qquad \text{Eq. 9}$$

2.3.4. Nij

The Nij injury criterion was developed to assess neck injury risk in frontal impacts. The metric is calculated as a linear combination of neck force and moment normalized by critical intercepts (Eq. 10). These intercepts depend on the type of loading, and the surrogate as shown in Table 6. It is worth noting that this neck injury metric will predict an ambient 4% AIS 3+ injury risk due to a non-zero intercept in the IRF (Eq. 11).

Table 6. Nij intercepts by loading type and surrogate [9], [14].

Dummy	Tension (N)	Compression (N)	Flexion (Nm)	Extension (Nm)
Hybrid III mid-sized male	4500	4500	310	125
THUMS	3000	3230	54.5	72.0
MADYMO Pedestrian	3000	3230	54.5	72.0

$$Nij = \frac{F_z}{F_{int}} + \frac{M_y}{M_{int}} \qquad \text{Eq. 10}$$

$$P(AIS3+) = \frac{1}{1 + e^{3.227-1.969*Nij}} \qquad \text{Eq. 11}$$

2.3.5. *Chest Deflection*

Due to differences in the mechanical properties of the Hybrid III dummy and the human body models (HBMs), separate IRFs had to be used to assess thoracic injury. The human chest experiences greater deflection under concentrated loading than distributed loading, while the deflection of the Hybrid III chest is less sensitive to loading type. According to Kent (2003), chest injury risk in human subjects correlates with chest deflection and is not dependent on loading type [15]. The result is that chest injury risk as predicted by the Hybrid III chest deflection will depend on loading type. For this reason, the chest IRF developed for the Hybrid III is not only a function of chest deflection, but also of loading type, as well as age, mass, and gender.

$$P(Injury) = \frac{1}{1 + e^{-q}} \qquad \text{Eq. 12}$$

$$q = \alpha + \sum_{i} \beta_i x_i \qquad \text{Eq. 13}$$

2.3.5.1. *Hybrid III Chest Deflection*

Because NCAP focuses on vehicle occupant tests, the chest IRF used for NCAP assessment is based on belt loading conditions. Belt loading IRFs yield higher risk than airbag loading IRFs for the same amount of chest deflection. Since loading conditions in the sled tests more closely resemble the distributed loading caused by an airbag, this IRF was used for the injury evaluation instead of the NCAP standard. Eq. 12 describes the AIS 3+ chest injury risk curve where q is a sum of model predictors and an intercept α as shown in Eq. 13. The model predictors are displayed in Table 7.

Table 7. Beta values for Hybrid III thoracic IRF where α = -14.4135 [15].

Predictor	β
Gender (male = 1)	-2.1944
Mass (kg)	-0.0425
Age (years)	0.0692
Sled Speed (km/h)	0.2518
Position (driver = 1)	1.0193
Restraint = airbag (no belt)	-8.4238
Restraint = combined	-3.8875
C_{max}	0.1696

2.3.5.1. Human Body Model Chest Deflection

Thoracic injury chest deflection based IRFs developed for humans (and FE HBMs) were based on the work done in Kent 2005 [16]. As these IRFs are developed for models with a biofidelic chest, there is no dependency on loading type. AIS 4 chest injury is predicted according to Eq. 12 and Eq. 13 with the beta values specified in Table 8.

Table 8. Beta values for human body model IRF where α = - 9.3189 [16].

Predictor	β
Age (years)	0.0474
Cmax	0.1838

2.3.6. Rib Strain

Most thoracic injury criteria are deflection-based formulations that are only predictive in certain loading conditions. Forman et al. (2022) provided a method for assessing thoracic injury risk using rib strain [17]. This approach is omnidirectional and can be fine-tuned for specific HBMs, making it an attractive alternative to deflection-based criteria. The rib fracture IRF was based on a Weibull formulation (Eq. 14), and uses age along with rib strain as predictors. The individual rib fracture risks are combined into an overall risk of 3+ or 7+ rib fractures according to the generalized binomial model. A combined optimization was conducted along with separate optimizations to tune the IRF parameters (Table 9) to predict 3+ and 7+ rib fractures. These IRFs are optimized to predict the global number of rib fractures and cannot be thought of as predictors of individual rib fractures. The result is that the 7+ IRF is the most sensitive to strain, and the 3+ IRF is the least sensitive (Figure 5).

$$P(fracture) = 1 - e^{-\left(\frac{strain}{e^{\beta_0 + \beta_1 * age}}\right)^{\alpha}} \qquad \text{Eq. 14}$$

Table 9. Parameters for strain-based rib fracture IRF [17].

IRF	β_0	β_1	α
3+ rib fracture	-3.0665	-0.0179	3.3562
7+ rib fracture	-3.72	- 0.0135	3.3562
Combined	-3.3696	- 0.016	3.3562

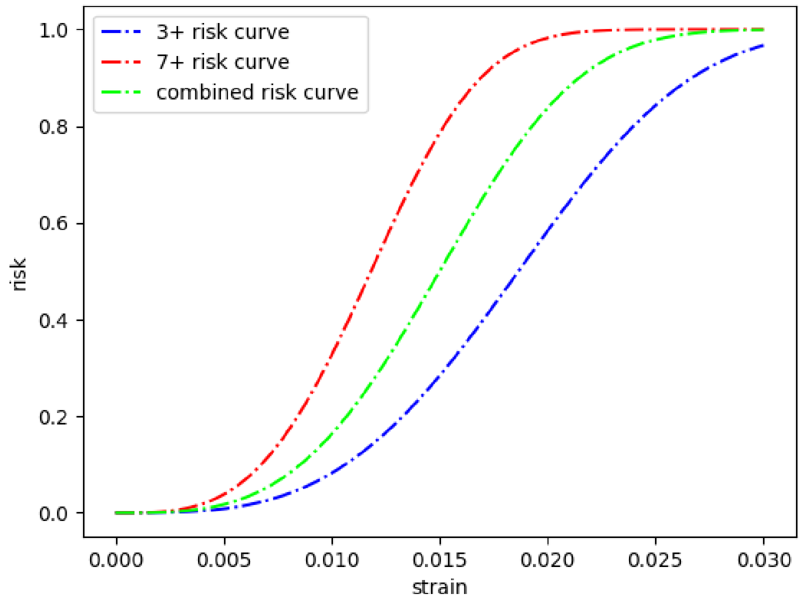

Figure 5. Strain-based rib fracture IRFs for a 45-year-old from Forman et al. (2022) [17].

For the purposes of this project, it was important to determine whether it was more appropriate to use the combined IRF, or the 3+ and 7+ IRFs. While the simulations used to optimize the IRFs were predominantly concentrated loading cases, the train project required an injury criterion that would be predictive in impacts with a soft countermeasure. After extensive analysis, it was determined that the 3+ and 7+ IRFs are predictive in concentrated loading scenarios, but do not extrapolate well to distributed loading cases (see the Appendix C. Strain-Based Thoracic Injury Criteria). For this reason, it was decided that it was more appropriate to use the combined IRF.

2.3.7. Femur Axial Load

Knee-thigh-hip injuries make up a significant percentage of lower extremity injuries in automobile crashes and thus are important to incorporate into the injury analysis. These injuries include patellar, femur and hip fractures, joint dislocations, and severe soft tissue damage. Kuppa et al. (2001) formulated AIS 2+ (Eq. 15) and AIS 3+ (Eq. 16) IRFs based on previous impact testing on cadaveric subjects. [18]. These IRFs used solely femur axial load as the predictor of knee-thigh-hip injury. The NCAP specified threshold of 10 kN (Table 2) corresponds with a 35% AIS 2+ injury risk and a 15% AIS 3+ injury risk.

$$P(AIS2+) = \frac{1}{1 + e^{5.7949 - 0.5196 * F_{femur}}} \quad \text{Eq. 15}$$

$$P(AIS3+) = \frac{1}{1 + e^{4.9795 - 0.326 * F_{femur}}} \quad \text{Eq. 16}$$

2.3.8. RTI

The Revised Tibia Index (RTI) was presented in Kuppa et al. (2001) as an improvement upon a previous tibia injury criterion [18]. RTI is used to predict tibial and fibular shaft fractures based on a linear combination of axial load and bending moment (Eq. 17). The axial load is measured along superior-inferior direction of the tibia, while the moment is defined as the resultant of the medial-lateral and anterior-posterior moments. Both the axial load and the moment are normalized by their respective critical values as shown in Table 10. The IRF for AIS 2+ injuries is shown in Eq. 18. The NCAP threshold for RTI of 0.91 (Table 2) corresponds with a 20% risk of AIS 2+ injury.

$$RTI = \frac{F}{F_c} + \frac{M}{M_c} \quad \text{Eq. 17}$$

$$P(AIS2\,+) = 1 - e^{-e^{\frac{\ln(RTI) - 0.2728}{0.2468}}} \quad \text{Eq. 18}$$

Table 10. Critical values for force and moment for Revised Tibia Index.

F_c	12 kN
M_c	240 Nm

2.3.9. Lower Tibia Axial Load

While tibial and fibular shaft fractures are caused by a combination of forces and moments, foot and ankle fractures closely correlate with axial loading alone. Kuppa et al. developed an IRF (Eq. 19) for predicting calcaneal, midfoot, talar, pilon, and ankle fractures based on axial load (kN) measured in the lower tibia [18]. This work was based on previous impact and axial loading tests conducted with PMHS. The NCAP injury threshold for lower tibia axial force of 5.2 kN (Table 2) corresponds with a 25% risk of injury.

$$P(AIS2+) = \frac{1}{1 + e^{4.572 - 0.670 * F_{tibia}}} \qquad \text{Eq. 19}$$

2.3.10. Pubic Force

Petitjean et al. developed an AIS 2+ (Eq. 20) and AIS 3+ (Eq. 21) IRF for predicting pubic symphysis injuries in side impacts [19]. Lateral pubic force as a predictor with age as a covariate. While these risk curves have been specifically developed for the WorldSID 50th dummy, they were used with THUMS for injury analysis in this thesis.

$$P(AIS2+) = \frac{1}{1 + e^{\frac{\ln(F_{pubic}) - (8.77482706 - age * 0.01385568)}{e^{-1.52587836}}}} \qquad \text{Eq. 20}$$

$$P(AIS3+) = \frac{1}{1 + e^{\frac{\ln(F_{pubic}) - (8.70406439 - age*0.01163987)}{e^{-1.82737827}}}} \quad \text{Eq. 21}$$

2.3.11. *Nasal Force*

The IRF for Nasal bone injury was developed by Cormier et al. (2010) using a series of rigid impactor tests on male cadaveric subjects to correlate impact force with nasal bone fracture [20]. The AIS 2+ IRF from the paper is shown in Eq. 22.

$$P(AIS2+) = 1 + e^{-((0.0013*F_{nose})^{1.65})} \quad \text{Eq. 22}$$

2.3.12. *Wrist*

The tests that were used to develop the wrist fracture IRF were presented in Forman et al. (2014) [21]. The tests were conducted using PMHS material in a drop tower device. The wrist and forearms were loaded by an impact hammer, and the resulting moment was measured at the elbow. The AIS 2+ risk curve for wrist fracture is described in Eq. 23.

$$P(AIS2+) = 1 + e^{-((F_{elbow}/3752.85)^{3.32035})} \quad \text{Eq. 23}$$

Chapter 3. Countermeasure Design

The countermeasure concept was designed to address the most common causes of serious injury and death in subway collisions. FEA was used to reach ballpark estimates of the material stiffness required to minimize injury in 35 mph collisions. Materials that have been used in similar impact mitigation applications were identified and down selected based on NYCT fire safety restrictions, and their sensitivity to environmental conditions. Selected materials were characterized with compression testing which was later used to create FE material models.

3.1. Design Concept

Based on the incident reports and medical examiner data, it was clear that while many injuries and fatalities were caused by direct impact with the train, many were also caused by secondary impact with the tracks and rollover. The track bed in the NYC subway contains a variety of potentially injurious features including crossties, metal rebar, and an electrified third rail (Figure 6). A potential countermeasure would need to soften impact with the train and prevent rebound onto the tracks. The impact-mitigating device would need to be paired with either wheel blocks or a scoop. Wheel blocks are cheap and fast to implement, but their effectiveness is difficult to evaluate and would likely be more injurious than a scoop. While the drainage pit has been shown to provide a survival space in cases of rollover [1], the fact that the track bed is not level with the rails makes the implementation of a scoop impossible. To remedy this problem, NYCT would need to implement a false floor in and around stations to create a level surface at the top of the rails. This would function like a level grade crossing and would also serve to cover injurious track geometry. Depending on the material used for the false floor, it may not be forgiving in the case of secondary impact. For this reason, it is important that the impact-mitigating device not only minimizes the severity of the primary impact but also reduces rebound. While active systems such as deployable airbags have been used for pedestrian safety on automobiles and light rail trams, there are several facts about the NYC subway incidents that make these an unattractive option. Given that around half of the incidents are suicides, and most of the impact speeds are above 20 mph [1], it is unlikely that an active countermeasure will be able to deploy in time while also preventing the pedestrian from rebounding onto the track. Hence, it is preferable for the impact-mitigating device to be passively deployed to avoid this problem.

Figure 6. Railbed features.

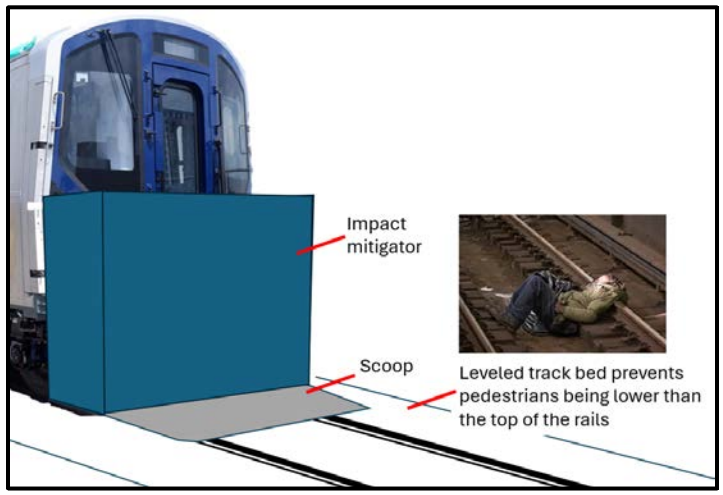

Figure 7. Design concept to address challenges posed by potentially hazardous track geometry.

3.2. Preliminary Simulations

The effectiveness of a potential train mounted countermeasure was estimated from coupled finite element multibody simulations. These simulations recreated train-pedestrian collisions with the addition of an energy absorbing countermeasure. Figure 6 illustrates the energy absorbing device, modeled as solid element, crushable (non-elastic) material, attached to the front of an R-160 subway train model. The R160 was used as the train front for this design as this model was associated with the largest number of subway pedestrians impacts [1]. The human surrogate was a multibody facet model that had been developed for analyzing car-pedestrian impacts and has been instrumented to output forces, moments, and kinematic data needed to determine the risk of injury. IRFs presented in Chapter 2 were used to map the relevant injury metrics to an AIS injury risk for each body region. To assess the fatality risk posed by these body region specific AIS risks, they were translated to an MAIS injury distribution. The Monte Carlo methods utilized for this purpose were similar to methods described in Bollapragada, 2019 [22]. For each simulation, virtual pedestrians were created by generating a random number between zero and one for each body region. These random numbers in combination with the injury risk gave an AIS score for each region (Figure 7). The highest AIS score for the virtual pedestrian constitutes its MAIS score. This process was repeated for over 10,000 virtual pedestrians to yield the MAIS distribution. The material stiffness of the theoretical countermeasure was optimized to reduce severe injury in a 35 mph collision with a 1.5 m thick device. This was done by scaling the stress-strain curve of the material model and analyzing the injury risk as a function of stiffness.

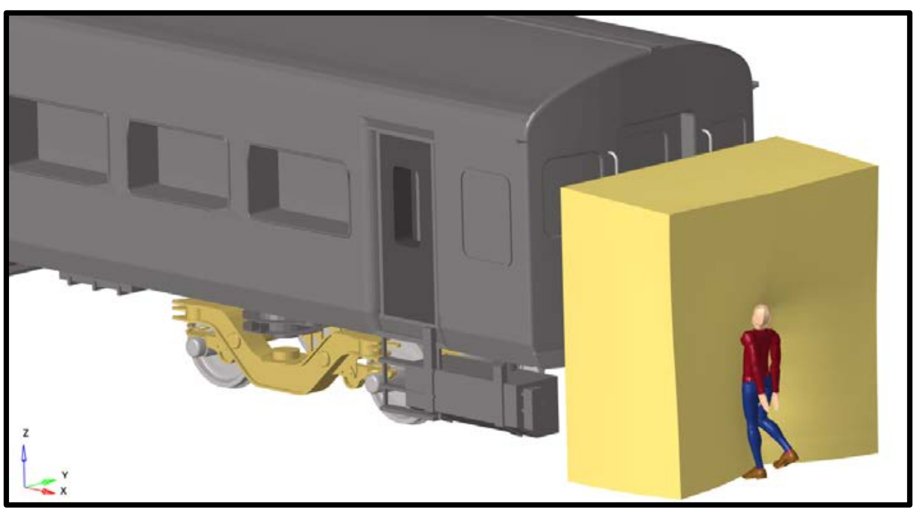

Figure 6. Coupled FE, multibody simulation of optimized countermeasure material used to estimate injury risk for various impact conditions.

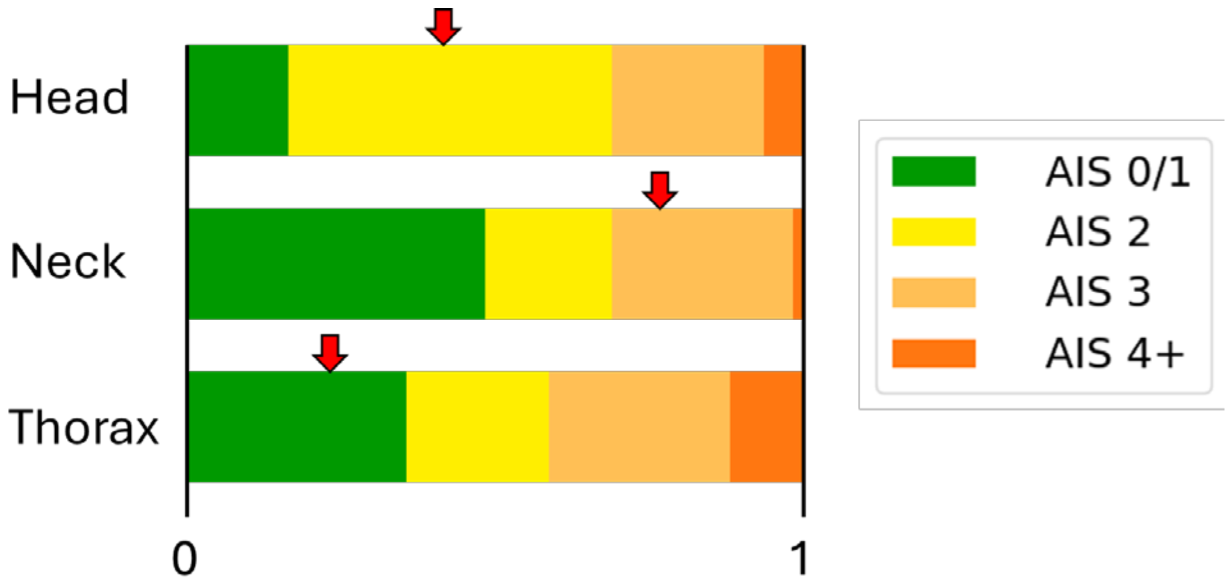

Figure 7. Illustration of Monte Carlo method for generating an MAIS distribution from AIS injury risk. A random number between zero and one was generated for each body region, and based on the injury risk an AIS score was assigned. The highest AIS score across all body regions constitutes the MAIS score for the virtual pedestrian. In this example, the virtual pedestrian has an MAIS 3 injury score.

Using this optimized material model, a larger set of simulations was used to formulate body region specific injury risks at a range of impact speeds. Monte Carlo methods were used to map these injury risks to a MAIS distribution for each impact speed as shown in Figure 8. Due to limitations of injury risk research, it was impossible to differentiate between AIS 4, AIS 5, and AIS 6 injuries. In the interest of making a conservative estimate for countermeasure effectiveness, AIS 4+ was treated as AIS 6. These distributions were then weighted by the relative frequency of occurrence as reported in Hall et al., 2023 [1] to yield the projected injury distribution (Figure 9). Treating AIS 4+ injuries as AIS 6, this injury distribution represents an 84.3% reduction in fatal cases when compared to the baseline. In the best case, where AIS 4+ injuries are AIS 4, the countermeasure would have 92.7% effectiveness.

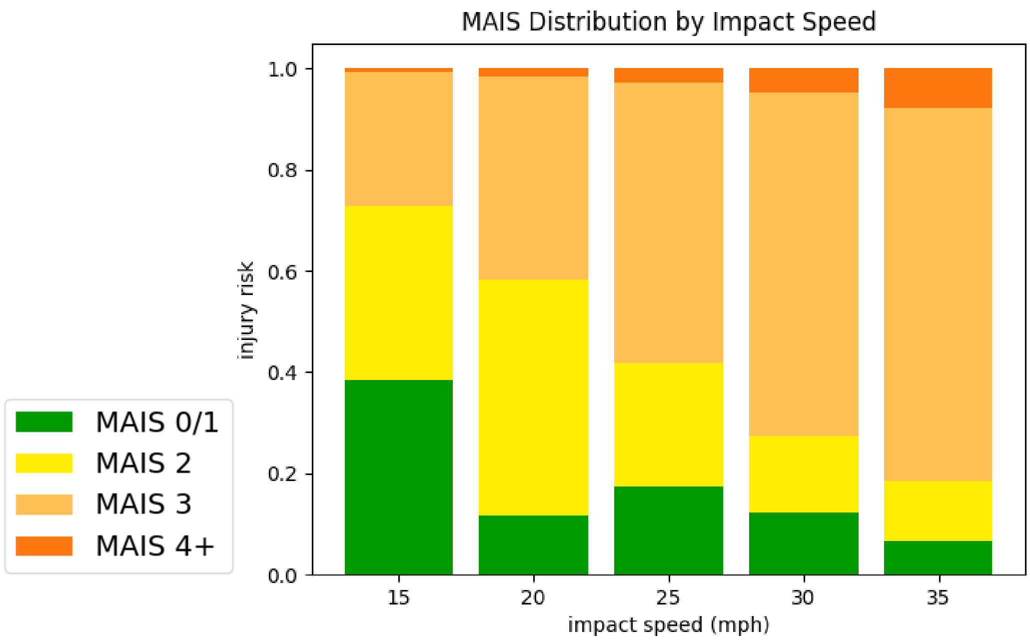

Figure 8. Injury distributions at varying impact speeds as predicted by finite element simulation.

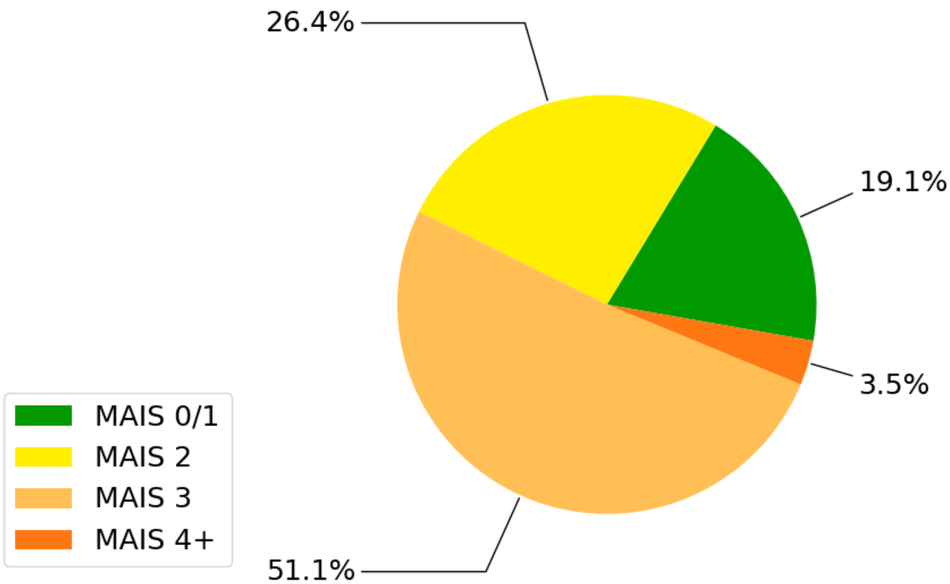

Figure 9. Projected injury distribution from weighting distributions from Figure 8 by the frequency of impact at the corresponding speed.

3.3. Material Selection

Material selection for the impact-mitigating device was based on engineering judgement, design constraints provided by NYCT, and preliminary simulations that provided bounds on stiffness. While reducing the severity of the primary impact was the main concern, the incident reports and medical examiner data indicated that a substantial number of fatal injuries were sustained from secondary impact with the railbed and rollover. It was important for the countermeasure to attenuate as much of the impact energy as possible to minimize rebound. It was also preferable to select a material that has a plateau in its stress-strain curve as opposed to a linear relationship, as this will reduce the peak loading the pedestrian is subjected to. While certain materials may perform well in the laboratory, it was also necessary to consider how various environmental conditions within the NYC subway may influence countermeasure performance or cause it to degrade over time. Some materials become stiff in cold weather causing them to be ineffective at mitigating impact. Others may be adversely affected by rain or moisture, especially those that are prone to absorption. NYCT also has stringent fire safety regulations which require all materials used in or around the subway to meet ASTM-E84 standards. Several energy attenuating materials were identified that displayed most of the desired physical characteristics. Open cell urethane foams were an attractive option because they are already manufactured and used for impact mitigation purposes, such as in gymnastics mats. There is also a large variety of urethane foams available from vendors that have a wide range of densities and stiffness. CF-40 Confor foam was identified as the urethane foam with the best physical properties. Despite these advantages, open cell urethane foams are highly porous and prone to absorbing water. This causes them to become incompressible when fully saturated. They also exhibit temperature sensitivity, causing them to become stiff in subzero temperatures as demonstrated by tests in the lab. Polystyrene foam, also known as EPS, Styrofoam or geofoam does not suffer from temperature sensitivity or water absorption that urethane foams do. Polystyrene is used for a wide variety of industrial applications and does not easily degrade even in harsh conditions. While EPS deforms plastically, and cannot be reused after impact, it is typically cheaper than urethane foam. Unfortunately, both polystyrene and urethane foams do not meet ASTM-E84 fire safety standards, which is required by NYCT to be used in the subway. There are foams made from non-flammable hydrophobic materials such as silicone. Silicone foams do not suffer from temperature sensitivity nor are they absorbative. They are durable and can be reused after impact. However, these foams are more elastic than polystyrene or urethane foam and thus return more energy on impact as shown in Figure 10.

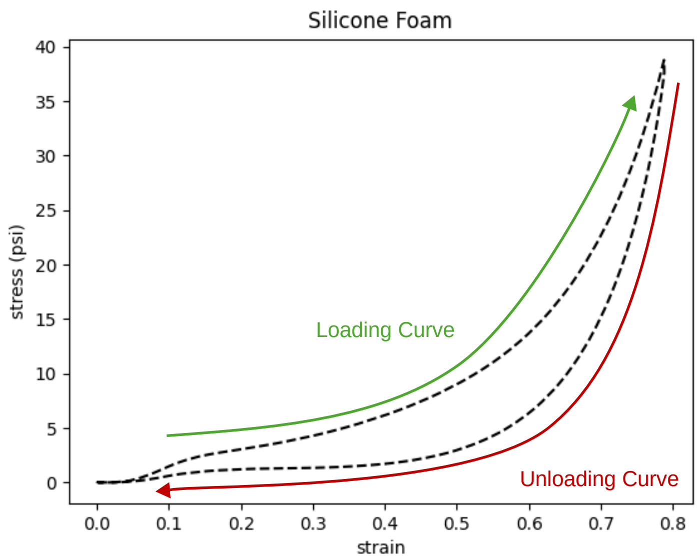

Figure 10. F12 silicone foam stress-strain curve obtained through Instron compression testing (section 3.5).

Aluminum honeycomb is a material that has been used frequently for impact mitigation purposes due to its good energy attenuation properties. As shown in Figure 11, aluminum honeycomb exhibits a high level of hysteresis, thus minimizing the energy returned after impact. Aluminum has no fire safety problems, nor is it temperature sensitive. The downside of honeycomb is that it is not reusable, and commercially available products are orders of magnitude too stiff to be used for the impact-mitigating device. This problem can be solved through coring as discussed in section 3.4. Despite its drawbacks, aluminum honeycomb was determined to be more viable for the countermeasure application than the other materials discussed in this section. An overview of the pros and cons of potential countermeasure materials is provided in Table 11.

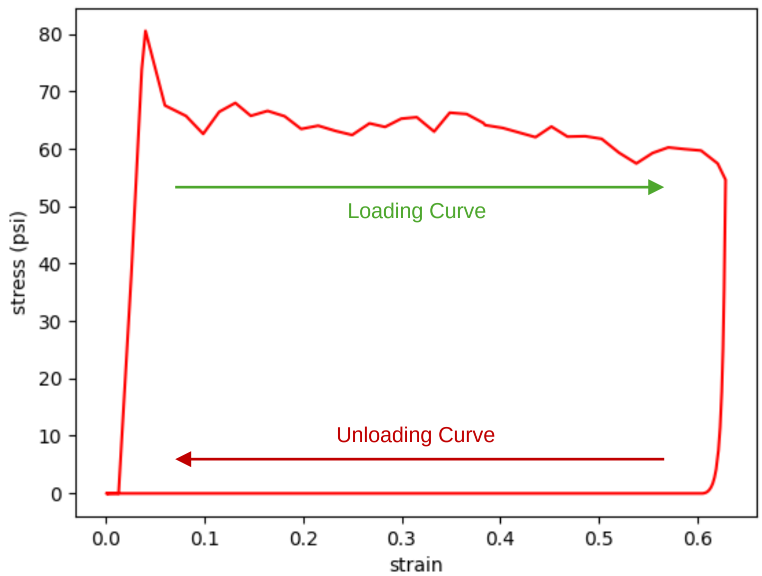

Figure 11. Aluminum honeycomb stress-strain curve exhibits high hysteresis, most kinetic energy is attenuated on impact. Stress-strain curve obtained through Instron compression testing (section 3.5).

Table 11. Material characteristics for potential countermeasure materials.

	Polystyrene Foam	Urethane Foam	Silicone Foam	Aluminum Honeycomb
Water Resistant	✓	✗	✓	✓
Temp. Resistant	✓	✗	✓	✓
ASTM-E84 Compliant	✗	✗	✓	✓
High Hysteresis	✓	✓	✗	✓
Desirable Stiffness	✗	✓	✓	✗
Reusable	✗	✓	✓	✗
Appx. Cost per ft^3	$5	$135	$800	$25

3.4. Honeycomb Fabrication

At present, commercially available honeycomb is too stiff for use in this application, however through coring and other techniques which remove material, the effective stiffness can be reduced to more desirable levels. Honeycomb is manufactured using thin sheets of aluminum bonded together with epoxy to form hobs. These hobs can then be expanded into honeycomb. Given the target stiffness of just under one psi, a hole pattern was developed to achieve this property. This toolpath was used by a Tormach CNC machine to cut the appropriate pattern in the unexpanded honeycomb hobs. The resulting honeycomb is shown in Figure 12.

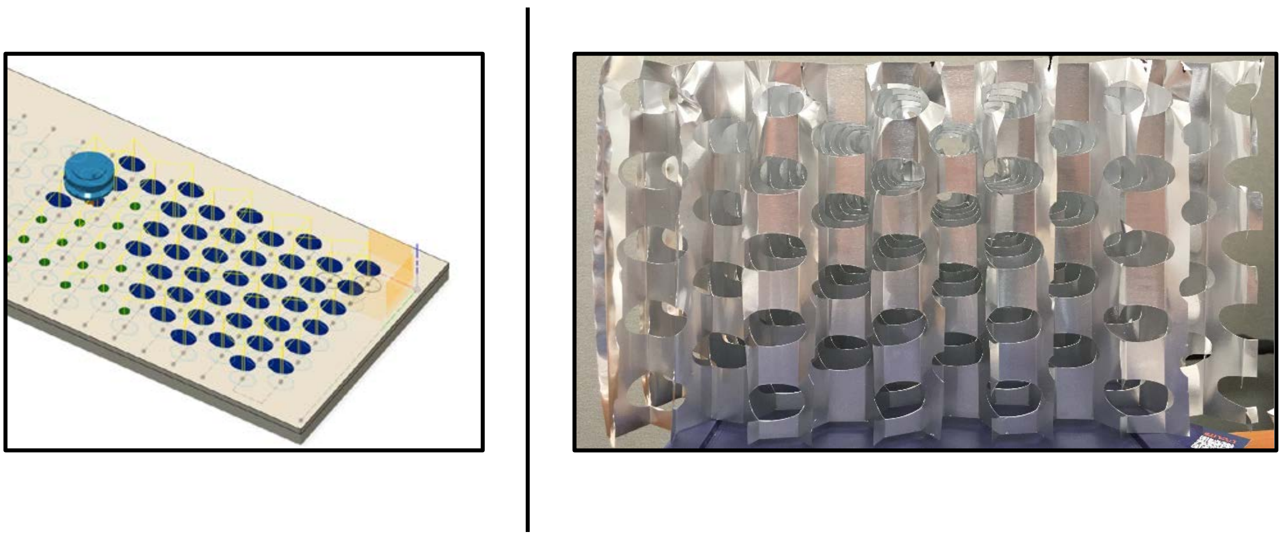

Figure 12. CNC tool path for the coring process and the resulting cored honeycomb.

3.5. Material Characterization

The two most promising materials, aluminum honeycomb and silicone foam, were characterized through compression testing using both an Instron machine and a Kuka robot. Load cells were used to obtain force vs displacement which were then translated to stress-strain curves. Two different types of silicone foam were tested on the Instron machine at various strain rates (Figure

13). While the foams did exhibit favorable physical properties, the use of them for the sled tests was infeasible due to their prohibitive cost, and a material model was not developed.

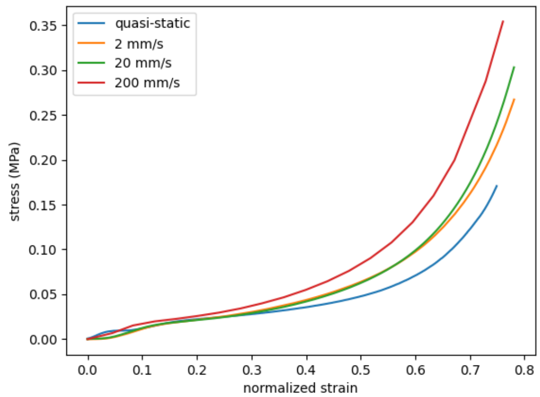

Figure 13. Silicon foam stress-strain curves at increasing strain rates.

The initial round of honeycomb testing used available honeycomb samples, and not the honeycomb that would later be used in sled tests. The purpose of this experiment was to further understand the stress-strain relationship along the three principal axes and to develop an initial material model (Figure 14). While the stiffness of the honeycomb in the off-axis directions fell within the desired range, it also returned a significant amount of energy during the unloading phase which would result in rebound during an impact (Figure 15). The honeycomb exhibited high hysteresis in the axial direction but was roughly two orders of magnitude stiffer than what was required to minimize injury in 35 mph impacts.

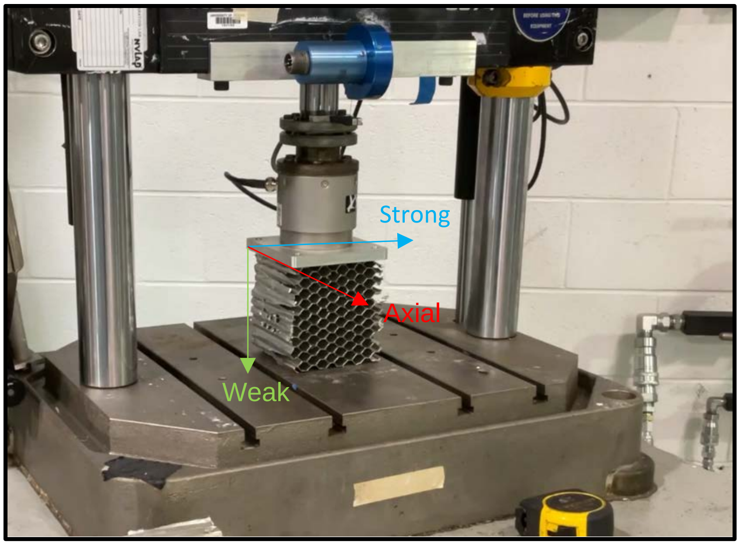

Figure 14. Honeycomb oriented in off-axis direction tested on Instron.

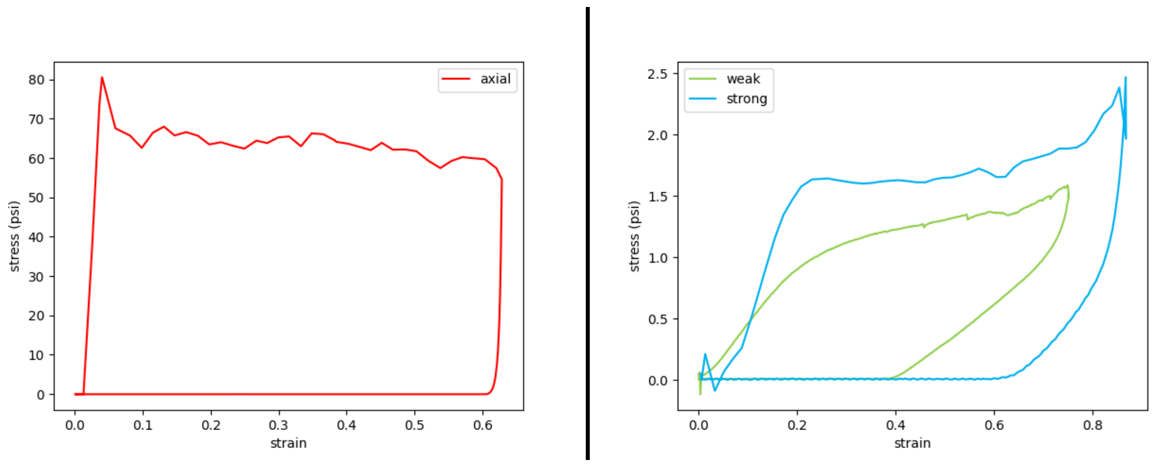

Figure 15. Stress-strain curves for 3/4 in. cell size honeycomb.

Further compression testing was conducted using Cellbond honeycomb. While this honeycomb was still too stiff for application in the impact-mitigating device by roughly an order of magnitude, the stiffness could be controlled through coring. Figure 16 shows the stress-strain curves for the Cellbond honeycomb before and after coring. The cored honeycomb had a plateau stress of just under 1 psi, which was deemed optimal for injury prevention. For further details on the optimization process see section 6.2.

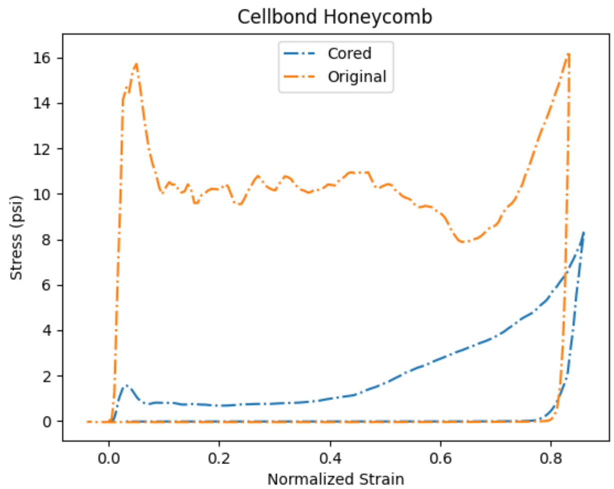

Figure 16. Cored and un-cored Cellbond honeycomb stress-strain curves.

3.6. Material Model Development

Aluminum honeycomb is a difficult material to model due to its geometry and its complex modes of failure. Previous publications have typically approached modelling honeycomb in one of two ways. The most straight forward approach is to use solid elements with the MAT_MODIFIED_HONEYCOMB material model, which allows the user to define stress-strain curves for each of the principal material axes. According the LS-DYNA manual, these material definitions assume that the honeycomb is an anisotropic material with uncoupled material axes and a Poisson's ratio of zero in the uncompressed configuration [23]. The highest fidelity method for modelling honeycomb is to recreate the cell geometry using shell elements and an aluminum material model. While this approach has been shown to produce marginally better results than the solid element formulation, it requires a much smaller mesh size to accurately capture the buckling of the honeycomb [24]. As a result, the shell element model is far more computationally expensive to use. Furthermore, every new honeycomb coring pattern would require the shell part to be remeshed to match the geometry. For these reasons the solid element formulation was used for the simulation work in this thesis. Stress-strain data from the compression testing was translated directly into load curves for the material card. Given that the material axes are uncoupled and that the loading would primarily happen along only one axis, it was deemed appropriate to increase the stiffness of the material in the transverse directions to improve the stability of the model. It was confirmed through simulation that scaling the transverse stiffness had a minimal effect on the response when loaded in the axial direction.

Chapter 4. Airbag Characterization and Model Development

As mentioned in Chapter 2, stunt airbags have been widely used in the entertainment industry to break falls at speeds exceeding that of most NYC subway accidents. While there have been incidents of misuse resulting in injury [25], when used properly stunt airbags are almost completely effective at preventing injuries. The passive inflation pressure of stunt airbags is typically less than 0.25 psi gauge pressure, which makes it impractical to mount these on train fronts. However, these airbags can serve as a standard in which to compare potential countermeasures. Drop tests were conducted to understand the external loads imparted by the airbag on impact as well as the internal pressure response. This data was used to develop a FE airbag model that would later be used to recreate the sled test environment.

4.1. Airbag Drop Tests

4.1.1. Methods

An i2k AirPad was used for the testing, the exact specifications of which are described in the Countermeasures section of Appendix A. The airbag has four base chambers with the blower inlet and vent outlet located in the same chamber. Each base chamber has five to six fingers, all of which are covered by, and fastened to a tarp (Figure 17). The tarp is connected to the base chambers with elastic cords. Testing was performed at a range of heights between 6 and 30 ft with two different vent configurations (Table 12). An initial set of drops was conducted at 6 ft to establish the repeatability of the tests.

Table 12. Testing matrix for drop tests by vent configuration and drop height.

Vent Size	6 ft	12 ft	24 ft	30 ft
3 in		DROP29	DROP30	DROP33
Open Vent	DROP27	DROP28	DROP31	DROP32

Figure 17. Larger i2k AirPad model provided for visualization. Source: i2kairpad.com

The test setup involved the Hybrid III positioned face-up above the i2k stunt airbag (Figure 19), suspended from a solenoid drop release mechanism pictured in Figure 18. The airbag was instrumented with a pressure transducer to monitor the airbag pressure during impact. The dummy was connected via umbilical to a test laptop. All data acquisition systems and the drop release were triggered simultaneously to ensure synchronization. Data from these tests was filtered according to SAE recommendations as detailed in the Data Acquisition and Filtering section of the Appendix.

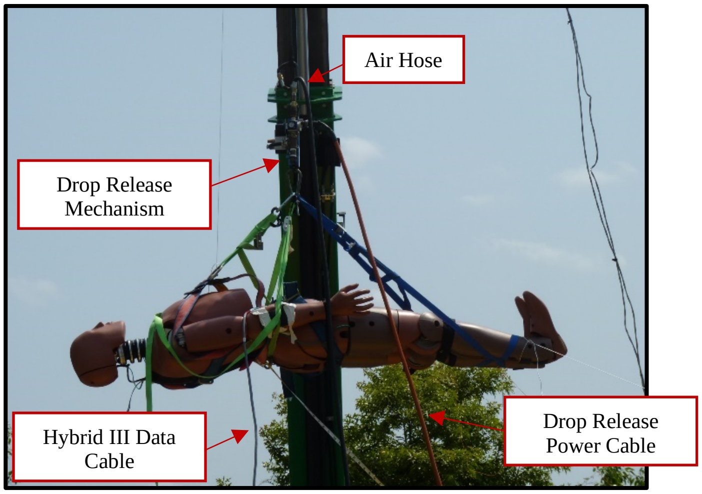

Figure 18. Hybrid III dummy suspended from solenoid drop release mechanism.

Figure 19. Experimental setup for airbag drop test.

4.1.2. Results

The Hybrid III chest acceleration and airbag pressure for the restricted vent tests is displayed in Figure 20. The data for the open vent tests is displayed in Figure 21. Of note, the varying vent configurations had a minimal effect on the peak internal pressure and peak acceleration during impact. The internal pressure of the airbag in Drop 32 and 33 peaked at 2 psi despite Drop 33 having a restricted vent. The peak acceleration for these tests varied by less than 3 g's, with the open vent drop reaching a higher peak acceleration (23.9 g). The restricted vent drop, despite having lower peak acceleration, produced a larger rebound.

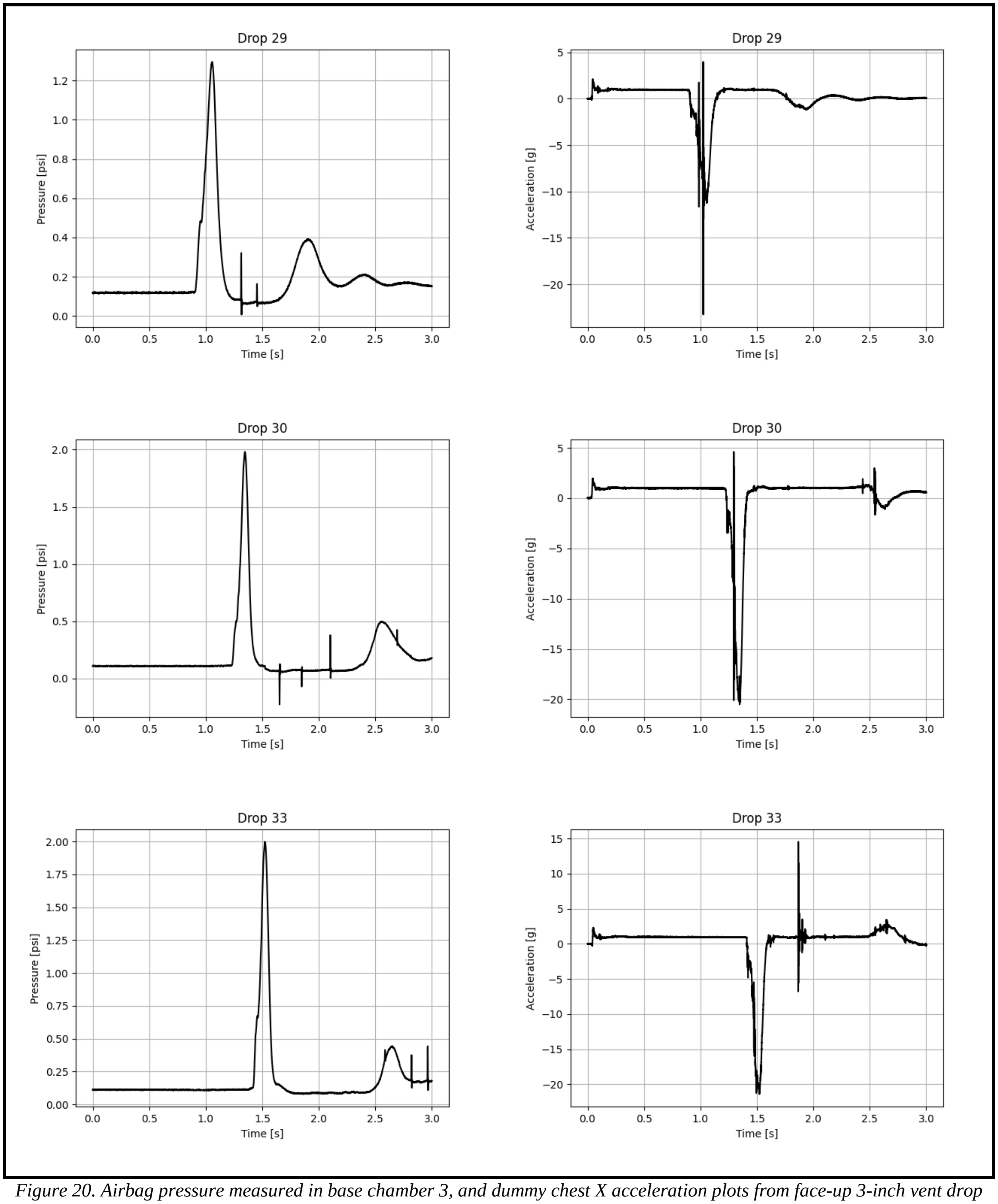

Figure 20. Airbag pressure measured in base chamber 3, and dummy chest X acceleration plots from face-up 3-inch vent drop tests.

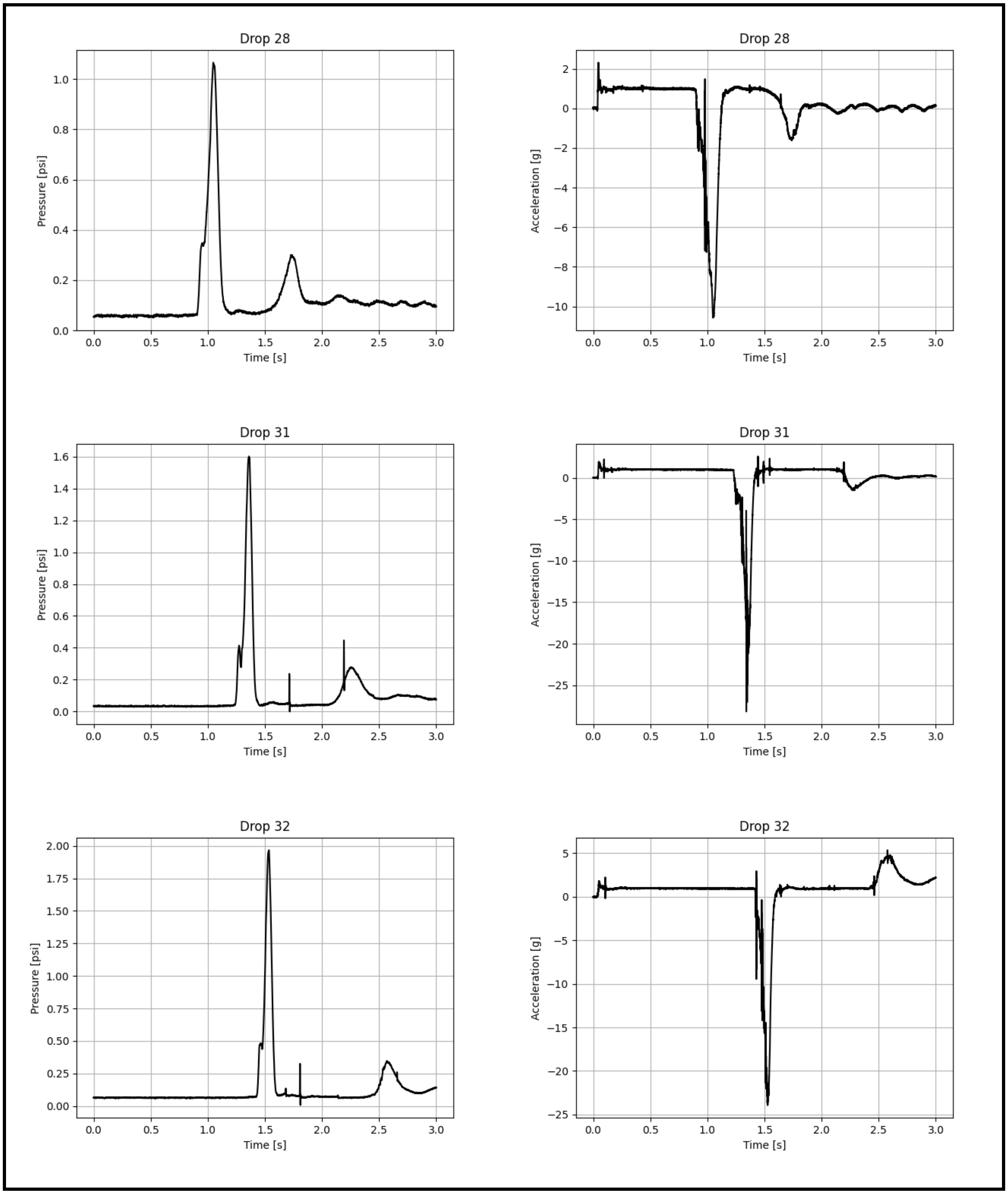

Figure 21. Airbag pressure measured in base chamber 3, and dummy chest X acceleration plots from face-up open vent drop tests.

4.2. Finite Element Airbag

Physical tests provided an important link to reality, but they were slow and time consuming. Additionally, the Hybrid III dummy has more limited injury prediction capability than many of the FE HBMs. For these reasons it was important to develop an FE model of the airbag that could be used to explore a broader range of impact conditions. The airbag model was developed based on the available specs of the i2k airbag. The model included the airbag fingers, cover, elastic cords, blower, and a vent in the base chamber (Figure 22).

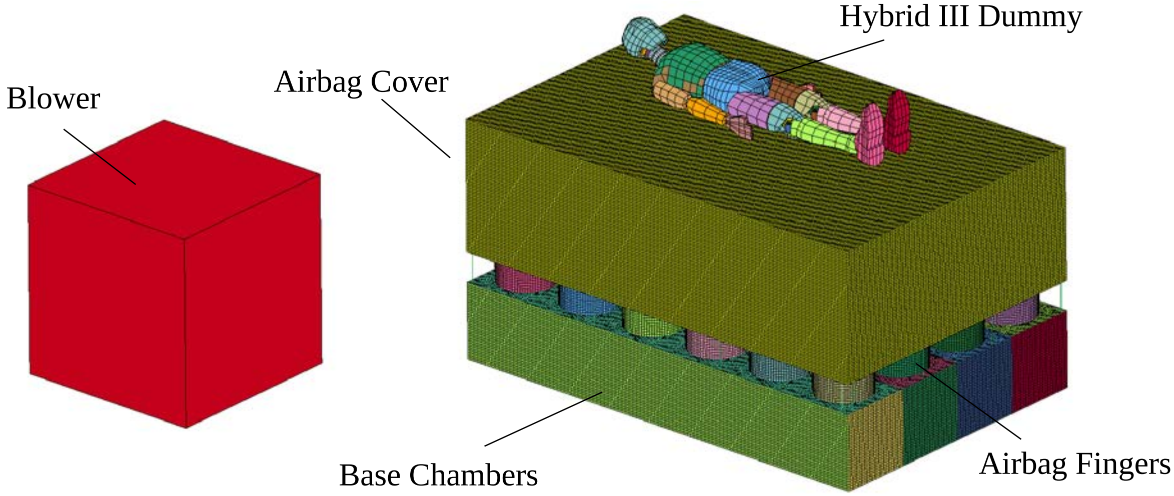

Figure 22. Finite element LS-Dyna airbag model based on the specs of the i2k airbag.

4.2.1. Model Development

The airbag cover and chambers were created as shell element parts with the MAT_FABRIC material model. The internal pressure calculations were handled through the AIRBAG_SIMPLE_AIRBAG_MODEL keyword. The pressure in each airbag chamber is calculated according to Eq. 24 where ρ is the mass density of air in the control volume, e is the specific internal energy, and γ is the ratio of specific heats [23]. The pressure is applied as a load along the normal direction of each shell element in the part [26]. The change in air mass within a control volume is calculated at each time step as the difference between the inflow and the outflow (Eq. 25). The inflow and could be a defined mass flow rate or air acquired from another control volume with higher pressure. Likewise, the outflow is air lost to another chamber or the environment through a vent.

$$p = (\gamma - 1)\rho e \qquad \text{Eq. 24}$$

$$\frac{dM}{dt} = \frac{dM_{in}}{dt} - \frac{dM_{out}}{dt} \qquad \text{Eq. 25}$$

The physical dimensions of the airbag such as the size of the chambers and orifices were translated directly into the FE model. The model allows air to flow freely between all four base chambers and the connected fingers. Air is expelled from the airbag through a fixed-area vent. To capture the effect of the airbag's internal pressure on mass flow rate, the blower chamber was modelled as a fixed volume airbag with a constant mass flow rate inlet and an outlet vent (Figure 23). The outlet was treated as a variable area vent that increased in size with increasing pressure. In steady state, air flows from the blower to the base chambers. During impact air can move back through the orifice to the blower, reducing the peak pressure in the airbag during these events. Several of the airbag parameters were optimized to match test data. While the volume flow rate of the blower at zero gauge pressure was reported by the manufacturer, the reduction in flow rate as the airbag inflates was unknown. The leakage through the airbag membrane was also difficult to estimate. These parameters were optimized to match test data as described in section 4.2.2.

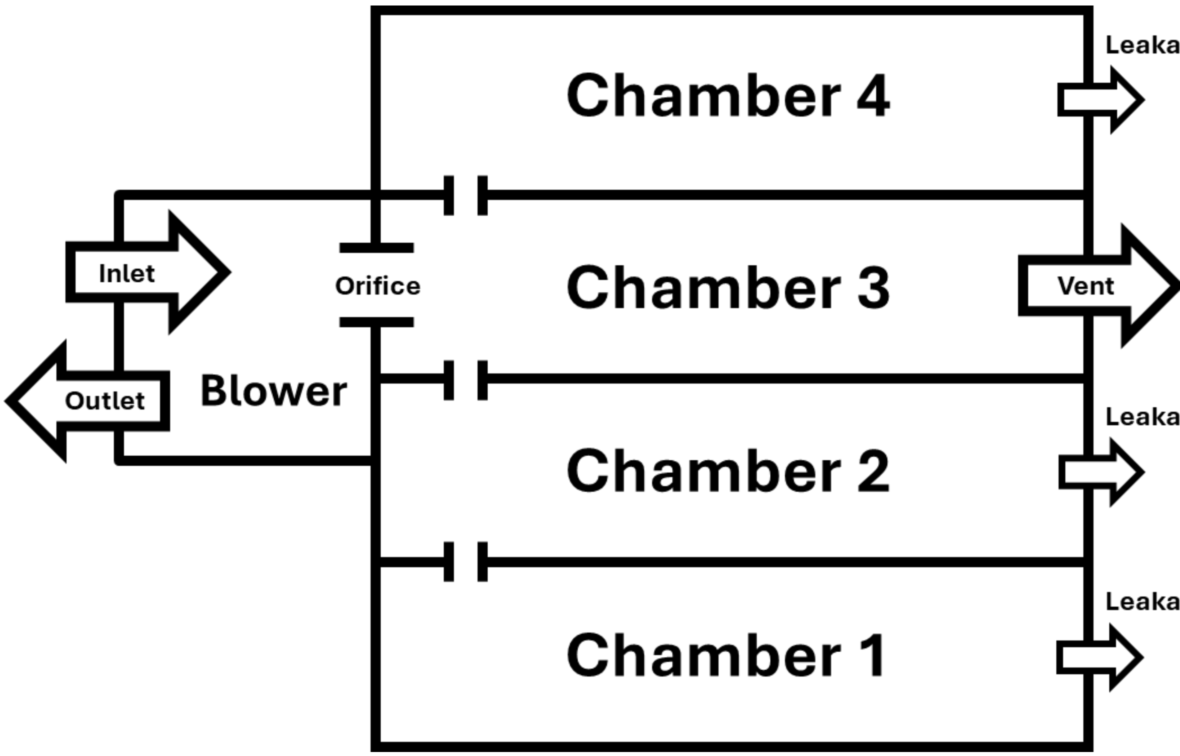

Figure 23. Airbag model diagram detailing the airflow between the various airbag chambers.

4.2.2. Drop Test Simulations

The airbag model had two free parameters to optimize to match the i2k airbag's response. The optimization was done using the 12 ft drop test. The 24 ft and 30 ft tests were then used to verify that the airbag model extrapolated well to higher energy impacts. The tests were simulated with a Hybrid III dummy model placed above the FE i2k airbag. The airbag was given one second to inflate, then the dummy was prescribed a downward velocity equal to that of the equivalent drop test just before impact. The results of the drop tests were compared to the equivalent simulations as shown in Figure 24. The acceleration time history matched up well between the tests and simulations at all three heights. Peak pressure matched well at 12 and 24 ft, but the simulation overpredicted peak pressure by roughly 0.4 psi at 30 ft.

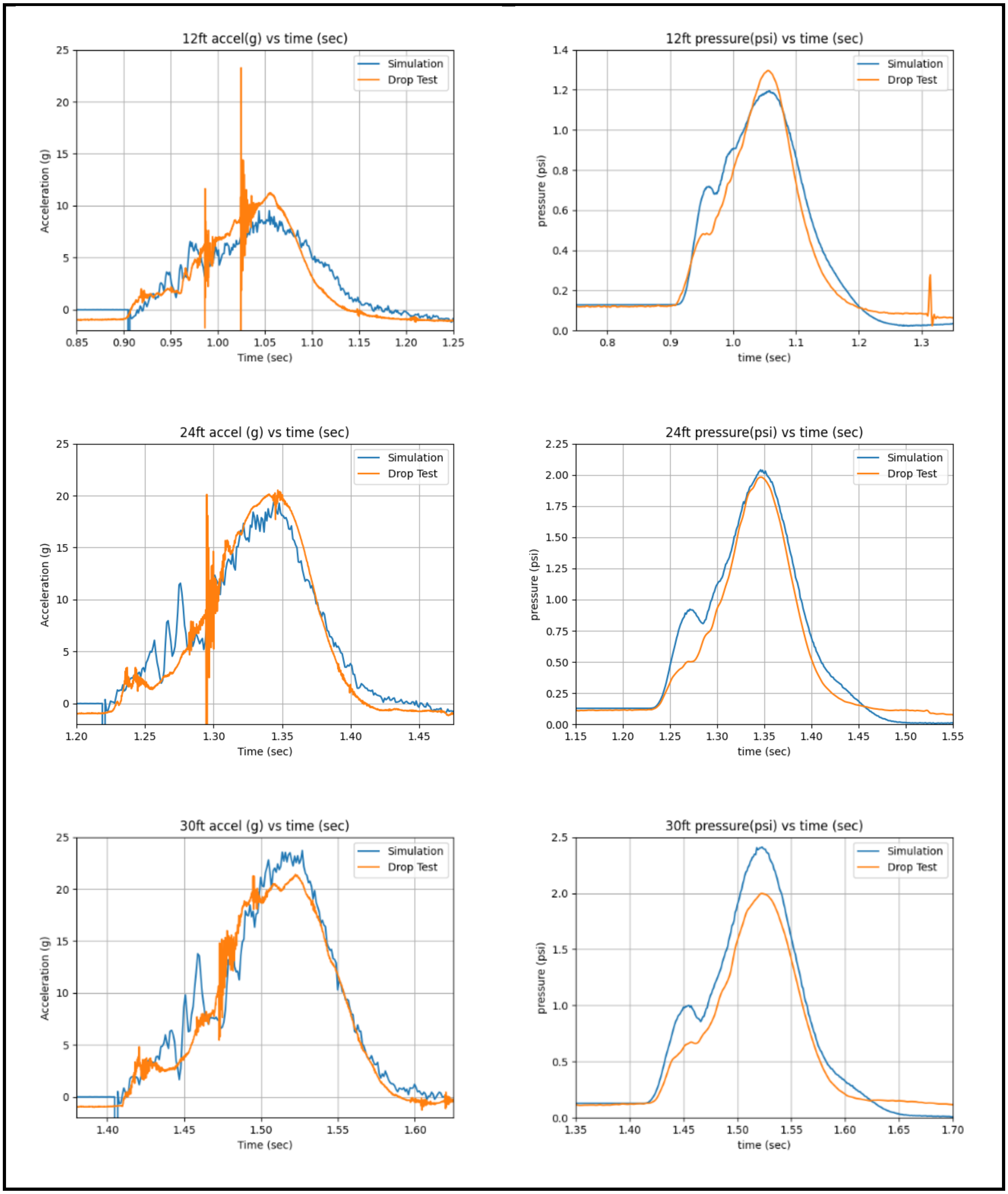

Figure 24. Acceleration and pressure comparison between drop tests and simulations.

Chapter 5. Sled Tests

Following the drop tests, a series of sled tests was planned to evaluate countermeasure effectiveness in terms of reducing injury and rebound within the range of impact speeds seen in subway incidents. Creating a test setup that was representative of accidents seen in the NYC subway requires an understanding of the distribution of impact conditions (section 1.2). Preventing serious injury and death at 35 mph was a stated performance target for the countermeasure as more than 90% of train-pedestrian collisions happen below this speed [1]. The sled tests focused on 35 mph impacts but also explored lower speeds to assess the rebound and scoop performance under various conditions. An overwhelming majority of incidents happened in or near stations [1], meaning that it is within the realm of practicality to install a false floor within these areas. The sled test environment was designed to approximate a levelled track bed rather than one with crossties and a drainage trough. The age and sex of the pedestrians hit by the subway trains was also relevant for determining the type of surrogate used in the tests and evaluating injury risk from test data. The 50th percentile male Hybrid III dummy was considered appropriate for this study, given that most recorded cases involve male pedestrians (83%). The tests were run with a variety of postures seen in NYC subway incidents (Table 13). Two types of countermeasures were tested - a stunt airbag and a crushable aluminum structure. Four different aluminum countermeasures were tested, the first two preliminary tests were conducted with countermeasures constructed using aluminum trays (see Countermeasures section in the Appendix). The first honeycomb test involved honeycomb custom fabricated in the lab. Based on these tests, FE simulations were used (section 6.2) to determine the optimal stiffness for reducing injury in 35 mph impacts. Cellbond honeycomb was cored to have the desired stiffness (section 3.4). The cored honeycomb was used in the final sled test (Test 35). These countermeasures were judged on several criteria. Injury risk was assessed according to the appropriate injury metrics and IRFs for the Hybrid III dummy (section 2.3). However, due to limitations of the Hybrid III, there was reason to doubt the absolute predicted injury risk. To control for this, the injury risk from the honeycomb sled runs was compared to the airbag tests. If the countermeasures produced similarly low injury risk to the airbag, it could be concluded that they would be sufficiently effective at reducing injury. Additionally, injury criteria from these sled tests was compared to NCAP accepted thresholds as described in section 2.1.

Table 13. Test matrix for VIA sled tests.

Dummy Posture	10 mph	25 mph	35 mph
Front facing		Test 23 (Airbag)	Test 24 (Airbag) Test 31 (Stacked Trays) Test 32 (Sealed Trays) Test 34 (Fabricated Honeycomb) Test 34 (Cored Honeycomb)
Side Facing		Test 27 (Airbag)	
Back Facing		Test 25 (Airbag)	
Lying	Test 30 (Airbag)	Test 26 (Airbag)	
Seated		Test 28 (Airbag) Test 29 (Airbag)	

5.1. Methods

The test setup involves a Hybrid III positioned on the sled which was accelerated down the track towards the countermeasure using a pneumatic propulsion system. The countermeasure was positioned on top of the stage (Figure 55) which also housed a pneumatic telescoping assembly that deployed a scoop on dummy impact. This assembly was powered by a separate pressure tank held behind the stage as shown in Figure 56. A trigger switch mounted on the stage was set to trigger the offboard Data Acquisition System (DAS), cameras, and telescoping scoop on impact. The Hybrid III onboard DAS triggered separately. To simplify the test setup, the impact kinematics were reversed in the sled tests, with the dummy being projected into a stationary countermeasure. After impact, the sled was stopped using a hydraulic decelerator. The test sequence was shown in Figure 25 and Figure 26. The cameras, sled velocity gate and the pressure tank deployment valve for the telescoping scoop assembly were connected to the trigger distributor box (Figure 28).

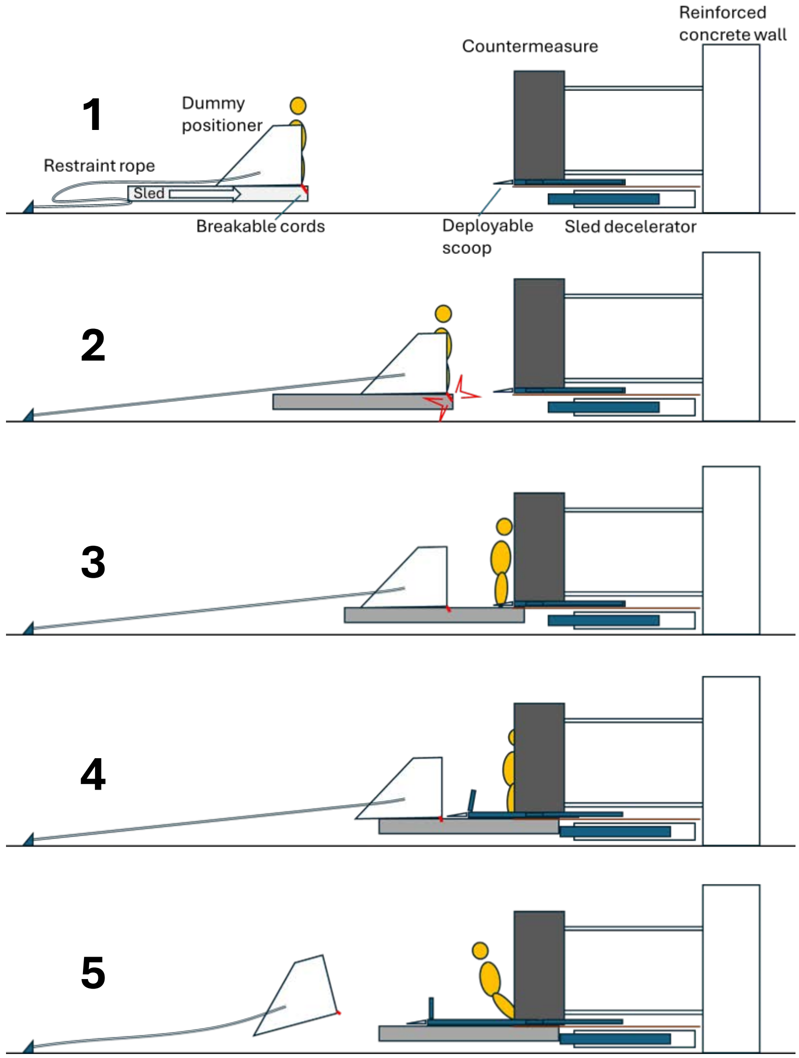

Figure 25. Test sequence. 1) Sled is accelerated down the tracks by the pneumatic propulsion system. 2) Restrain ropes become taught, causing the cords to break and the positioner to release the dummy. 3) The dummy impacts the countermeasure. 4) The scoop deploys, and the sled is stopped by the decelerator. 5) The dummy rebounds onto the sled.

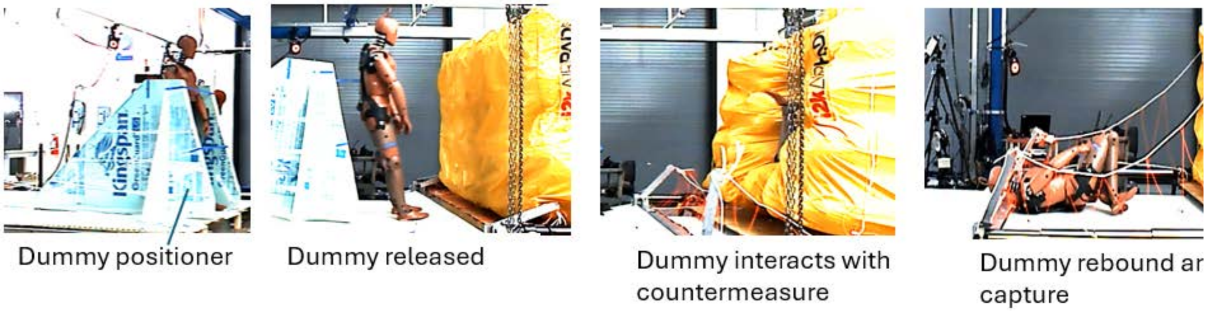

Figure 26. Test sequence with airbag countermeasure.

Critical test components were tracked using VICON cameras. Markers were attached to the dummy and countermeasure to assess dummy kinematics and countermeasure deformation during impact. An array of 14 VICON cameras were set up in the VIA sled room to capture motion of the dummy, positioner, sled, scoop, and the countermeasure surface. Four high speed video cameras (MEMRECAM Q2s) were used to capture test motion at 1000 frames per second (Figure 27).

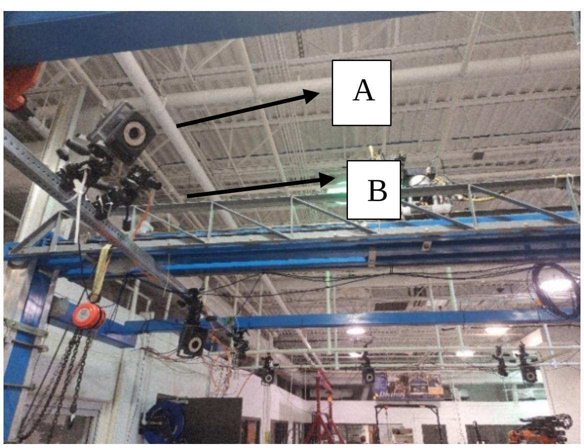

Figure 27: A) VICON. B) Highspeed video cameras

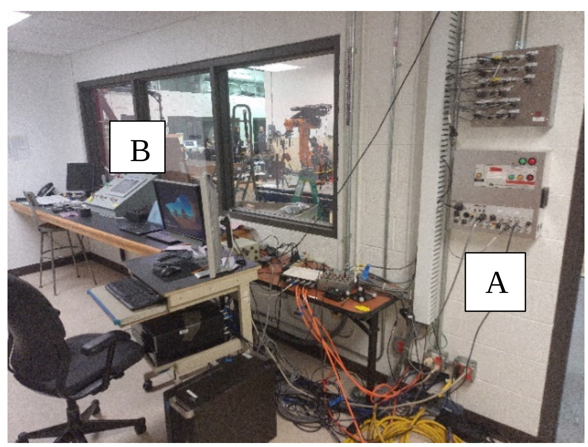

Figure 28: VIA Control room. A) Trigger distributor box. B) VIA systems controller

5.2. Results and Discussion

Table 14 summarizes the test observations. The instrumentation in the right leg of the Hybrid III was damaged in Test 24, and thus the injury analysis for the right leg was missing for Test 24 through 31, and Test 35. The primary impact injury analysis (Table 15) was done using test data from trigger time until the dummy leaves the countermeasure. The filtered data for the 35 mph tests is shown in Figure 29. Dummy penetration into the countermeasure was measured using VICON. In the case of the crushable aluminum countermeasures, these measurements were confirmed posttest.

Table 14. Observations for VIA sled tests.

Test Number	Observations
23	Significant rebound.
24	Very high rebound, dummy bounced off sled. Right lower extremity sensor failures.
25	Significant rebound.
26	Low rebound.
27	Significant rebound.
28	Scoop failed to deploy due to a trigger switch failure. Changed the position of the switch for future tests.
29	Low rebound.
30	Low Rebound.
31	Small Rebound. It may have been due to tarp trampolining because the tarp perimeter was screwed to the countermeasure frame.
32	No rebound. Fixed the right lower extremity sensor failures.
33	The dummy fell onto the rails before impact. Test incomplete.
34	No rebound. The knee of the dummy hit the stage after impact, resulting in higher femur forces.
35	Low rebound, dummy successfully captured with deployable scoop.

Table 15. Primary Impact Injury Analysis

Dummy Posture			Lying		Seated	Back Facing	Side Facing	Front Facing					
Target Speed (mph)			10	25					35				
Countermeasure			Airbag							Trays (Stacked)	Trays (Sealed)	Fabricated Honeycomb	Cored Honeycomb
Test Number			30	26	29	25	27	23	24	31	32	34	35
Skull		HIC15	1.1	48.8	22.3	102.9	192.0	27.4	84.6	179.2	72.7	168.8	68.0
		AIS 3+	0%	0%	0%	0%	0.2%	0%	0%	0.1%	0%	0.1%	0%
Brain		BrIC/ Damage	0.26/ 0.14	0.57/ 0.26	0.39/ 0.16	0.44/ 0.22	0.46/ 0.33	0.18/ 0.08	0.43/ 0.21	0.31/ 0.24	0.29/ 0.22	0.46/ 0.28	0.59/ 0.29
		AIS 2+ (Damage)	1.3%	12.0%	2.0%	6.2%	25.5%	0.2%	5.8%	8.7%	6.8%	14.8%	15.8%
		AIS 3+ (BrIC)	2.3%	19.1%	6.8%	9.5%	10.7%	0.8%	8.9%	3.6%	3.1%	10.6%	20.3%
		AIS 4+ (Damage)	0%	0.5%	0%	0.2%	1.8%	0%	0.2%	0.3%	0.2%	0.7%	0.8%
Neck		N_{ij}	0.07	0.27	0.62	0.30	0.88	0.6	0.74	1.47	1.31	1.48	0.53
		AIS 3+	4.4%	6.3%	11.8%	6.7%	18.2%	11.5%	14.5%	41.8%	34.2%	42.3%	10.2%
Chest		C_{max} (mm)	0.6	4.2	2.5	2.5	2.9	17.4	18.9	24.1	20.0	21.8	22.2
		AIS 3+	0%	0%	0%	0%	0%	0%	0%	0.1%	0.1%	0.1%	0.1%
Right	Femur	Force (kN)						2.37			3.63	8.49	
		AIS 2+						1.0%			2.0%	20.0%	
		AIS 3+						1.5%			2.2%	9.9%	
	Tibia	RTI						1.21			1.31	2.43	
		AIS 2+						51.4%			62.6%	100%	
	Ankle	Force (kN)						2.71			4.28	10.20	
		AIS 2+						6.0%			15.4%	90.5%	
Left	Femur	Force (kN)	0.14	0.68	2.18	2.65	3.06	2.02	4.27	5.06	4.32	6.22	4.25
		AIS 2+	0.3%	0.4%	0.9%	1.2%	1.5%	0.9%	2.7%	4.1%	2.8%	7.1%	2.7%
		AIS 3+	0.7%	0.9%	1.4%	1.6%	1.8%	1.3%	2.7%	3.5%	2.7%	5.0%	2.7%
	Tibia	RTI	0.19	0.29	1.17	2.16	2.00	1.48	1.49	1.61	2.03	1.95	1.49
		AIS 2+	0.0%	0.23%	46.0%	99.9%	99.6%	80.6%	80.9%	89.7%	99.7%	99.3%	81.4%
	Ankle	Force (kN)	0.07	0.21	2.61	2.05	2.46	2.36	4.85	5.85	5.16	7.71	4.89
		AIS 2+	1.1%	1.2%	5.6%	3.9%	5.1%	4.8%	21.0%	34.3%	24.7%	64.4%	21.5%

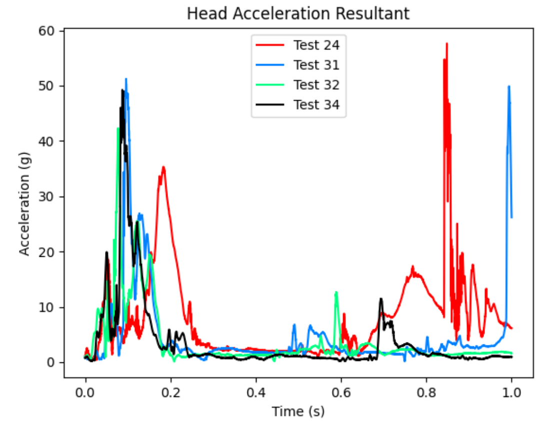

Head Acceleration

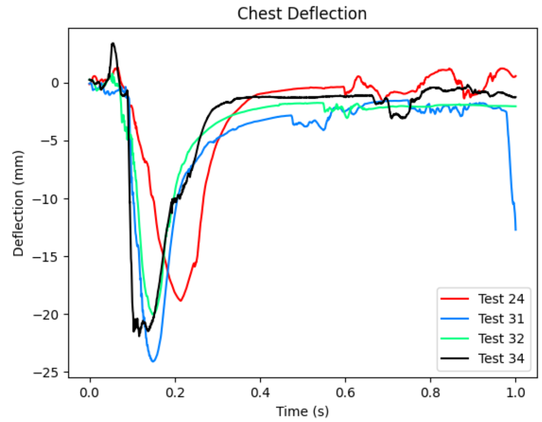

Chest Deflection

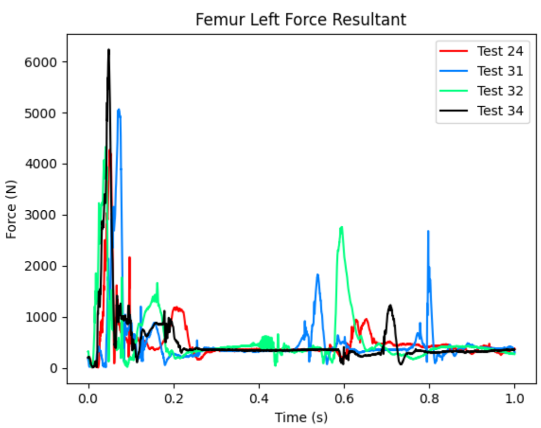

Femur Left Force

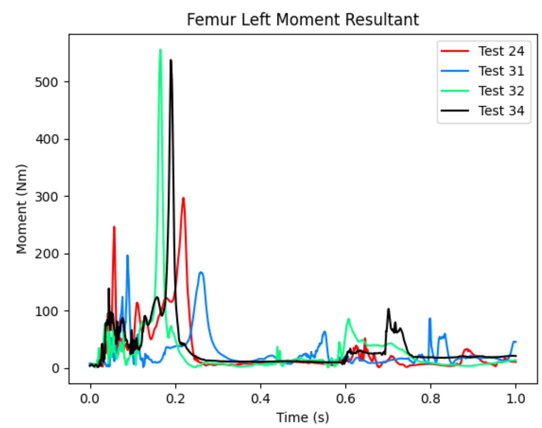

Femur Left Moment

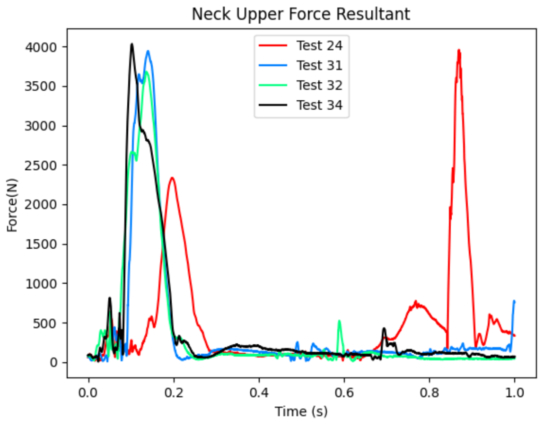

Neck Upper Force

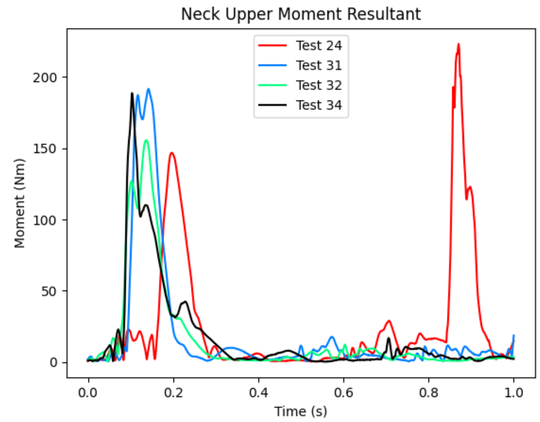

Neck Upper Moment

Figure 29. Filtered data for 35 mph sled tests.

Serious and severe injury risk was low for the primary impact across all tests for the skull, brain and thorax. There was notably high injury risk for the neck and lower extremity. In these cases, the contribution to the Nij injury score came primarily from axial loading as opposed to bending moment (Figure 30).

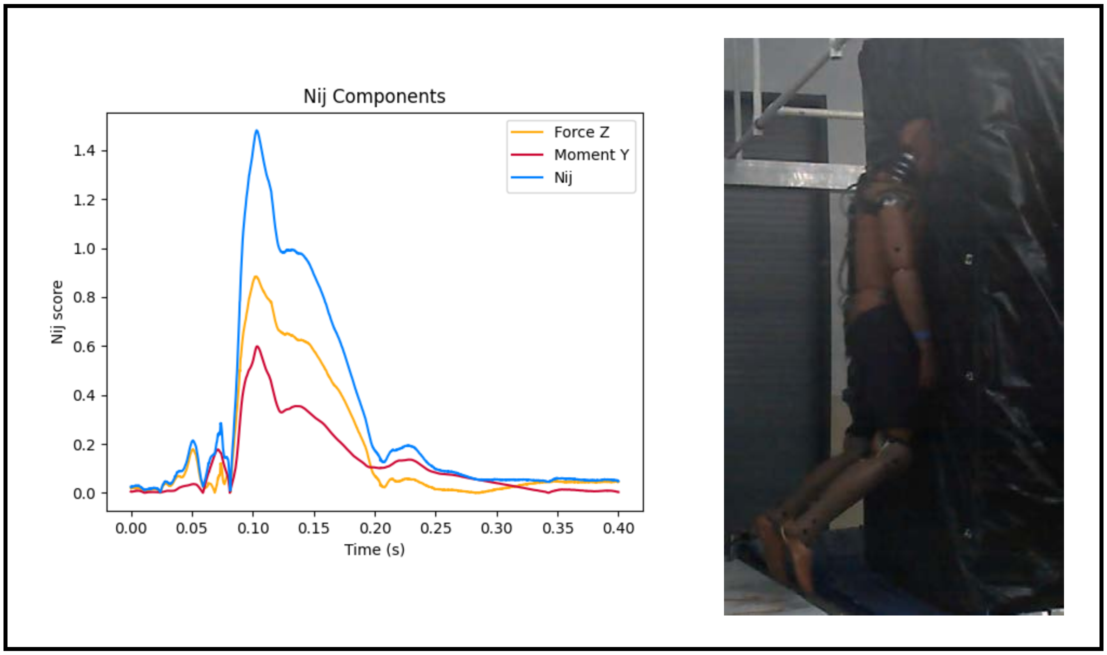

Figure 30. Nij contribution from axial force and moment Test 34.

Due to differences in the environment and limitations of the Hybrid III, the sled test secondary impact was not representative of the type of secondary impact seen in NYC subway. The countermeasure implementation includes a false floor or rubber grade crossing to raise the track bed to the level of the rails. While this is more forgiving than the current station geometry, the false floor is firmer than the plywood surface of the sled. Additionally, the post-impact kinematics of the Hybrid III are not representative of a human subject due to non-biofidelic joint stiffness and a lack of muscle tone. For these reasons, the injury analysis for the secondary impact should be viewed with limited confidence but still illustrates the importance of preventing rebound. Injury risk from secondary impact remained low for most tests with some notable exceptions. The rebound in Test 23 was relatively mild, but the Hybrid III head landed on the aluminum scoop, which resulted in a HIC score of 506 (Figure 31). Test 24 had a substantial rebound but produced a much lower HIC score of 172 due to the dummy's head landing on the plywood surface of the sled rather than the aluminum scoop. This impact did however cause a significant bending moment in the neck corresponding with a Nij score of 2.66 (Figure 32).

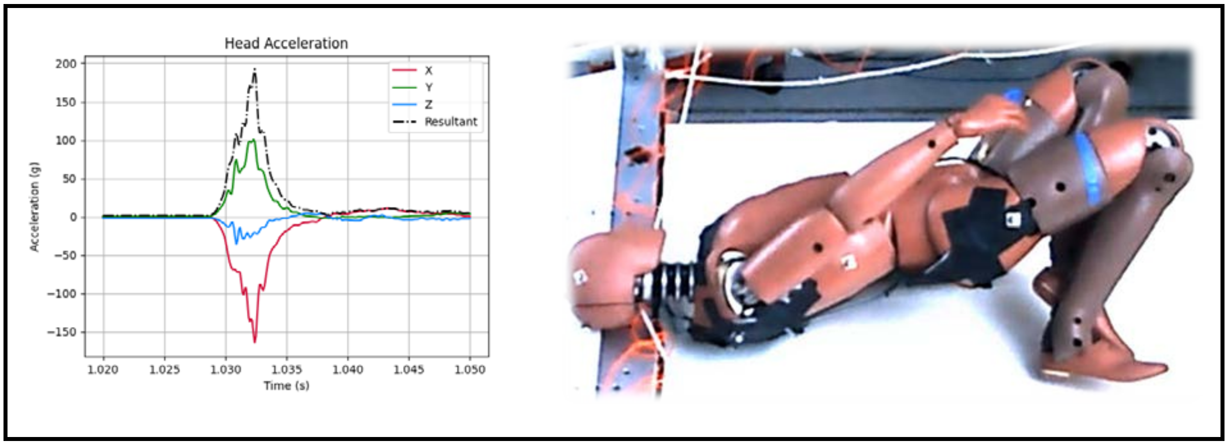

Figure 31. Head acceleration during secondary impact Test 23.

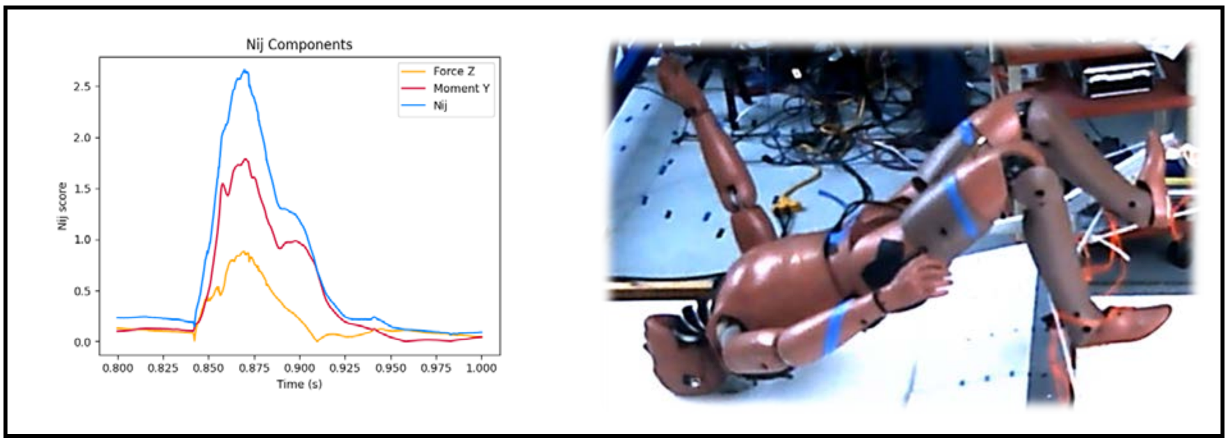

Figure 32. Force and moment contribution to Nij during secondary impact Test 24.

The injury criteria scores for the head and chest seen in the 35 mph sled tests tended to be on par with 5-star NCAP frontal impact tests (Figure 33), however substantial injury risk was observed in the neck and lower extremity. There was also a high brain injury risk predicted by BrIC but not by DAMAGE. For both the airbag and cored honeycomb sled test, all injury criteria remained below the NCAP thresholds except for tibia index (Table 16). The head and chest injury criteria from the cored honeycomb sled test were on par with 5-star NCAP tests as pictured in Figure 33.

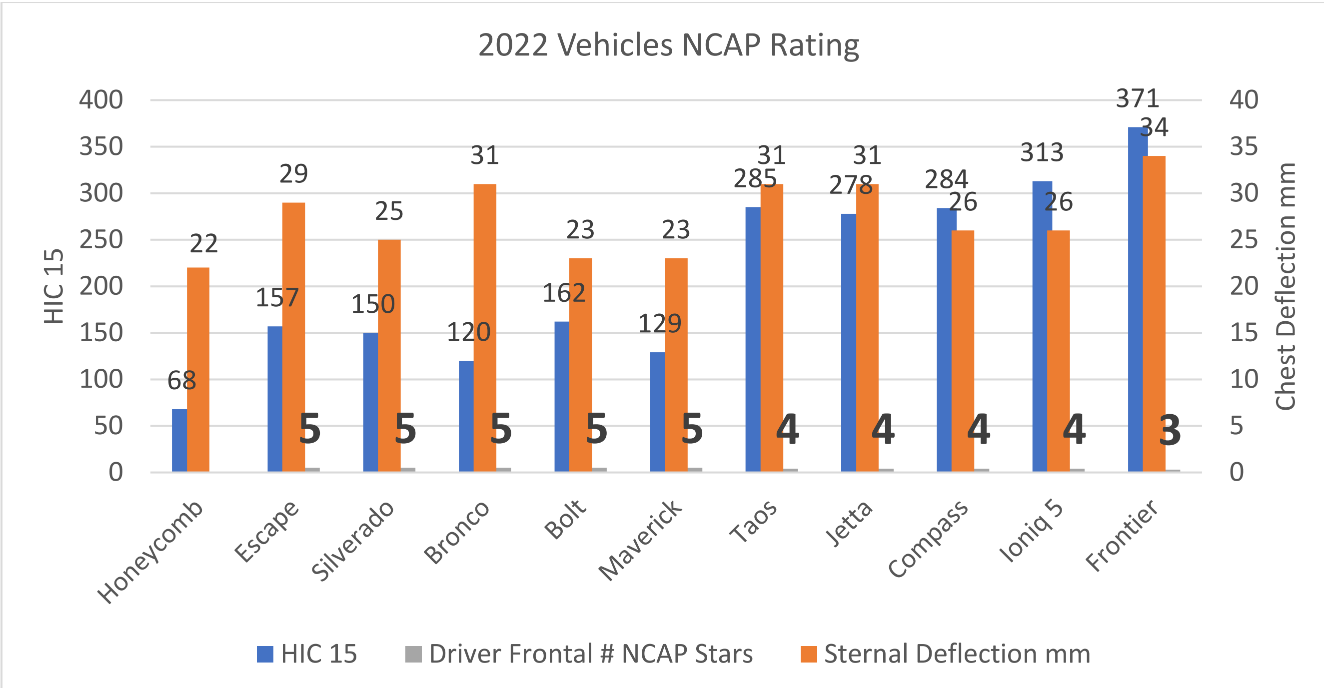

Figure 33. Injury criteria comparison between honeycomb countermeasure (Test 35) and NCAP rated cars.

Table 16. NCAP injury criteria comparison [6].

Measurement Description	Threshold	Test 24	Test 31	Test 32	Test 34	Test 35
Head Injury Criteria (HIC_{15})	700	84.6	179.2	72.7	168.8	68.0
Maximum Chest Compression (mm)	63	18.9	24.1	20.0	21.8	22.2
Nij	1	0.74	1.47	1.31	1.48	0.53
Neck Tension (N)	4170	579	154	658	543	333
Neck Compression (N)	4000	1243	3845	3633	3978	1184
Left Femur Force (kN)	10.0	4.27	5.06	4.32	6.22	4.25
Right Femur Force (kN)				3.63	8.49	
Left Tibia Index	0.91	1.49	1.61	2.03	1.95	1.49
Right Tibia Index				1.31	2.43	
Left Lower Tibia Axial Force (kN)	5.2	4.85	5.85	5.16	7.71	4.89
Right Lower Tibia Axial Force (kN)				4.28	10.20	

Nij is the NCAP accepted injury criterion for neck injury and is formulated using bending moment and axial force. Moment was the driving factor behind the high Nij scores seen in the airbag sled tests. Figure 34 shows the neck force and moment contribution to the Nij score for the 35 mph sled test with the airbag (Test 24). In this case, the contribution to Nij from moment was almost twice that from force. This can be partially attributed to the fact the head was unsupported during the primary impact (Figure 35), however these high scores were also present at lower speeds and even in cases where the head was supported. Test 29 (Figure 37), which was a 25 mph seated test produced a similar Nij score to Test 24 (Figure 36), despite a slower impact speed and minimal head acceleration. Test 34 (Figure 39) also yielded a high Nij score which was largely caused by compressive loading (Figure 38). As previously mentioned, this type of airbag is known to be non-injurious at these impact speeds, and thus these high Nij scores were likely an artifact of the inflexible Hybrid III neck, not dangerous loading by the countermeasure. Prior research reported that the Hybrid III overpredicts compressive neck forces. In similar tests with PMHS, the subjects sustained only minor or no injury while the dummy-derived Nij values predicted extensive neck injury. The authors attribute this discrepancy to a stiff dummy neck/surrogate spine [27]. Similarly, a NHTSA report found that the Hybrid III neck exhibits considerable inflexibility at its occipital condyle joint [14]. This may allow large moments to be transmitted to the neck by the head without much relative motion. Therefore, it was concluded that the dummy neck was too stiff to accurately represent human response and that our ability to estimate neck injury using the dummy response was compromised.

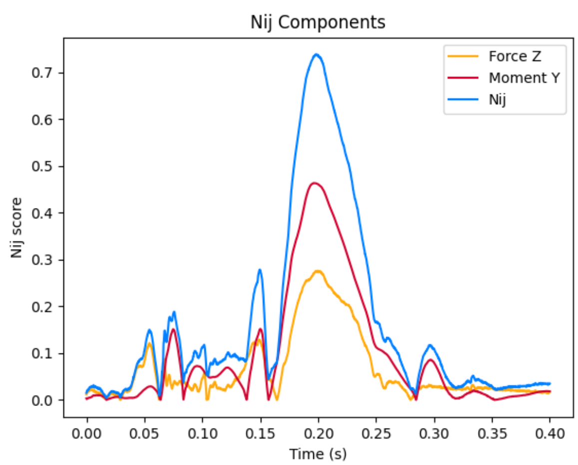

Figure 34. Test 24 Nij contribution from neck force and moment.

Figure 35. Test 24 head and neck unsupported by airbag.

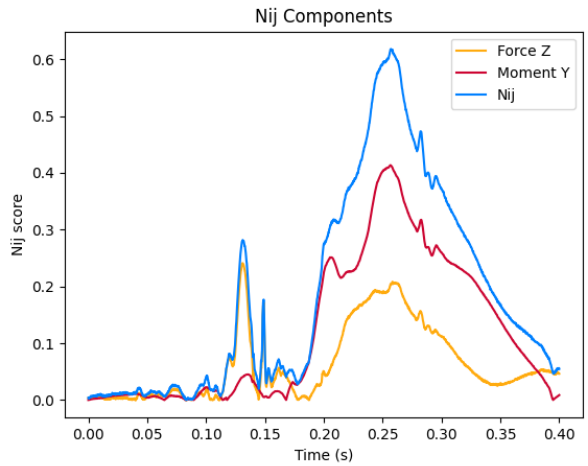

Figure 36. Test 29 Nij contribution from neck force and moment.

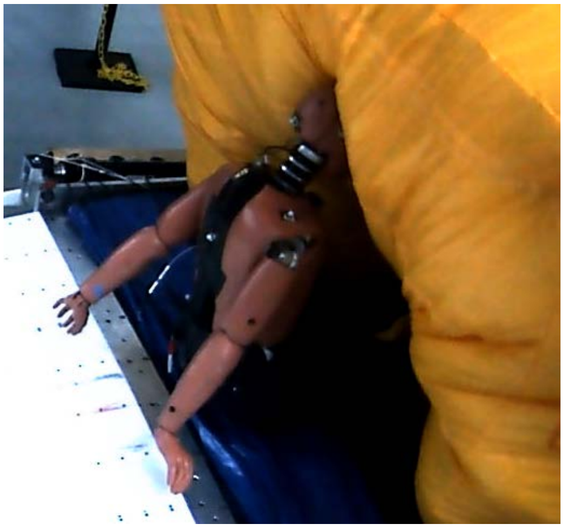

Figure 37. Test 29 head entering airbag.

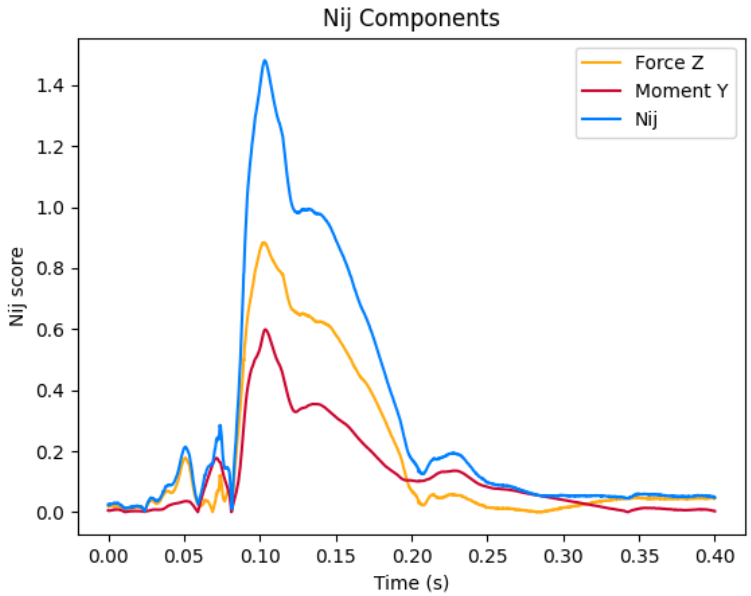

Figure 38. Test 34 large Nij contribution from axial loading.

Figure 39. Test 34 Hybrid III entering countermeasure headfirst.

Estimating brain injury risk was similarly difficult, as a non-biofidelic neck will change head kinematics. BrIC is a legacy injury criterion but has been shown not to be predictive of brain strain in longer duration impacts such as the ones seen in the sled tests (see section 2.3.2). For this reason, DAMAGE should be used to evaluate brain injury risk, while BrIC was included solely for reference. Out of the 35 mph tests, DAMAGE never predicted an AIS 4+ injury risk above 1%. Three injury criteria were used for lower extremity, including femur load, tibia load, and Revised Tibia Index (RTI). RTI is formulated using tibia load and was used in calculating the risk of shaft fracture. Substantial lower extremity injury risk was seen in most forward-facing tests, especially Test 34. The right femur force in this test reached 8.5 kN which corresponds with a 10% AIS 3+ injury risk (Figure 42). However, this loading is likely an artifact of the Hybrid III. As shown in Figure 40, this axial loading comes from contact with the scoop prior to impact with the countermeasure. This is not an injurious type of loading and should be ignored. Similarly, the high RTI scores (Figure 43) and high ankle loading were also caused by the scoop loading and impact with the dummy's posterior (Figure 41). The tendency for the knees to lock and transfer significant forces to the dummy legs despite a small amount of relative motion of the feet while sliding up the scoop is not biofidelic.

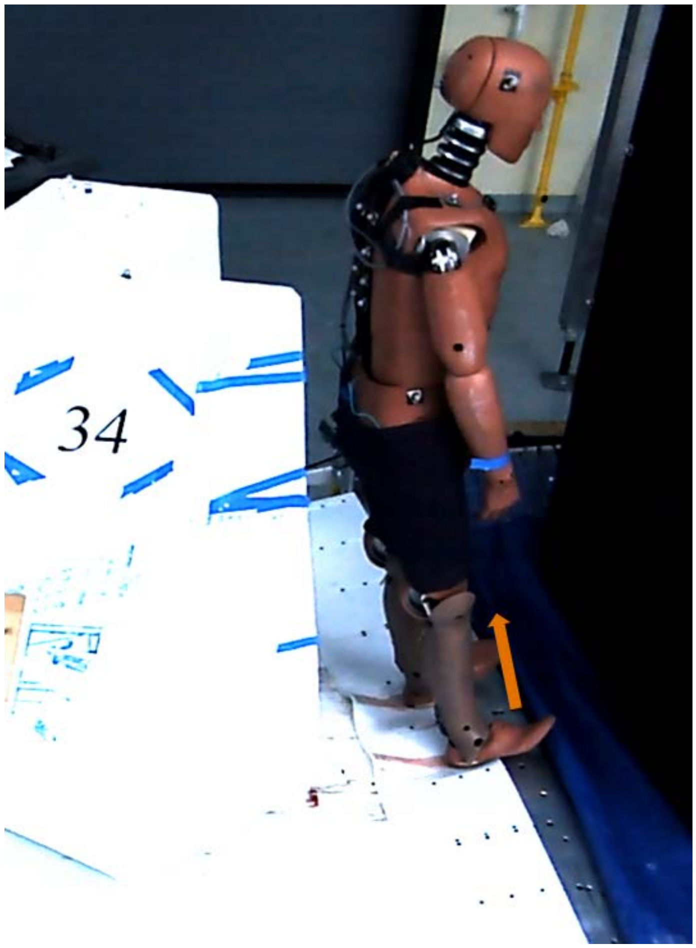

Figure 40. Test 34 scoop loading the femur.

Figure 41. Test 34 Hybrid III heels impacting posterior.

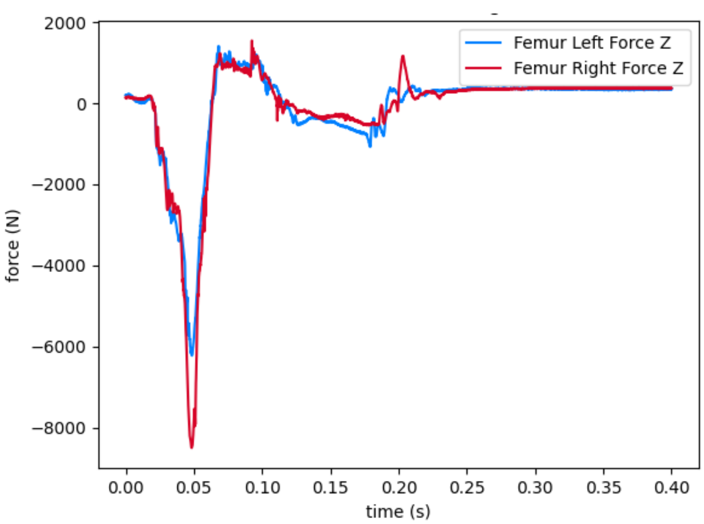

Figure 42. Test 34 femur force spike corresponding with the scoop loading.

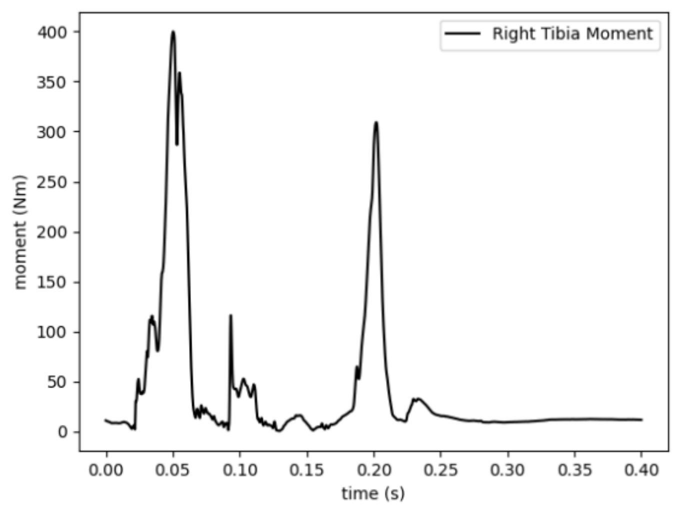

Figure 43. Test 34 tibia moment spike corresponding with the scoop loading and secondary spike from impact with posterior (see Figure 41).

Test 35 involved the cored honeycomb countermeasure and featured a scoop and capture mechanism. AIS 3+ injury risk for this test was below 3% for all body regions except neck. As discussed above, the high neck injury risk was likely to be due to limitations of the Hybrid III and not a cause for concern. This theory was explored using FE simulations in section 6.2. The catcher mechanism was successful at preventing the dummy from rebounding onto the sled (Figure 44).

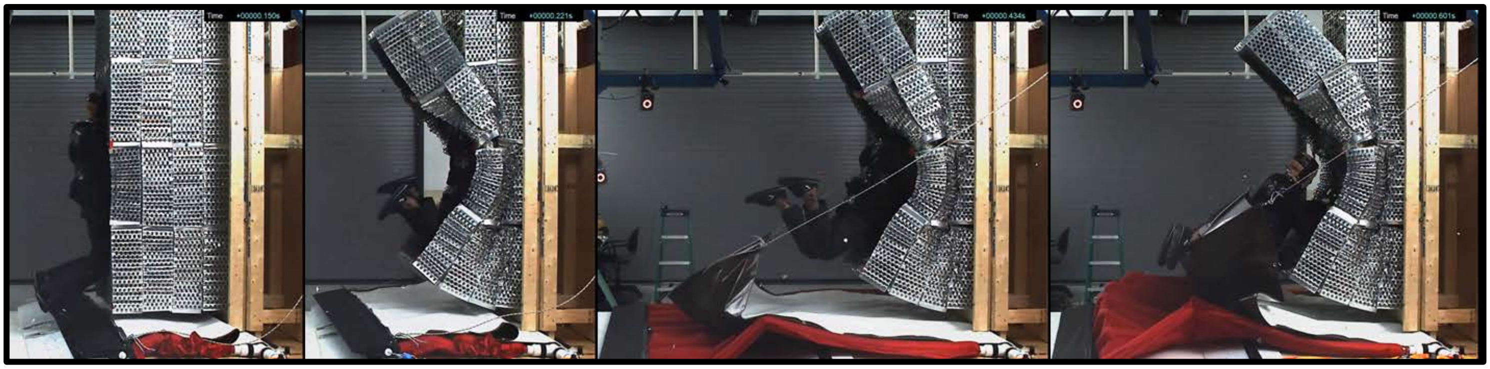

Figure 44. Test 35, cored honeycomb sled test sequence.

The injury risk from the honeycomb test was compared to that of the airbag sled test to ensure that honeycomb was similarly effective at preventing injury. Based on the experimental results it was determined that the honeycomb was as safe as the airbag and even produced lower injury in some body regions as summarized in Table 17.

Table 17. Injury summary comparing 35 mph airbag sled test and cored honeycomb test.

Injury	**Criteria**		**Risk**	
	Test 24	**Test 35**	**Test 24**	**Test 35**
AIS 3+ Skull	HIC15: 84.6	HIC15: 68.0	0.0%	0.0%
AIS 4+ Brain	DAMAGE: 0.21	DAMAGE: 0.29	0.2%	0.8%
AIS 3+ Neck	Nij: 0.74	Nij: 0.53	14.5%	10.2%
AIS 3+ Chest	Cmax: 18.9 mm	Cmax: 22.2 mm	0.0%	0.1%
AIS 3+ Femur	Fz: 4.27 kN	Fz: 4.25 kN	2.7%	2.7%

5.3. Conclusion

The purpose of this test series was to gauge the effectiveness of potential countermeasure materials in terms of their ability to minimize injury and rebound. Due to limitations of the Hybrid III dummy, several body regions including neck and lower extremity exhibit non-biofidelic behavior resulting in unrealistically high forces and moments under certain loading conditions. Injury risk for these body regions will be explored through finite element simulation. Excluding neck and lower extremity, both the airbag and crushable aluminum countermeasures produced minimal injury risk at 35 mph. The head and chest injury criteria scores with the cored honeycomb were on par with five-star NCAP tests. Stunt airbags like the one used in this test series are routinely and effectively used to prevent injury from falls at comparable speeds to the sled tests. For this reason, the airbag countermeasure serves as a benchmark to compare the other countermeasures. It was demonstrated that the final honeycomb countermeasure was similarly effective at preventing injury as the airbag. Based on this work, it was concluded that honeycomb is an effective material for human impact mitigation and injury prevention.

Chapter 6. Countermeasure Simulations

Following the first round of sled testing, a suite of simulations was created to answer important questions that could not be answered with sled testing alone. While physical tests are generally preferable to simulations, there was reason to question whether the Hybrid III was biofidelic enough to accurately assess neck and lower extremity injury. The sled tests were also limited in the number of trials that could be feasibly conducted due to time and budget limitations. For these reasons, it was necessary to use FEA to supplement the injury analysis done with the sled tests.

6.1. Environment Validation

The first objective was to create a simulation environment to replicate the airbag sled tests. This included the FE stunt airbag model that had been previously validated using drop test data and a FE Hybrid III model. The goal was to verify that the simulation was an accurate representation of the sled environment by comparing kinematic data. Surprisingly, the 35 mph simulation overpredicted dummy acceleration when compared to sled test 24 (Figure 47). While the optimized airbag model was predictive at impact speeds comparable to the drop tests, the model did not extrapolate well to higher speed impacts. A likely reason for this discrepancy was the difference between the elastic restraint bands used to fasten the airbag cover to the base chambers, and the beam elements used to model these bands. As seen in Figure 45, the restraint bands on the i2k airbag were loose prior to impact while the beam elements in the simulations were taught (Figure 46). This extra tension in the airbag cover could have caused the load to be distributed across more of the airbag's fingers, increasing the force on the Hybrid III. This effect was most noticeable at higher energy impacts, which may explain why the discrepancy only appeared in the 35 mph case.

Figure 45. Hybrid III entering i2k airbag in Test 24.

Figure 46. Test 24 simulation using FE airbag.

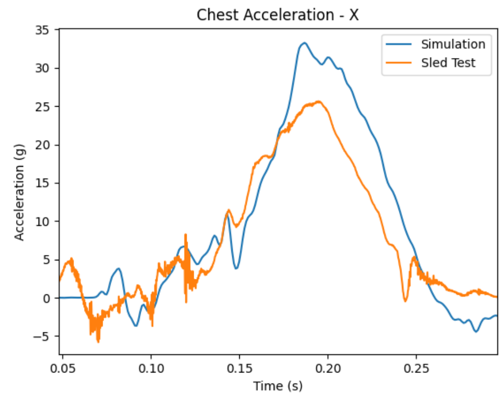

Figure 47. Airbag chest acceleration comparison for Test 24.

This exercise was repeated for Test 34 (Figure 48). The honeycomb was covered with an unrestrained polyethylene tarp, which was modelled using the same material characteristics as the cover for the i2k airbag (Figure 49). The honeycomb material model was created using stress-strain data obtained from compression testing as described in section 3.6 above. Unlike the airbag simulation, the honeycomb simulation matched the sled test well both in terms of qualitative kinematics and peak acceleration (Figure 50).

Figure 48. Hybrid III impact with countermeasure in Test 34.

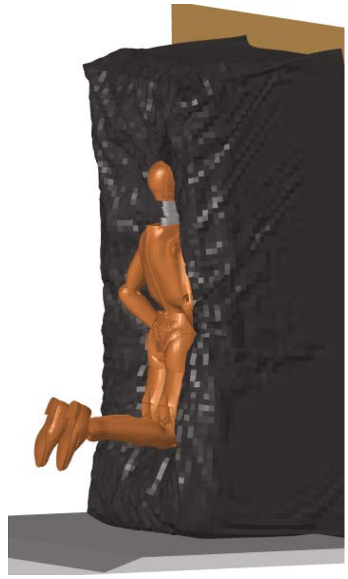

Figure 49. Test 34 simulation using FE honeycomb material model.

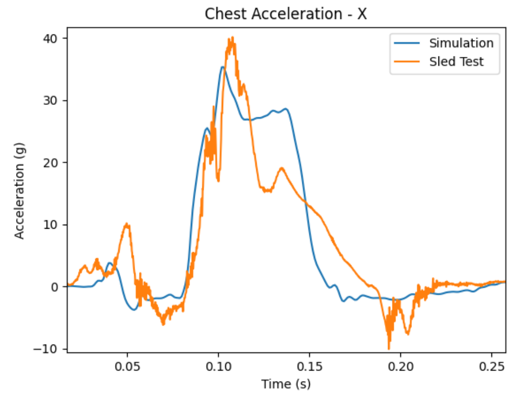

Figure 50. Honeycomb chest acceleration comparison for Test 34.

6.2. Injury Analysis and Optimization

Using the validated simulation environment, Test 34 was replicated using THUMS instead of the Hybrid III ATD model (Figure 51). The goal of this simulation was to assess whether the high neck and lower extremity injury were in fact due to limitations of the Hybrid III or if THUMS would also predict high injury in these body regions. As was expected, the risk of AIS 3+ femur injury was around 1% and the risk of AIS 3+ neck injury was well below 1% (Table 18). Other body regions had similarly low AIS 3+ injury risk.

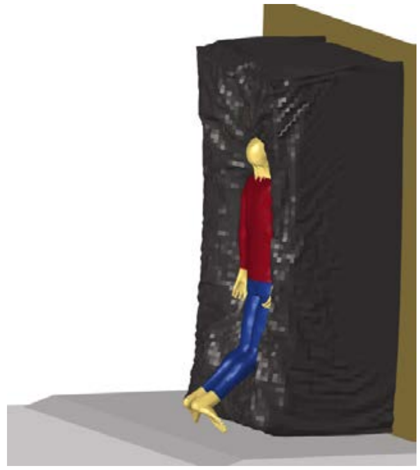

Figure 51. Test 34 replicated with THUMS.

Table 18. Injury risk from 35 mph honeycomb simulation with THUMS.

region	1+	2+	3+	4+	5+	6
thorax	N/A	N/A	0.0%	N/A	N/A	N/A
arm	N/A	0.1%	N/A	N/A	N/A	N/A
wrist	N/A	0.0%	N/A	N/A	N/A	N/A
pelvis	N/A	N/A	0.6%	N/A	N/A	N/A
femur	N/A	0.7%	1.2%	N/A	N/A	N/A
tibia	N/A	1.6%	N/A	N/A	N/A	N/A
ankle	N/A	0.9%	N/A	N/A	N/A	N/A
face	N/A	43.3%	N/A	N/A	N/A	N/A
neck	N/A	0.4%	0.4%	N/A	N/A	N/A
brain	17.0%	10.6%	N/A	0.4%	N/A	N/A
head	15.1%	5.0%	1.8%	0.4%	0.0%	0.0%

As discussed in the Appendix A. Testing Supplementary, the honeycomb used in test 34 was fabricated at the lab. Honeycomb available from vendors was too stiff for human impact mitigation, but the stiffness could be reduced through coring (section 3.4). It was important to understand the range of honeycomb stiffness that would prevent serious injury during impact to serve as a target for the coring process. The simulation setup above was used to create a suite of simulations to explore how stiffness and orientation affected the risk of serious (AIS 3+) injury in

35 mph impacts. The stress-strain curve from the fabricated honeycomb was scaled to have a plateau stress ranging from just under 0.3 psi to over 2.5 psi. Forward facing and side facing orientations for THUMS were used. Low risk of serious injury was detected in the forward-facing cases, with the most severe still being less than 5%. In the side facing cases, thoracic injury was the main driver of serious injury risk. In these cases, injury risk increased sharply below 0.5 psi and began increasing gradually above 1.5 psi (Figure 52). Anywhere in this range was acceptable, but it was preferable to err towards the higher end, as it will prevent the countermeasure from bottoming out in higher speed impacts. This information aided in the honeycomb fabrication process and helped develop the honeycomb that was used in the second round of sled testing (Figure 53).

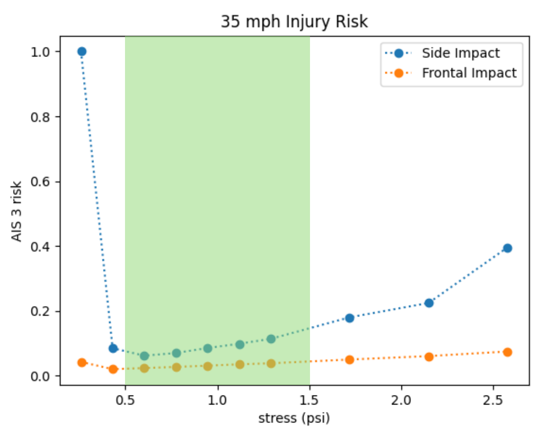

Figure 52. Risk of sustaining at least one AIS 3+ injury in forward and side impacts with the honeycomb countermeasure, with the x-axis describing the plateau of the stress-strain curve.

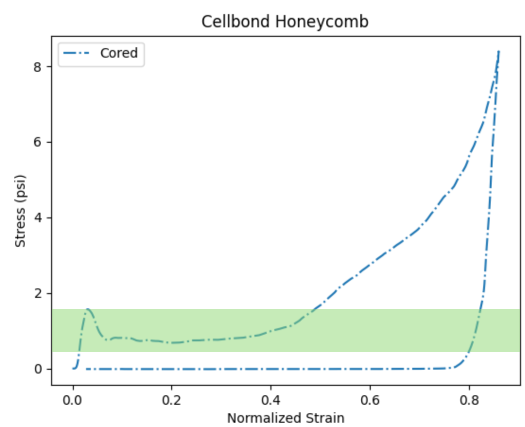

Figure 53. Cored honeycomb stress-strain curve, green region corresponds with the optimal plateau stress as determined by simulation.

Following the fabrication and characterization of the cored honeycomb, a FE material model was formulated using its stress-strain curve (Figure 53). Side impact simulations were conducted at speeds ranging from 15 to 45 mph, using the same environment shown in Figure 50, with the updated material model implemented. Based on these simulations, injury distributions were generated for each impact speed using the same process described in section 3.2. These distributions were weighted by frequency of occurrence to generate an overall injury distribution (Figure 54). Injury risk increases exponentially after 35 mph, with thoracic injury being the main contributor. This is because the material had been optimized to minimize injury at this speed, and higher speeds cause the honeycomb to bottom out. Despite the countermeasure being only 30 inches thick, the injury distribution was far less severe than the one predicted by the original train simulations. Based on the method described in section 2.2, the countermeasure was estimated to be 98.7% effective at preventing fatalities.

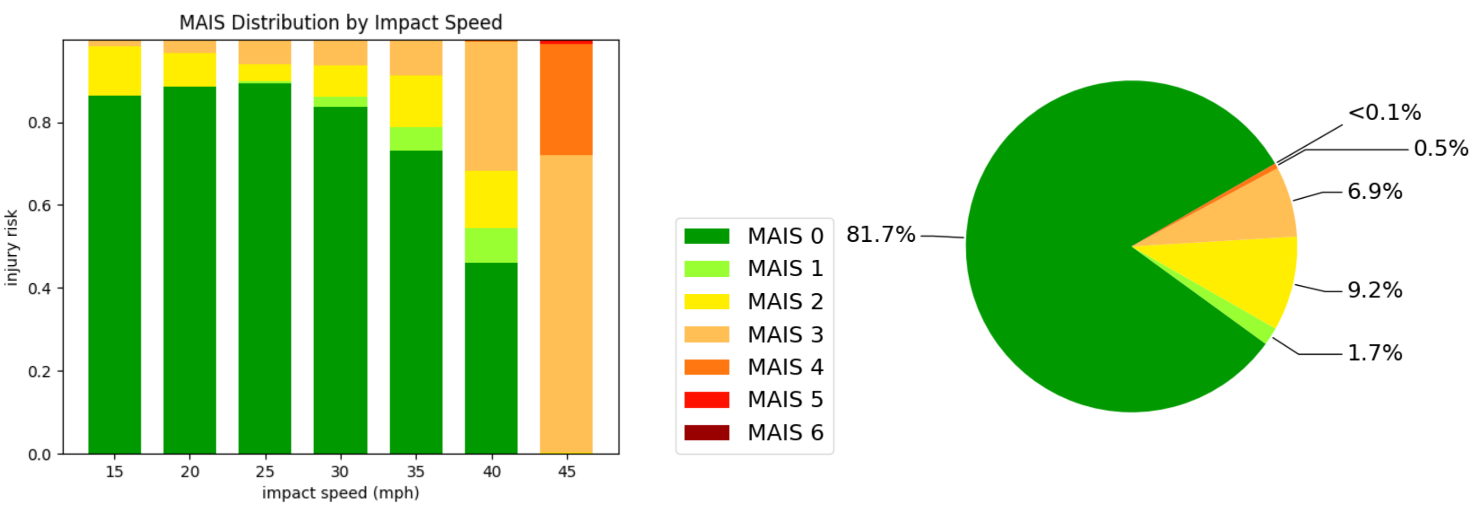

Figure 54. Honeycomb countermeasure injury distribution from THUMS FE simulations.

Chapter 7. Benefit-Cost Analysis

The potential for an impact-mitigating countermeasure to minimize fatalities in the NYC subway system was demonstrated in Chapter 5 and Chapter 6. However, it was also important to show that the implementation of such a device would be cost effective. Based on guidance from the Department of Transportation (DOT), a benefit-cost analysis was conducted to estimate the plausible range for the project's Net Present Value (NPV) [28]. This was done based on rough cost estimates and DOT guidelines for the Value of a Statistical Life (VSL) [29]. For a more in-depth discussion of the calculations and assumptions made, see Appendix B. Cost Benefit Supplementary.

7.1. Results

To demonstrate that the impact-mitigating countermeasure is a viable solution to the problem of train-pedestrian collisions, it is important to show that the NPV remains positive within the range of possible parameters. Injury risk sensitivity to loading varies by human body model, and the estimate for device effectiveness was affected by these differences. The highest estimate for device effectiveness came from the THUMS simulations from section 6.2, which predicted a 98.7% reduction in fatalities. The lower end estimate for device effectiveness came from the MADYMO Pedestrian simulations in section 3.2 (84.3% effective). There are several parameters that were not well constrained, including the buildout time and device cost. The best- and worst-case estimates for the project's NPV are shown in Table 19. In the worst-case scenario, the NPV over a 50 year period was expected to be over one billion USD.

Table 19. Best- and worst-case estimates for NPV using DOT recommended VSL.

	Best Case	Worst Case
Installation Cost (million USD)	$235	$7,001
Maintenance Cost (million USD)	$20.3	$119.2
Completion (years)	10	35
Device Effectiveness %	98.7%	84.3%
NPV (million USD)	$16,091.8	$1,038.2

7.2. Discussion

While saving lives is the end goal of any public safety project, convincing policymakers to implement the solution may ultimately be contingent on whether it is cost effective. For this reason, it is essential to demonstrate that a project proposal is expected to have a positive NPV. It is worth noting that the benefits considered in this analysis solely pertained to lives saved and injuries prevented. A more comprehensive benefit-cost analysis may seek to include reduced legal costs from lawsuits, operational expenditures due to incidents, and commuter wage loss from train delays as part of the project benefits. Using the DOT recommended VSL, the worst-case analysis determined that the countermeasure implementation would have a positive NPV for the most conservative assumptions within the range of uncertainty, meaning that the countermeasure implementation would be economically beneficial. This result justifies future investment on public safety projects for the NYC subway.

Conclusion

Based on NYC subway incident statistics, a countermeasure concept was devised that would minimize injury risk to pedestrians during impact. The design involved an impact-mitigating device along with a false floor and scoop to prevent rollover. Energy attenuating materials that exhibited desirable physical properties and met NYCT fire safety standards were identified and tested in a laboratory setting. It was ultimately decided that aluminum honeycomb was the best option based on cost, insensitivity to environmental factors, and ability to minimize rebound after impact. Countermeasure effectiveness was assessed through a combination of simulations and physical testing. There were some assumptions that had to be made for this analysis due to limitations in the human body models as well as uncertainty with regards to operational concerns. The kinematics of the Hybrid III dummy as well as the HBMs could not be trusted after the primary impact. This made it difficult to analyze secondary impact with the track bed and rollover. For the injury analysis it was assumed that the scoop and false floor would be effective at preventing rollover. There was also uncertainty with regards to which parts of the train could be covered with an impact-mitigating device due to regulations and safety concerns. If NYCT policy prevents the door, anti-climber, and coupler from being covered, this could drastically reduce the effectiveness of a potential countermeasure. Sled tests were conducted to determine the effectiveness of a honeycomb countermeasure at reducing injury in 35 mph impacts. The catcher mechanism proved successful at preventing the dummy from rebounding after the primary impact. The cored honeycomb countermeasure produced very low injury risk for the head and thorax, but moderate injury risk for neck and lower extremity. The injury criteria scores from the cored honeycomb sled test were all below NCAP specified thresholds except for RTI. Previous literature on the Hybrid III suggested that the high neck injury risk was an artifact of the poor biofidelity of the dummy. A set of simulations recreated the sled tests with an FE human body model instead of a dummy. In these cases, the risk of lower extremity injury was near zero, suggesting that the Hybrid III might also be overpredicting femur force in certain loading conditions. Using finite element simulation, it was estimated that a theoretical countermeasure could reduce fatalities in train-pedestrian collisions by at least 84%. Currently, one in three train-pedestrian collisions result in fatality. After the implementation of a countermeasure, it is expected that the fatality rate will fall to under 5%. A benefit-cost analysis was used to assess the financial viability of the impact-mitigating countermeasure as well as other potential safety solutions. The inability to accurately estimate parameters such as project cost and installation time resulted in significant uncertainty in the overall costs and benefits. Despite this, the project NPV remained above one billion USD in the worst-case analysis when using the VSL suggested by DOT. The results presented in this thesis demonstrate the potential for an impact-mitigating device to drastically reduce fatalities within the NYC subway. Future work on this topic should explore the potential of using active systems such as deployable airbags that would not cause the same operational concerns as a passive impact-mitigating device.

References

[1] D. Hall, J. Linogao, L. Zentz, G. Shaw, T. Lamb, and C. Simms, “Detailed Analysis of New York City Subway Pedestrian Incidents From 2019,” *Transp. Res. Rec. J. Transp. Res. Board*, vol. 2677, no. 11, pp. 642–650, Nov. 2023, doi: 10.1177/03611981231166692.

[2] “System-Wide Platform Screen Door Feasibility Study,” New York City Transit, Feb. 2020. Accessed: Aug. 01, 2024. [Online]. Available: https://new.mta.info/document/73241

[3] P. T. Lin and J. R. Gill, “Subway Train-Related Fatalities in New York City: Accident versus Suicide*,” *J. Forensic Sci.*, vol. 54, no. 6, pp. 1414–1418, Nov. 2009, doi: 10.1111/j.1556-4029.2009.01165.x.

[4] “TIGER Benefit-Cost Analysis (BCA) Resource Guide.” U.S. Department of Transportation, Apr. 18, 2014. [Online]. Available: https://www.transportation.gov/sites/dot.gov/files/docs/TIGER%20BCA%20Resource%20Guide%202014.pdf

[5] L. Hershman, “THE U.S. NEW CAR ASSESSMENT PROGRAM (NCAP): PAST, PRESENT AND FUTURE,” U.S. NCAP, 390, 2001. [Online]. Available: https://www-nrd.nhtsa.dot.gov/pdf/esv/esv17/Proceed/00245.pdf

[6] James Saunders, Allison Louden, and Aloke Prasad, “OFFSET TEST DESIGN AND PRELIMINARY RESULTS,” NHTSA, 2007. [Online]. Available: https://www-nrd.nhtsa.dot.gov/pdf/ESV/Proceedings/20/07-0240-W.pdf

[7] “Abbreviated Injury Scale (AIS),” Association for the Advancement of Automotive Medicine. Accessed: Aug. 01, 2024. [Online]. Available: https://www.aaam.org/abbreviated-injury-scale-ais-position-statement/

[8] A. A. Weaver, R. T. Barnard, P. D. Kilgo, R. S. Martin, and J. D. Stitzel, “Mortality-based Quantification of Injury Severity for Frequently Occurring Motor Vehicle Crash Injuries,” *Ann. Adv. Automot. Med. Assoc. Adv. Automot. Med. Annu. Sci. Conf.*, vol. 57, pp. 235–246, 2013.

[9] M. Craig, D. Parent, E. Lee, R. Rudd, E. G. Takhounts, and V. Hasija, “Injury Criteria for the THOR 50th Male ATD,” NHTSA, Sep. 2020. [Online]. Available: https://www.regulations.gov/document/NHTSA-2020-0032-0004

[10] E. G. Takhounts, M. J. Craig, K. Moorhouse, J. McFadden, and V. Hasija, “Development of Brain Injury Criteria (BrIC),” presented at the 57th Stapp Car Crash Conference, Nov. 2013, pp. 2013-22–0010. doi: 10.4271/2013-22-0010.

[11] F. Hernandez and D. B. Camarillo, “Voluntary Head Rotational Velocity and Implications for Brain Injury Risk Metrics,” *J. Neurotrauma*, vol. 36, no. 7, pp. 1125–1135, Apr. 2019, doi: 10.1089/neu.2016.4758.

[12] L. F. Gabler, J. R. Crandall, and M. B. Panzer, “Development of a Second-Order System for Rapid Estimation of Maximum Brain Strain,” *Ann. Biomed. Eng.*, vol. 47, no. 9, pp. 1971–1981, Sep. 2019, doi: 10.1007/s10439-018-02179-9.

[13] T. Wu *et al.*, “Integrating Human and Nonhuman Primate Data to Estimate Human Tolerances for Traumatic Brain Injury,” *J. Biomech. Eng.*, vol. 144, no. 7, p. 071003, Jul. 2022, doi: 10.1115/1.4053209.

[14] Rolf Eppinger, Emily Sun, and Shashi Kuppa, “Development of Improved Injury Criteria for the Assessment of Advanced Automotive Restraint Systems - II,” NHTSA, Mar. 2000.

[15] R. Kent, J. Patrie, and N. Benson, “The Hybrid III dummy as a discriminator of injurious and non-injurious restraint loading,” *Annu. Proc. Assoc. Adv. Automot. Med.*, vol. 47, pp. 51–75, 2003.

[16] R. Kent and J. Patrie, “Chest deflection tolerance to blunt anterior loading is sensitive to age but not load distribution,” *Forensic Sci. Int.*, vol. 149, no. 2–3, pp. 121–128, May 2005, doi: 10.1016/j.forsciint.2004.04.086.

[17] J. Forman, S. Kulkarni, D. Perez-Rapela, S. Mukherjee, M. Panzer, and J. Hallman, “A method for thoracic injury risk function development for human body models,” in *IRCOBI Conference. Porto, Portugal*, 2022, pp. 12–15.

[18] S. Kuppa, J. Wang, M. Haffner, and R. Eppinger, “Lower extremity injuries and associated injury criteria,” SAE Technical Paper, 2001.

[19] A. Petitjean, X. Trosseille, P. Petit, A. Irwin, J. Hassan, and N. Praxl, “Injury Risk Curves for the WorldSID 50th Male Dummy,” presented at the 53rd Stapp Car Crash Conference, Nov. 2009, pp. 2009-22–0016. doi: 10.4271/2009-22-0016.

[20] J. Cormier *et al.*, “The tolerance of the nasal bone to blunt impact,” *Ann. Adv. Automot. Med. Assoc. Adv. Automot. Med. Annu. Sci. Conf.*, vol. 54, pp. 3–14, 2010.

[21] J. Forman, B. Perry, A. Alai, A. Freilich, R. Salzar, and T. Walilko, “Injury tolerance of the wrist and distal forearm to impact loading onto outstretched hands,” *J. Trauma Acute Care Surg.*, vol. 77, no. 3, pp. S176–S183, Sep. 2014, doi: 10.1097/TA.0000000000000329.

[22] V. Bollapragada, “The Influence of Disabling Injuries on the Design of the Vehicle Front End for Pedestrian Safety,” University of Virginia, 2019. doi: 10.18130/V3-SR6H-SP61.

[23] “LS-DYNA Keyword User’s Manual.” Livermore Software Technology, Jul. 17, 2020.

[24] K. E. Jackson *et al.*, “Experimental and Analytical Evaluation of a Composite Honeycomb Deployable Energy Absorber,” 2011.

[25] E. Power, J. Bauer, and W. Hayes, “Impact Forces and Injury Potential from Landing on Large Inflatable Airbags,” *J. N Forensic Biomech.*, vol. 10, no. 1, 2019.

[26] A. Hirth, A. Haufe, and L. Olovsson, “Airbag Simulation with LS-DYNA: Past-Present-Future,” May 2007.

[27] J. Kerrigan *et al.*, “Axial Compression Injury Tolerance of the Cervical Spine- Initial Results,” *Traffic Inj. Prev.*, 2014.

[28] “Treatment of the Value of Preventing Fatalities and Injuries in Preparing Economic Analyses,” Kentucky Transportation Center, Mar. 2021. [Online]. Available: https://uknowledge.uky.edu/ktc_researchreports/1547

[29] “Departmental Guidance on Valuation of a Statistical Life in Economic Analysis,” U.S. Department of Transportation. Accessed: Apr. 14, 2024. [Online]. Available: https://www.transportation.gov/office-policy/transportation-policy/revised-departmental-guidance-on-valuation-of-a-statistical-life-in-economic-analysis

[30] “INSTRUMENTATION FOR IMPACT TEST—PART 1—ELECTRONIC INSTRUMENTATION,” SAE International. Accessed: Apr. 14, 2025. [Online]. Available: https://law.resource.org/pub/us/cfr/ibr/005/sae.j211-1.1995.html

[31] “DIAdem Help,” National Instruments. Accessed: Apr. 14, 2025. [Online]. Available: https://www.ni.com/docs/en-US/bundle/diadem/page/crash/misc_cfc.html

[32] A. Hayes, “Benefit-cost ratio (BCR): Definition, formula, and example,” Investopedia. Accessed: Aug. 25, 2024. [Online]. Available: https://www.investopedia.com/terms/b/bcr.asp

[33] “Station accessibility projects.” Accessed: Aug. 26, 2024. [Online]. Available: https://www.mta.info/project/station-accessibility-upgrades

[34] “Use of Discounting, Present Value, Constant and Future Dollars in Benefit-Cost Analysis,” U.S. Department of Transportation. Accessed: Jul. 13, 2022. [Online]. Available: https://ops.fhwa.dot.gov/publications/fhwahop14032/ch3.htm
[35] “Circular No. A-4.” Office of Management and Budget, Nov. 09, 2023. Accessed: Jun. 18, 2024. [Online]. Available: https://www.whitehouse.gov/wp-content/uploads/2023/11/CircularA-4.pdf

Appendix A. Testing Supplementary

Countermeasures

Figure 58 and Figure 59 describe the fabrication of the aluminum tray countermeasures. Figure 61 and Figure 62 describe the fabrication process of the honeycomb countermeasure and Figure 60 details the honeycomb geometry.

Airbag tests 23-30   Crushable aluminum tests 31-34

Figure 55. Pre-test configuration of the scoop and countermeasure.

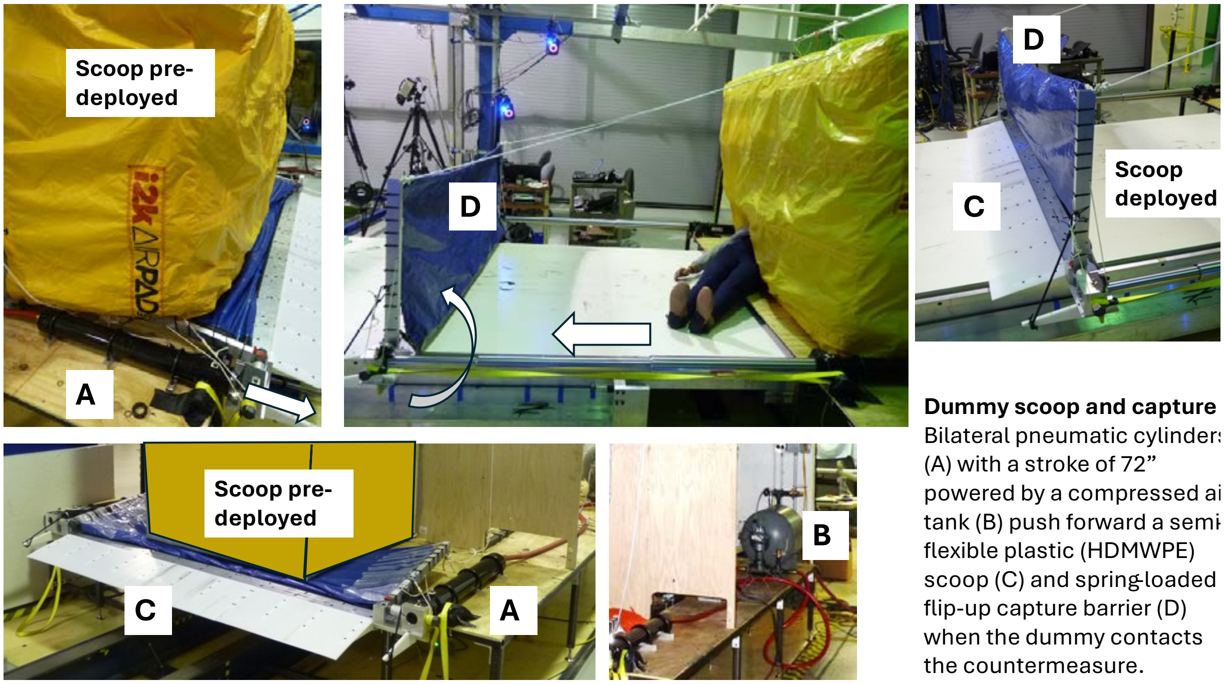

Figure 56. Dummy scoop and capture mechanisms.

Tests 23-29

A stunt airbag* was rotated 90 deg and screwed to the stage wall. With a 3” diameter vent, the pre-test inflation pressure is 0.21 psi.

*AirPad (Fall Protection) Custom Size 8’x5’x4’ h^. Commercial Fall Protection AirPad w/Zero Shock technolody)Patented Crumple Tubes under top sheet.

^Actual height ~ 4.5’ inflated.

Company: Inflatable 2000
Azusa, CA 91702

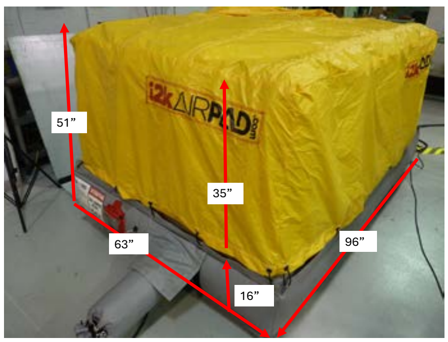

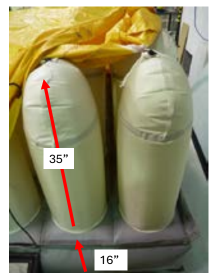

The airbag construction includes a ~16” thick base chamber and ~35” tall air pillars (Figure ??).

Figure 57. i2k Stunt Airbag dimensions.

Tests 31, 32

Half Size Foil Steam Table Pan
Extra Deep 4 3/16" Depth
https://www.webstaurantstore.com/1-2-size-foil-4-extra-deep-steam-table-pan-case/612634260.html

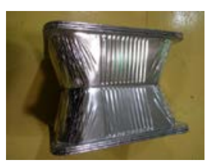

Test 31
Three plans glued together to increase crush stiffness.

Test 32
Single plans taped together forming an air pocket.

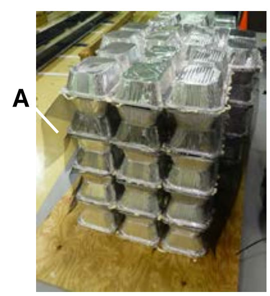

Test 31
Assembly prior to enclosing in foam panels. Both test 31 and 32 assemblies used fiberglass screen (A) to stabilize the structure and to increase crush resistance via recruitment of elements not directly loaded by the dummy. A combination of polyurethane adhesive and polyurethane foam insulation was used to hold the pans together.

Figure 58. Aluminum pans used for the countermeasure in Test 31.

Tests 31, 32

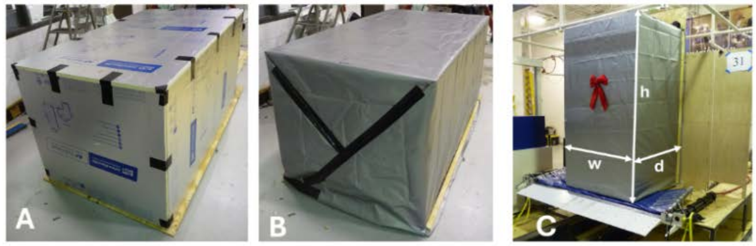

Both pan assemblies were enclosed in 1”thick polystyrene insulation panels. Test 31 used aluminum-foil-faced panels (A). Test 32 used similar panels without the foil (not shown).

In both tests, the foam panel enclosures were covered with a 0.020” thick polyethylene tarp (B).

After fabrication, the assemblies were screwed to the stage wall (C).

	Width	Depth	Height
31	42”	41”	78”
32	42”	32”	78”

Figure 59. Aluminum pan countermeasure.

Test 34

We fabricated custom large-cell (3”) aluminum honeycomb after being unsuccessful in finding commercially available products soft enough / comparable to the response of the airbag.
We used soft 0.003” thick 1000 series aluminum foil for its ease of forming. We fabricated a press to speed fabrication. The 53 layers of preforms were glued with polyurethane adhesive.

Material source:
https://www.mcmaster.com/products/aluminum-sheets/easy-to-form-pure-1000-series-aluminum-sheets-and-bars/?s=aluminum-sheets

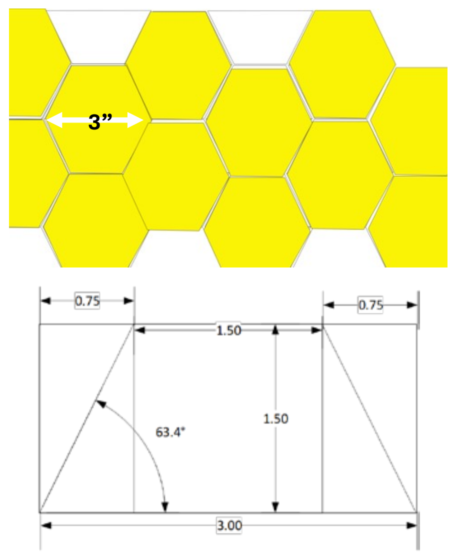

Half-cell geometry (inches)

Figure 60. Custom honeycomb dimensions.

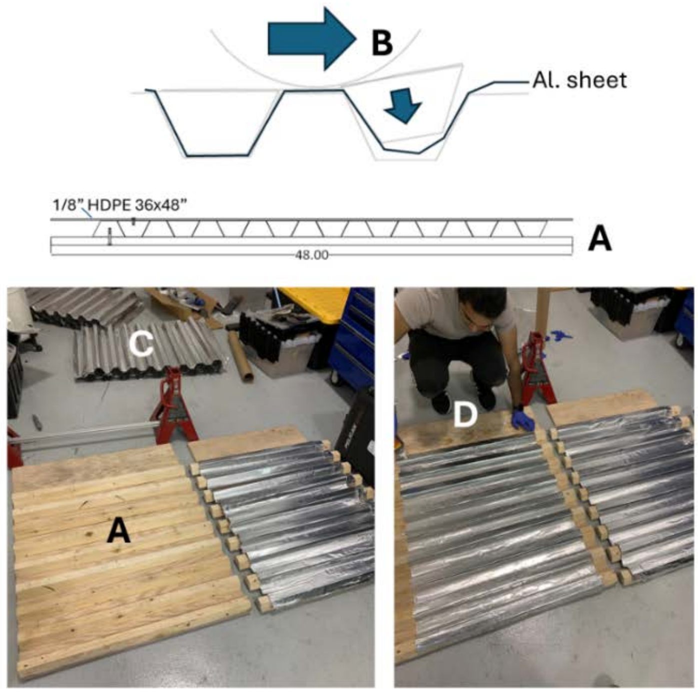

Honeycomb fabrication

A – wooden press: The press includes a flexible upper member (1/8" HDPE) that allows progressive forming (B).
C- preforms
D – preparing to laminate preforms

Figure 61. Custom honeycomb fabrication.

Test 34

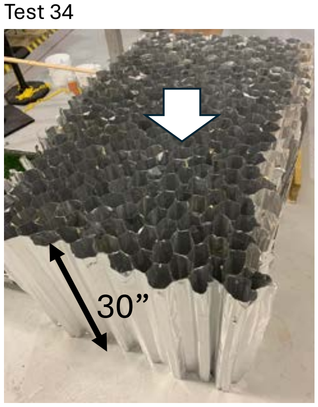

Honeycomb after lamination of preforms. Arrow indicates direction of dummy loading along the long axis of the cells.

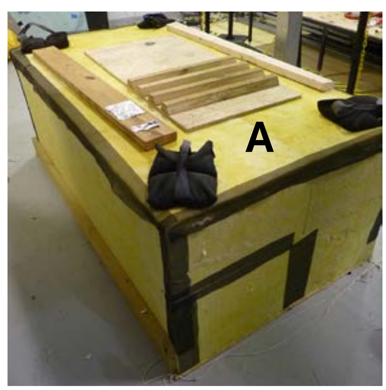

Honeycomb countermeasure encased in compressed fiberglass acoustic panels. Photo shows weights on the top panel to ensure polyurethane foam insulation bonding of the panel with the honeycomb. This added support was necessary as the very soft honeycomb structure sagged due to its own mass. Panel A is 2" thick; the other four panels are 1" thick.

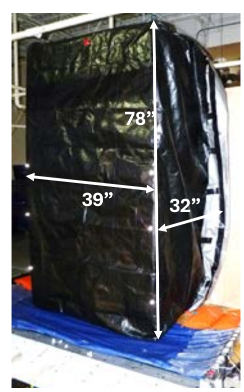

Assembled honeycomb countermeasure with tarp.

Figure 62. Custom honeycomb countermeasure.

Figure 63. Cored honeycomb countermeasure.

Figure 64. Test 35 post-test deformation.

Test Procedures

Before each test, the sled rails and the hydraulic decelerator were lubricated. A trigger check was performed to ensure the scoop and data acquisition systems were armed and functioning. The Hybrid III was positioned according to the specified test parameters (Figure 65) and the dummy's onboard DAS was armed and disconnected. The sled room doors were secured and locked. The main air tanks were pressurized, and the sled propulsion system was triggered from the VIA control room. Upon test completion, the emergency stop button was engaged, and the tanks were depressurized, rendering the sled system safe for post-test procedures.

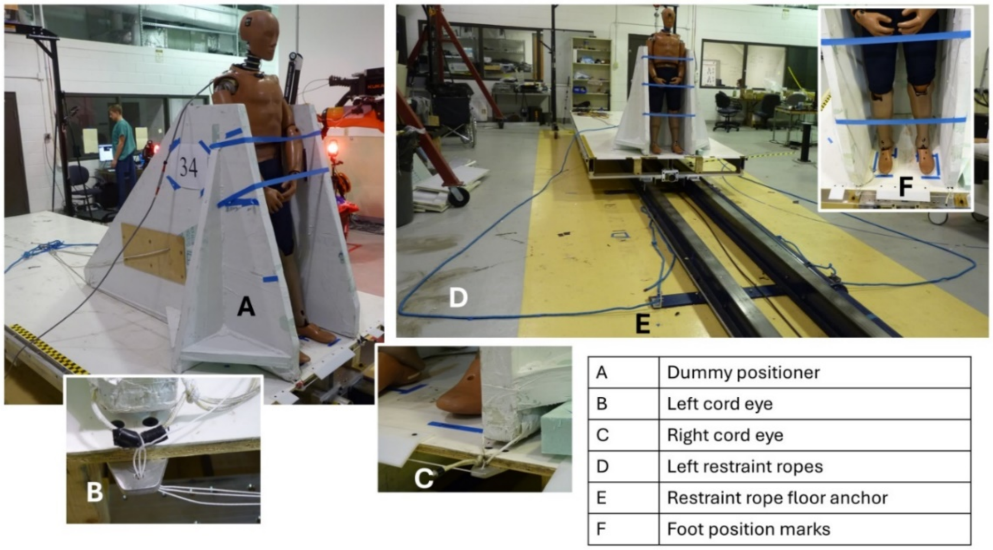

A	Dummy positioner
B	Left cord eye
C	Right cord eye
D	Left restraint ropes
E	Restraint rope floor anchor
F	Foot position marks

Figure 65. Dummy positioner.

Table 20 summarizes the sled test procedures developed to ensure safe, repeatable tests. Steps include dummy positioning, data acquisition, VICON and high-speed video camera data, and sled and scoop operation.

Table 20. Sled Test Procedures

Pre-Test Preparation
Dummy
Adjust knee and ankle joint stiffness to ~ 2g (twice normal for standing stability)
Inspect for damage, repair as needed
Don clothes for lying and sitting tests
Scoop, Sled Tracks
Lubricate pneumatic cylinders and sled tracks
Sled
Turn on magnetic velocity gate and inspect, adjust, and position trigger sensor
Ensure the chassis is at the start of the track and that the safety pin is engaged
Data Acquisition and Cameras
Verify that all channels are plugged in
Power on and calibrate VICON
Run preliminary diagnostics check
Run trigger check
Dummy Positioning
Place positioner on sled centered. full forward for front/rear tests, secure with cord
Arrange restraint ropes
Position dummy in positioner and attach trigger cable
Once dummy is positioned, install Vicon markers on dummy, positioner, sled, stage, scoop
Secure VIA Sled Room
All doors closed and secured, announce area closed for testing
Final Steps
Check and clear alarms.
Set sled launch pressure to achieve target sled speed
Ensure countermeasure is ready, (airbag blower on)
Prepare data acquisition systems (DAS) and cameras
Check position of dummy on the sled; disconnect DAS power cable
Inspect dummy trigger
Ensure the track area is clear of debris, tools, and equipment
Take pretest photos.
Confirm all personnel are ready for countdown
Ensure the sled room is clear. All personnel must be in control room
Pressurize pneumatic cylinder tank and announce that scoop is armed and to avoid area in front of scoop
Sled Launch
Pressurize sled propulsion tanks to target pressure
Launch sled once tank pressure is achieved
Post Launch
Vent pressurized tanks
Allow personnel in test area only when sled and scoop are in safe mode
Take post-test photos
Record test comments, observations, and failures
Camera and dummy DAS downloaded

Data Acquisition and Filtering

The Hybrid III is instrumented with IMUs and load cells in the head, thorax, and lower extremities as well as a rod pot to measure sternal chest deflection. The dummy's onboard data acquisition system (DAS) samples sensor data at 10 kHz. The raw data is filtered using SAE-recommended channel frequency class (CFC) (Table 21). The signal polarity of the dummy conforms to the coordinate system in accordance with the SAE J211/1 MAR95 instrumentation for impact tests (Figure 66) [30].

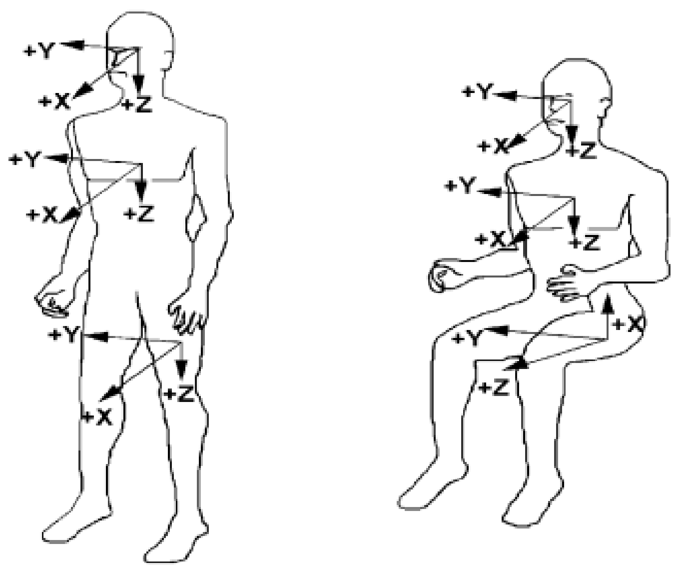

Figure 66. Hybrid III local coordinate frames.

Table 21. CFC Filtering Parameters and SAE Recommendations for Filtering [30], [31]

Filter Type	Filter Parameters	
CFC 60	3-dB limit frequency	100 Hz
	Stop damping	-30 dB
	Sampling frequency	at least 600 Hz
CFC 180	3-dB limit frequency	300 Hz
	Stop damping	-30 dB
	Sampling frequency	at least 1800 Hz
CFC 600	3-dB limit frequency	1,000 Hz
	Stop damping	-40 dB
	Sampling frequency	at least 6 kHz
CFC 1000	3-dB limit frequency	1,650 Hz
	Stop damping	-40 dB
	Sampling frequency	at least 10 kHz

Measurements	CFC
Head – Acceleration, Angular Velocity	1000, 60
Chest – Acceleration, Angular Velocity, Displacement	180, 60, 600
Neck – Forces, Moments	1000, 600
Pelvis – Acceleration, Angular Velocity	1000, 60
Femur – Forces, Moments	600
Tibia – Forces, Moments	600

Countermeasure Deformation

Figure 67 describes dummy penetration into the countermeasure. Figure 68, Figure 69, and Figure 70 illustrate post-test deformation for the crushable aluminum countermeasures. None of the tests resulted in the countermeasure bottoming out, and in all cases, there was less than 60% deformation observed in the countermeasure.

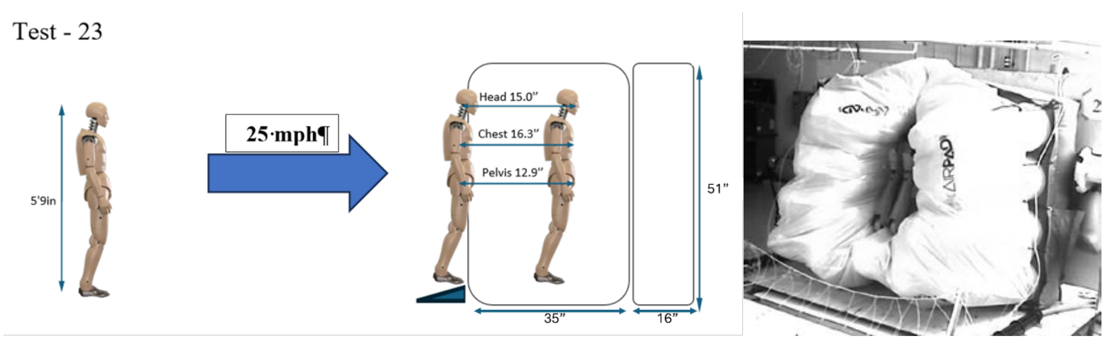

Test - 24

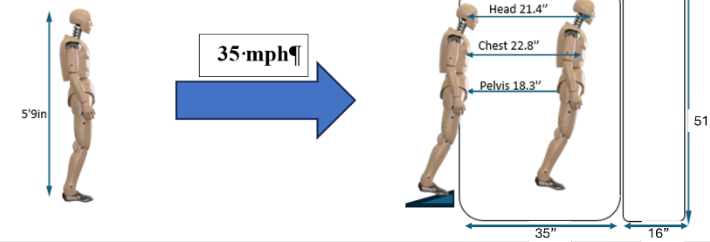

Test - 25

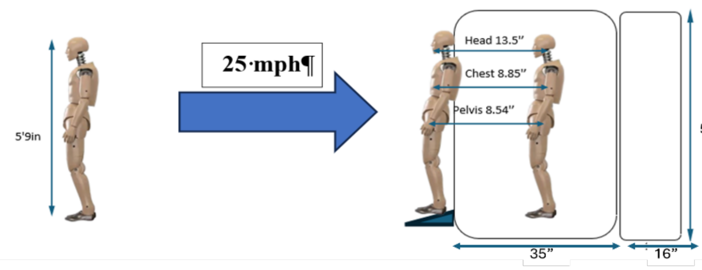

Test - 26

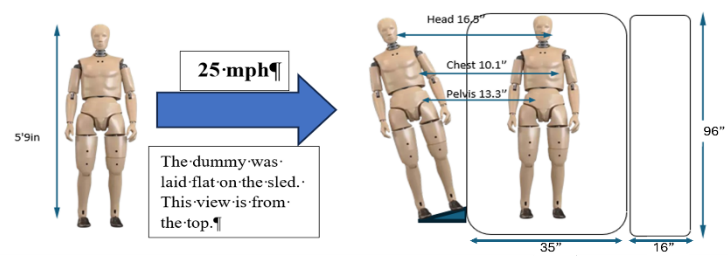

Test - 27

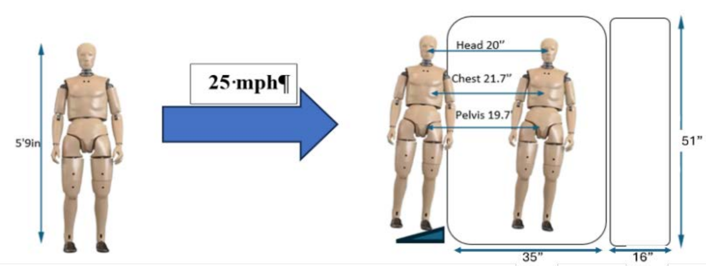

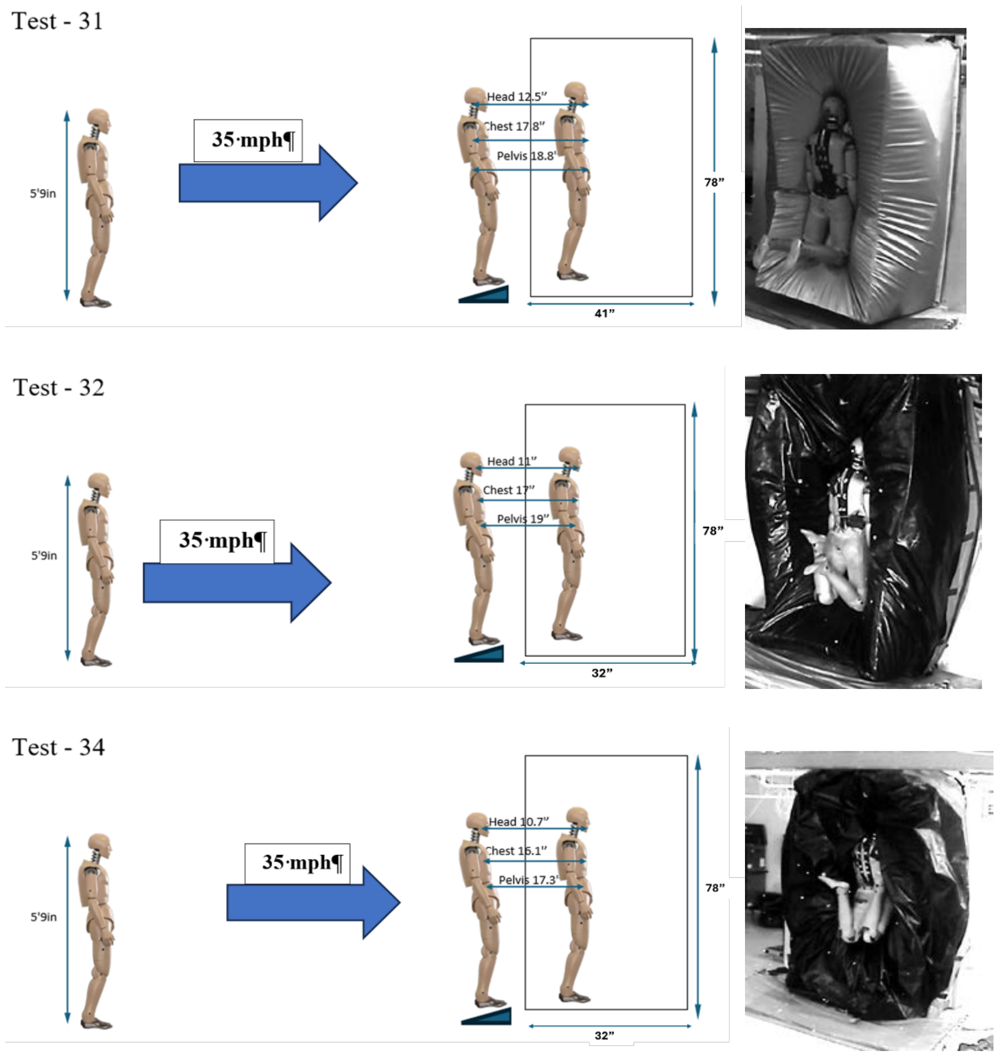

Figure 67. Dummy penetration into countermeasure as reported by VICON.

Test 31

Figure 68. Post-test countermeasure deformation Test 31.

Figure 69. Post-test countermeasure deformation Test 32.

Figure 70. Post-test countermeasure deformation Test 34.

Appendix B. Cost Benefit Supplementary

Following the USDOT benefit-cost guidance, a benefit-cost method was formulated to assess the financial viability of the project [28]. The methodology for determining a project's value to society involves estimating future costs and benefits in terms of present day, or base year dollars. For this analysis, 2022 is considered the base year. To understand the following discussion, it is important to provide some clarity on the terminology that will be used in this section (Table 22) as well as variables that will appear in the benefit-cost calculations (Table 23).

Table 22. Definitions for benefit-cost analysis.

Countermeasure	Countermeasure refers to the method or intervention used to prevent or mitigate injury and death.
Device	The term *device* indicates a single countermeasure implementation. Each instance is therefore a modification aimed at reducing the risk of injury or death to commuters and transit workers. The term includes all modifications to the transport system, and installations and modifications to the infrastructure.
Base year	Year for which costs and benefits are calculated. All future costs and benefits are adjusted to base year dollars according to the discount rate. In the context of this thesis the base years is 2022.
Lead Time	The number of years spent on planning and development before the buildout phase of the project begins.
Buildout	The buildout describes the time period over which the countermeasure will be implemented. It is assumed that the implementation will occur linearly (i.e., constant work-rate over time) after some initial lead time.
Baseline Injury Distribution	The baseline distribution refers to the current number of yearly cases within each injury severity category as defined by the injury scale of choice.
KABCO	KABCO is an injury severity scale made for use largely by police and first responders. It is based on the observed outcome at the scene of an incident, rather than injuries identified by a medical professional.
Net Present Value (NPV)	The NPV applies to a series of cash flows occurring at different times. The present value of a cash flow depends on the interval of time between now and the cash flow. It also depends on the discount rate. NPV accounts for the time value of money and provides a method for evaluating and comparing capital projects or financial products with cash flows spread over time, as in loans, investments [32].
Benefit-Cost Ratio (BCR)	The BCR is a ratio used in a benefit-cost analysis to summarize the overall relationship between the relative costs and benefits of a proposed project. BCR can be expressed in monetary or qualitative terms. If a project has a BCR greater than 1.0, the project is expected to deliver a positive net present value [32].

Table 23. Variable descriptions for benefit-cost analysis calculations.

N	The total number of yearly incidents.
N_i	Injury distribution: the number of yearly incidents that fall within an MAIS injury severity category *i*.
π_i	Normalized injury distribution: the proportion of yearly incidents that fall within an MAIS injury severity category *i*.
F	The proportion of yearly incidents that result in a fatality.
E	Countermeasure effectiveness at reducing fatality.
n	Number of devices.
r	Discount rate.
T	Buildout time.
$d(t)$	Discount factor.
$B(t)$	Yearly benefit.
$C(t)$	Yearly costs.

Installation and Maintenance Cost

Lower end estimates for installation costs were derived from material costs for the false floor and countermeasure. The estimated cost per device is based on the market price of possible materials that exhibit favorable properties, such as high hysteresis and stiffness, similar to the optimized material as determined by simulation. These include aluminum honeycomb and open-cell urethane foam, the associated cost is estimated to be no more than $100,000, which corresponds to a cost of $135 million USD to install these devices on all trains. Assuming these devices will need to be replaced after an incident, the estimated yearly maintenance costs are approximately $15,000 per device. To prevent rollover, this device must be paired with a scoop and false floor. The estimate for the cost of the false floor is derived from the price of rubber level crossing panels and the total length of track within the stations. This is expected to cost $100 million USD. Projects requiring more extensive station renovation may serve as an upper bound for the cost estimate. A 2020 study estimated that a platform door implementation would cost approximately 7 billion USD, and the associated yearly upkeep would be $119.2 million [2]. There is also an ongoing project to expand station accessibility that has been estimated to cost 5 billion [33].

Benefits

The benefits accounted for in this analysis are solely based on lives saved and injuries prevented and does not include benefits from reduced transit delays. Yearly benefit is based on VSL and the difference in projected injury distribution (Figure 9) and the baseline distribution (Figure 3). This calculation is discussed in the section on Yearly Benefit.

Buildout and Lead Time

For the purposes of this analysis, it was assumed there would be a five-year lead time for the planning phase of the project, and a 25-to-30-year buildout time. This estimate is based on other MTA station renovation projects [33].

Discount Rate

Guidance for selecting an appropriate value for the *real* discount rate r is outlined by the US Federal Highway Administration (FHWA). For transportation projects, the FHWA recommends selecting r that reflects the time value of money after adjustment for inflation [34]. The value of r can be tied to the interest rates on a 10-year Treasury bill; for example, assuming the interest on a

10-year Treasury bill is 6% and inflation is 3%, then *r* could be 3%. As of 2023, the US Office of Management and Budget (OMB) recommends using a 2% discount rate [35].

Project Sunset

The project sunset, or the total number of years for which to include when considering the accrual of costs and benefits, is an arbitrary choice of the user. This can have a substantial effect on both NPV and BCR if this value is set low. However, because both the costs and benefits converge to a finite number, even when the sunset date is set to infinity, the choice between two large values for the sunset has very little effect on NPV and BCR. For this analysis, the sunset date is 50 years.

Value of a Statistical Life (VSL)

The benefit of preventing a fatality is measured by what is called the Value of a Statistical Life (VSL), defined as the additional cost that individuals would be willing to bear for improvements in safety (that is, reductions in risks) that, in the aggregate, reduce the expected number of fatalities by one. Each Maximum Abbreviated Injury Scale (MAIS) severity level comes with an associated cost which is described as a percentage of VSL (Table 24). As of 2022, the US Department of Transportation considers the VSL to be $12.5 million dollars [29]. It also provides guidance on estimating the dollar value of various injuries in terms of fractional VSL [28].

Table 24. Value of Statistical Life (VSL) in millions of dollars per incident and the observed number of incidents within each MAIS severity category, 2019. VSL figures are based on 2021 US DOT guidance, increased by 3% to predict expected 2022 figures [28].

MAIS Injury Severity Level	Fraction of Fatal VSL	VSL in millions of 2022 US Dollars
0 No injury	0.000	$0.00
1 Minor	0.003	$0.04
2 Moderate	0.047	$0.57
3 Serious	0.105	$1.28
4 Severe	0.266	$3.23
5 Critical	0.593	$7.20
6 Fatal	1.000	$12.15

Injury Distribution

The injury distribution (N_i) is the *annual incident count* within a given MAIS category ($i = 0, \ldots, 6$). Incident outcomes are described according to the 6-level Maximum Abbreviated Injury Scale (MAIS) [7], with MAIS 1 corresponding to an injury with little to no chance of death, and MAIS 6 corresponding to an injury that is usually fatal. A normalized injury distribution (Eq. 26) describes the proportion of total cases that result in a given injury outcome with respect to the total number of yearly incidents (N).

$$\pi_i = \frac{N_i}{N} \qquad \text{Eq. 26}$$

The baseline injury distribution (N_i^B) refers to the spread of injuries observed prior to the implementation of a countermeasure. The projected injury distribution (N_i^P) refers to the predicted spread of injuries after a countermeasure has been fully implemented.

Yearly Benefit

The yearly benefit refers to the rate of benefit accrual at a given point in time. In addition to the benefit of saving a life associated with VSL, incidental economic benefit associated with avoiding an accident can also be considered. This would include incident-related delays and operational costs. To account for the buildout phase of the project, it is assumed that the benefit accrual will be proportional to the number of devices installed. Previous literature suggests that there have been a consistent number of yearly fatal incidents since the 1990s [3]. Assuming the total number and distribution of incidents remains constant, the *annual future benefit* is

$$B_{future}(t) = \sum_{i} \left(\Delta N_i (VSL_i + L_i) \right) * P_{built}(t) , \qquad i = 1, \dots, 6 \qquad \text{Eq. 27}$$

$P_{built}(t)$ is the percent buildout as a function of time measured in years from the base year. L_i represents incident related operational costs, and ΔN_i is the negative change in distribution due to the implementation of a countermeasure. This term can be calculated by subtracting the product of the *projected normalized distribution* and the *annual incident count* from the *baseline distribution*.

$$\Delta N_i = N_i - \pi_{P_i} N = N_i^B - N_i^P \qquad \text{Eq. 28}$$

Translating this to present benefit is done as outlined in the appendix.

$$B_{present}(t) = \frac{B_{future}(t)}{d(t)} \qquad \text{Eq. 29}$$

$$d(t) = (1 + r)^t \qquad \text{Eq. 30}$$

Yearly Costs

Yearly costs are the spending rate at a given point in time. As previously mentioned, these costs consist of a one-time installation cost and upkeep costs. During the buildout, one time installation spending can be calculated according to Eq. 31.

$$C_{install}(t) = \begin{cases} \frac{nC_{device}}{T} \; if \; t_{start} \leq t \leq t_{end} \\ 0 \; otherwise \end{cases} \qquad \text{Eq. 31}$$

where n is the total number of devices to be installed, and T is the time over which the buildout will occur and C_{device} is the cost per device. Maintenance costs can be modelled as Eq. 32.

$$C_{upkeep}(t) = nC_{maint}P_{built}(t) \qquad \text{Eq. 32}$$

where C_{maint} is the maintenance cost per device. Present cost (Eq. 33) can be found by summing these two terms and dividing by the discount factor.

$$C_{present}(t) = \frac{C_{upkeep} + C_{install}}{d(t)} \qquad \text{Eq. 33}$$

Benefit-Cost Ratio

The BCR for a given project describes the quotient of the total benefit and the total cost. This can be computed according to Eq. 34.

$$BCR = \frac{\int_0^\infty B_{present}(t)\,\partial t}{\int_0^\infty C_{present}(t)\,\partial t} \qquad \text{Eq. 34}$$

This can be interpreted as a measure of the project's efficiency, or the returns expected per dollar spent.

Net Present Value

NPV is the difference between the total benefit and the total costs.

$$NPV = \int_0^\infty B_{present}(t) - C_{present}(t)\,\partial t \qquad \text{Eq. 35}$$

Appendix C. Strain-Based Thoracic Injury Criteria Analysis

For the THUMS thoracic injury risk assessment, rib strain was used as a predictor of fracture. Forman et al. (2022) presented two methods for predicting cumulative rib fractures, and it was important to determine which approach was more appropriate for use in this thesis. Section 2.3.6 mentioned the choice of method without going into detail on the rationale behind the choice. Analysis on both approaches suggested that the separate IRF optimization had been overfit to the data it was developed on. The following section provides a brief overview of the methodology and outlines the problem with the separate optimization approach.

Method Overview

The thoracic injury criterion described in Forman et al. (2022) is a method of predicting risk of cumulative rib fractures from individual rib strains [17]. Separate IRFs were developed to predict 3+ and 7+ rib fractures. There was also a combined optimization for an IRF that can be used to predict both 3+ and 7+ fractures. Rib strain is mapped to fracture risk using these IRFs, from which the cumulative risk is computed. To illustrate how this method works, if an impact results in two ribs having a 100% fracture risk, and two ribs having a 50% risk, the cumulative risk of three or more fractures is 75% (Figure 71).

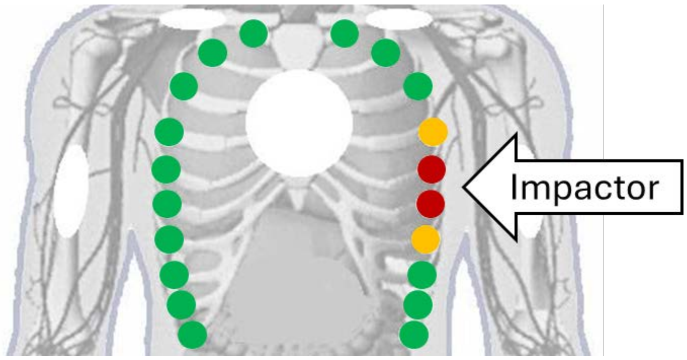

Figure 71. Example impact where two ribs have a 100% risk of fracture, and two ribs have a 50% risk of fracture. The cumulative risk of three or more fractures in this case would be 75%.

The IRF tuning was based on matched THUMS simulations that replicate the loading conditions of PMHS tests in the literature. These PMHS tests were a mix of impactor, tabletop, and occupant sled tests with restraint systems, and were primarily concentrated loading cases. The beta values shown in Table 9 were optimized to predict the correct number of rib fractures in the matched simulations. As mentioned in section 2.3.6, the 3+ and 7+ IRFs are different, and cannot be thought of as predictors of individual rib fractures. There are many explanations that could account for this discrepancy. For instance, the THUMS human body model may not distribute loads across the rib cage as much as a cadaver. A more concentrated loading pattern in THUMS would require a more sensitive IRF to predict seven rib fractures.

Analysis

While the separate formulation was more predictive in concentrated loading cases, there was an indication that it would not extrapolate well to other loading conditions. To illustrate this concern, it is useful to examine the case of perfect distributed loading where all ribs have equal strain. As shown in Figure 72, the strain-based method predicts a higher likelihood of 7+ rib fractures than

3+ rib fractures for most strain values. This result is non-physical and a good indicator that the separate risk curve formulation is not predictive in perfect distributed loading. However, this type of loading never happens in practice. Even in most distributed loading cases only a subset of the ribs experience a significant amount of strain.

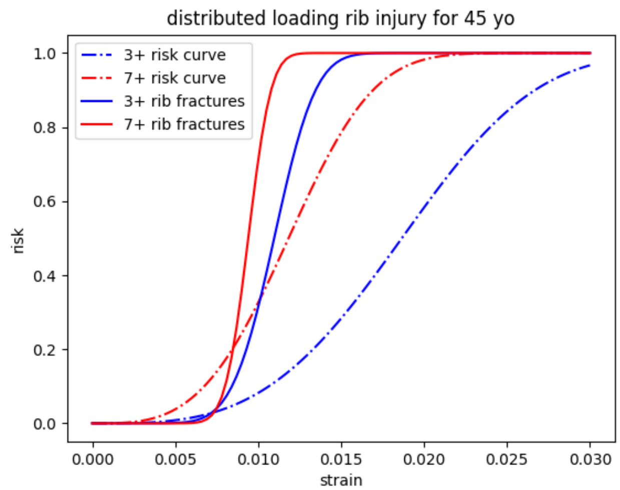

Figure 72. 3+ and 7+ IRFs along with cumulative risk of 3+ and 7+ fractures.

A Monte Carlo simulation was used to better understand how cumulative fracture risk changes between concentrated loading and distributed loading cases. Virtual pedestrians were created by generating random strain values between 0 and 0.02 for a subset of ribs. These strain values were mapped to individual fracture risk using each IRF (Figure 73) which yielded cumulative fracture risks.

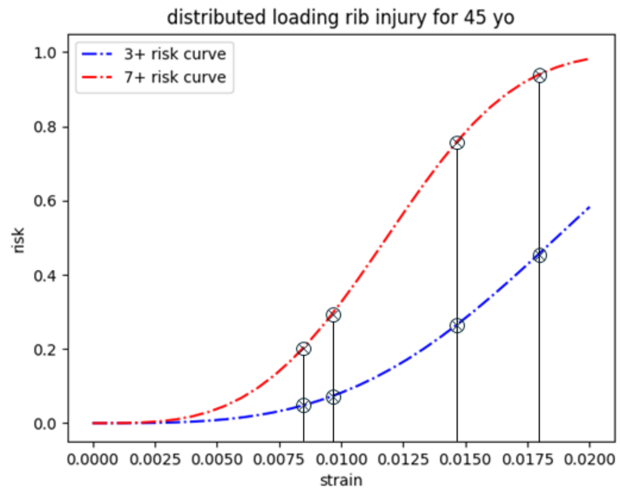

Figure 73. Sampling of rib strain for Monte Carlo analysis.

This exercise was repeated for 200 virtual pedestrians, varying the number of impacted ribs between 7 and 24. Cumulative risk of fracturing three or more ribs was plotted against seven or more. The dotted blue lines in Figure 74 represents equal risk of 3+ and 7+ fractures, thus any case that lies above this line would indicate a non-physical prediction by the IRFs. Even when less than half of rib cage is affected by an impact, the IRFs frequently predict a higher risk of 7+ fractures.

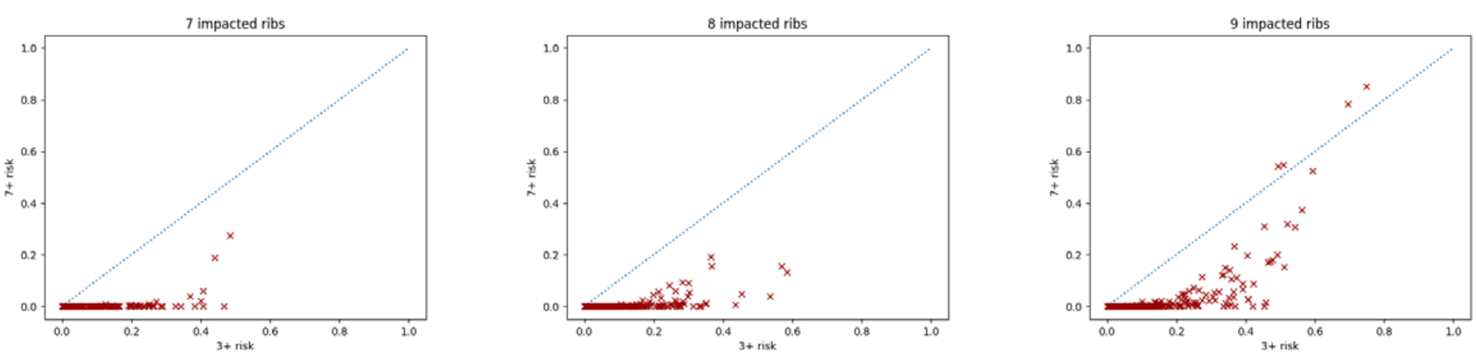

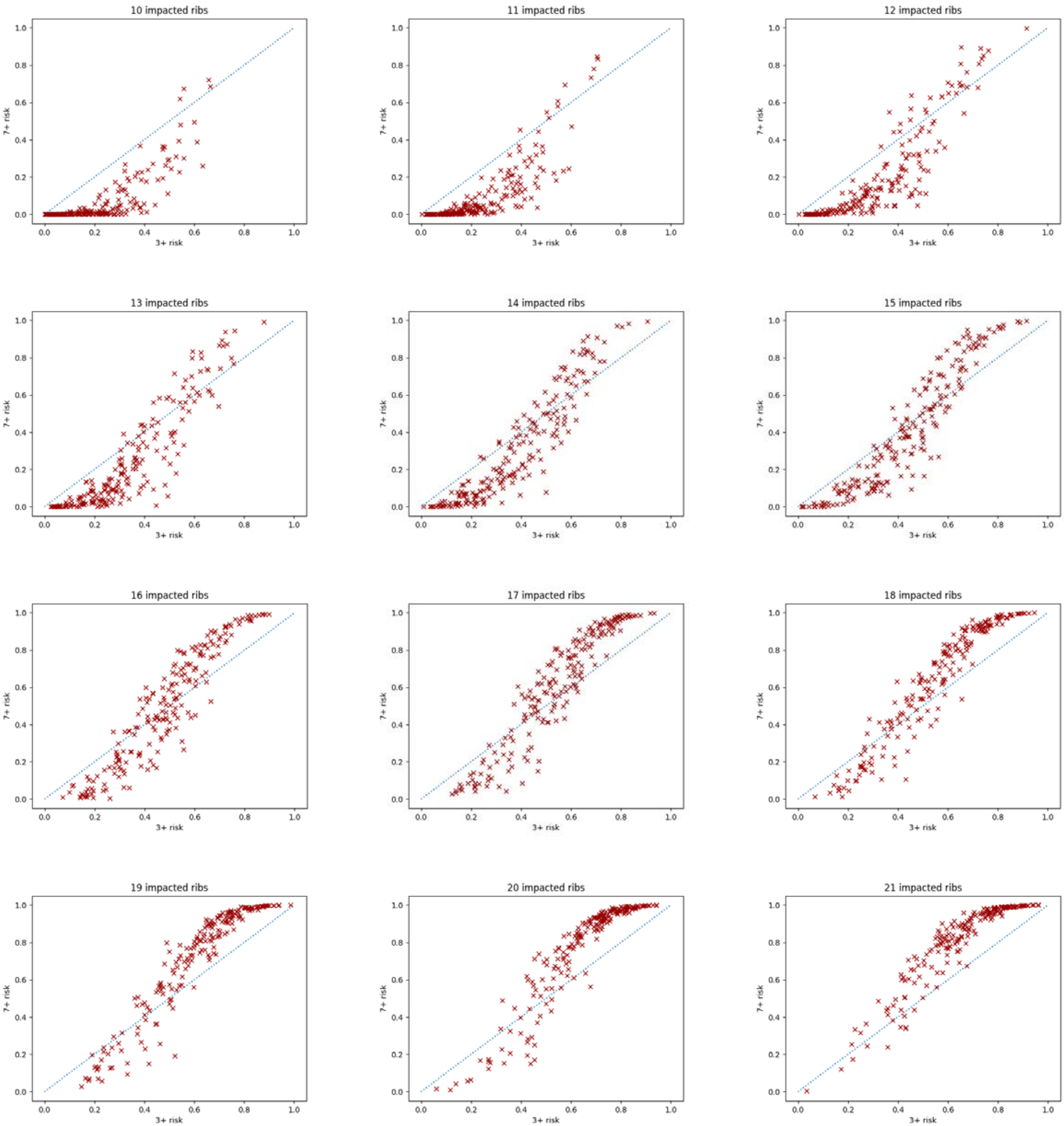
10 impacted ribs
11 impacted ribs
12 impacted ribs
13 impacted ribs
14 impacted ribs
15 impacted ribs
16 impacted ribs
17 impacted ribs
18 impacted ribs
19 impacted ribs
20 impacted ribs
21 impacted ribs
7+ risk
3+ risk

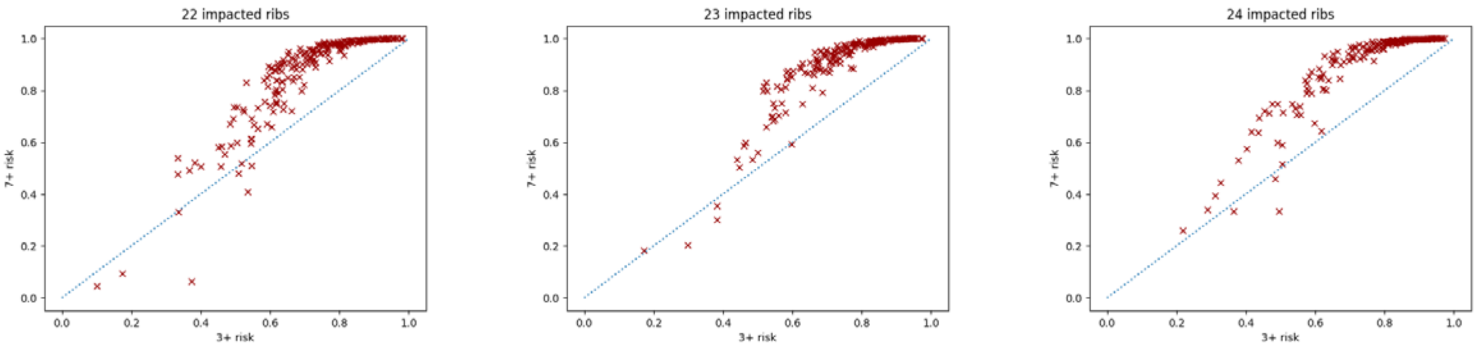

Figure 74. Monte Carlo analysis of 3+ and 7+ rib fracture risk with varying number of impacted ribs.

The Monte Carlo analysis indicated that the separate optimization overfit the risk curves, although it was unclear whether the loading conditions in the countermeasure simulations were similar enough to the matched cases for these IRFs to be predictive. To answer this question, THUMS frontal impact simulations were run using the cored honeycomb material model at speeds between 40 and 50 mph. A higher risk of fracturing seven ribs was predicted at all speeds (Figure 75), demonstrating that the separate curves could not be used to predict injury in these cases. Instead of using separate IRFs, the combined risk curve was used for the injury analysis in this thesis.

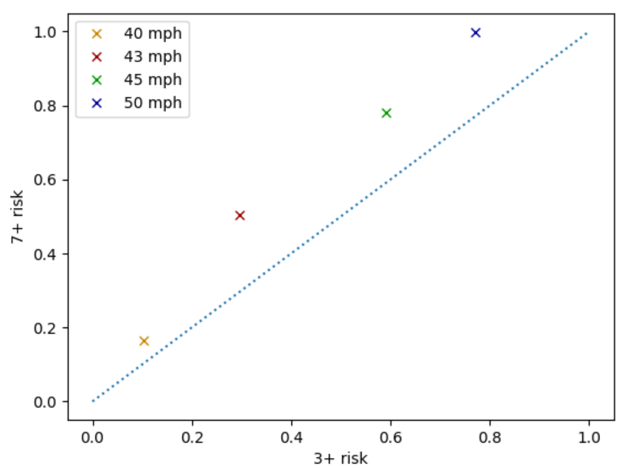

Figure 75. Distributed loading simulation results predict a higher risk of 7+ rib fractures than 3+ rib fractures when using separate IRFs.

Appendix D. Limitations

Human Body Model

The benefit cost model was constructed of elements that involved varying levels of uncertainty. In addition to those discussed above, the reliance on FEA to estimate countermeasure effectiveness required the use of a human body model. Human body models have typically been developed and validated for either occupant or pedestrian loading conditions. The pedestrian human body models are well suited for detecting injury in the primary impact. However, they are often not capable of making accurate predictions of post impact kinematics or evaluating injury in cases where the train wheels interact with the pedestrian. For these reasons, it was not possible to evaluate injuries caused by rollover or secondary impact with the track bed. It is therefore necessary to assume the countermeasure will be paired with a scoop and false floor that would limit secondary impact and will prevent rollover.

Injury Coding and Translation to MAIS

Section 1.2 describes how the KABCO coded injuries reported in the incident reports were translated to MAIS. There are several limitations of this method that are important to address. The existing KABCO-MAIS translation treats the KABCO 'Killed' category as an MAIS 6 injury, meaning that any subway incident that resulted in a fatality was translated to an MAIS 6 injury. KABCO is a scale based on the outcomes of an incident, while MAIS is a scale that represents the risk of death associated with an injury. An injury from any AIS category can cause death, so it is almost certainly the case that many of the deaths recorded in the incident reports were the result of an AIS 5 or lower injury. The result of this limitation is that the baseline injury distribution translated from the incident reports likely overestimates the number of AIS 6 injuries and underestimates the number of AIS 4 and AIS 5 injuries.

Injury Risk Curves

IRFs are used to assess injury risk in a simulation or physical test. An IRF describes the likelihood of sustaining an injury of at least the severity associated with the IRF. For instance, the risk of an AIS 3 chest injury is determined by the difference between the AIS 3+ and AIS 4+ curves as shown in Figure 76. Due to limitations of injury risk research, most body regions do not have AIS 5+ or AIS 6 IRFs. This means that it is impossible to differentiate between AIS 4, AIS 5, and AIS 6 injuries in these cases. Because of this limitation the best and worst cases were considered. One where all AIS 4+ injuries are treated as AIS 4 which constitutes the upper bound for countermeasure effectiveness, and where all AIS 4+ injuries were treated as AIS 6 which would correspond with the lower bound.

Figure 76. Lateral thoracic injury risk curves based on normalized chest deflection for a 45-year-old male. The risk of an AIS 3 injury is determined by the difference of the AIS 3+ and AIS 4+ risk.

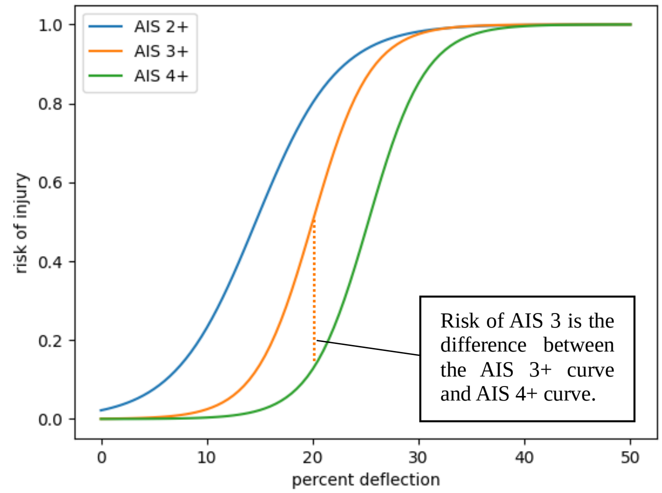

Subway Ridership

Based on previous NYC Subway research, it is reasonable to assume the total number of train-related incidents – fatal and non-fatal – remains stable over time [3]. If the number of incidents increases over time, future benefits will also rise, because the device will prevent a greater number of fatalities. If the number of incidents falls, perhaps as a result of an aggressive public safety campaign, future benefits will fall because the number of potential fatalities available to be prevented will also decrease.